ABSTRACT

Title of Document: SYSTEM ANALYSIS AND DESIGN FOR THE RESONANT INDUCTIVE NEAR-FIELD GENERATION SYSTEM (RINGS)

Dustin James Alinger, Master of Science, 2013

Directed By: Professor Raymond J. Sedwick
Department of Aerospace Engineering

The Resonant Inductive Near-field Generation System (RINGS) is a technology demonstrator experiment which will allow for the first ever testing of electromagnetic formation flight (EMFF) algorithms in a full six degree of freedom environment on board the International Space Station (ISS). RINGS is a hybrid design, which, in addition to providing EMFF capabilities, also allows for wireless power transfer (WPT) via resonant inductive coupling. This thesis presents an overview of the mechanical and electrical design of the RINGS experiment, as well as simulation techniques used to model various system parameters in both EMFF and WPT operational modes. Also presented is an analytical and experimental investigation of the influence of the proximity effect on a multi-layer flat spiral coil made from ribbon wire.

SYSTEM ANALYSIS AND DESIGN FOR THE RESONANT INDUCTIVE NEAR-FIELD GENERATION SYSTEM (RINGS)

By

Dustin James Alinger

Thesis submitted to the Faculty of the Graduate School of the

University of Maryland, College Park, in partial fulfillment

of the requirements for the degree of

Master of Science

2013

Advisory Committee:

Professor Raymond J. Sedwick, Chair

Professor David Akin

Professor Derek Paley

Acknowledgements

First, a huge thanks to my advisor, Dr. Ray Sedwick, for conceiving such an awesome experiment, for giving me the opportunity to work on such a great project, and for granting me the trust and independence to let me do things my way. His help and insight over the past few years have been invaluable, and there's no chance I would be where I am today had it not been for him.

I also owe a big thanks to Allison Porter, my grad student partner at UMD and the RINGS software mastermind, for her relentless dedication and contribution to every facet of the project. I doubt there's another pair of people on the planet who could make a coil stack as well as us - may we never have to wrap another layer again!

Thank you to everybody at Aurora Flight Sciences for their tireless efforts in getting the flight and engineering units built, and for always making me feel welcome at AFS. Thanks to John Merk and Charlie De Vivero for their contributions to the circuit designs, their excellent work in designing all of the RINGS PCBs, and their help and guidance with all of the electronics design. Thanks to soldering virtuoso Joanne Vining for the countless hours she put in to populate and coat the boards, and for teaching me a thing or two with the iron. And finally, thanks to Roedolph Opperman for his great work designing the RINGS to SPHERES support structure (which is definitely the best looking part of RINGS), for contributing his valuable creative insight to any mechanical design problem that came up, and for always lending a hand with anything RINGS needed.

Thanks are also owed to all those at the MIT SSL who helped make RINGS a reality. To Alex Buck and Greg Eslinger, thanks for all your exceptional work in getting RINGS and SPHERES to successfully (and peacefully) interface with one another, for all the great work testing them on the flat floor, for the huge number of hours I'm sure you put in to get us ready for the RGA flights, and of course for all the help in building the engineering and flight units. Thanks to Paul Bauer for all his help with the drive circuit, for recommending that we use the OSMC, and for teaching me the importance of reading the data sheet.

Also, thanks to Dr. Peter Fisher at MIT and Elisenda Bou at UPC Barcelona for all their help with the WPT side of RINGS.

Thanks to all of my labmates at the SPPL and all of my friends for putting up with the never-ending RINGS talk for the past two years.

Most importantly, thank you to my parents for their continuing love and support over the years.

Funding for this work was provided primarily by the DARPA InSPIRE program, through NASA contract number NNH11CC33C. Additional funding was also provided on the same contract by NASA Headquarters. The author gratefully acknowledges the support of both agencies.

To everyone on the RINGS team: congratulations, we made one hell of a payload…

"Is there life on Mars?" – David Bowie

Table of Contents

List of Tables

List of Figures

Chapter 1: Introduction

1.1: Electromagnetic Formation Flight

In the realm of satellite formation flying, a cluster formation refers to a group of satellites that share nearly identical orbital parameters and are separated by short distances, typically on the order of hundreds of meters. Sometimes called a cluster constellation, this arrangement can prove beneficial for several different technologies. Multiple-aperture interferometry (MAI) is one such technology. In MAI, a group of images, perhaps of the surface of Earth or another planetary body, are obtained from several telescopes in close proximity to one another. By cross-correlating these images, the resulting image resolution is comparable to that captured by a single, much larger aperture. Such a technique is highly advantageous for space-based imaging, since the cost of launching multiple smaller telescopes could be significantly smaller than the launch cost of a single larger telescope. An example of a proposed orbital MAI system is the U.S. Air Force Research Laboratory's TechSat-21 program, cancelled in 2003.

Another proposed technology that would utilize a clustered satellite arrangement is an architecture known as fractionated spacecraft. In this setup, the various subsystems typically found on a monolithic satellite are separated into separate modules. Brown and Eremenko propose in [1] that such a fractionated architecture would provide improved robustness and reduced development and operational costs versus traditional monolithic satellite designs.

Both of these technologies, and likely any technology based around clustered formation flight, require some means for controlling the individual attitudes and relative positions of the individual spacecraft. This control capability is most obviously necessary to maintain the desired orbit in the presence of disturbances such as differential drag and Earth oblateness, but could also be used to reposition the relative location of the individual satellites within the formation, perhaps to obtain some optimal spacing for MAI imaging. The traditional approach to providing such attitude and position control is through the use of propellant-based propulsion systems. However, this approach ultimately limits the operational lifetime of the cluster due to the finite amount of available propellant onboard a spacecraft. Electromagnetic formation flight (EMFF) is a propellant-less propulsion technology which aims to mitigate the operational lifetime constraints presented in a thruster based setup.

In an EMFF approach, each spacecraft in the cluster generates a magnetic field by circulating current through onboard wire coils. The interaction of these magnetic fields produces electromagnetic forces and torques that can be used to maneuver the individual satellites within the cluster. Due to conservation of momentum, the location of the center of mass of the cluster cannot change, but the spacecraft can be reoriented relative to one another. The energy required to drive current through the coils can be supplied by solar panels, eliminating the problem of limited consumables.

A full-fledged EMFF setup would include three orthogonally aligned coils on each spacecraft, to allow for the creation of a steerable magnetic dipole in all three

dimensions. Due to angular momentum conservation, an electromagnetic torque is produced in addition to the electromagnetic force, and as a result EMFF alone cannot provide attitude control. Instead, attitude control must be supplied through other means such as reaction wheels or control momentum gyroscopes.

In 2005, a two-dimensional ground-based EMFF testbed was created at the Massachusetts Institute of Technology (MIT) Space Systems Laboratory (SSL) [2]. It featured two vehicles, designed to operate on a flat floor using air carriages. Each vehicle contained two orthogonally aligned coils made from high-temperature superconducting (HTS) wire, as well as one reaction wheel. Due to the high currents needed to generate appreciable forces and torques over typical formation flight distances, HTS wire is an enabling technology for longer range EMFF. The power dissipation in traditional conductors at these high currents is prohibitively large, but this problem is eliminated in an HTS coil design. However, an HTS system is inherently more complex due to the thermal control system required to keep the wire at its superconducting temperature.

A non-superconducting EMFF testbed was also developed at the MIT SSL which used coils made from aluminum wire [3]. This one-dimensional proof-of-concept system, called micro-EMFF (μEMFF), was used to verify simulation models and to investigate various EMFF control algorithms. Most importantly, the μEMFF testbed successfully demonstrated that close proximity EMFF operations are feasible using coils made from conventional conductors.

1.2: Resonant Inductive Wireless Power Transfer

Wireless power transfer (WPT) using resonant inductive coupling is a means of non-radiative energy transfer. This technology exploits the fact that two resonators that are tuned to the same natural frequency will couple strongly to one another, but weakly into other objects that do not have the same resonant frequency, minimizing losses into the environment. In a magnetic induction setup, the resonators are made from coils of wire through which alternating current (AC) is driven. Circulating AC current through a source coil (also called a primary coil) generates an oscillating magnetic field which induces an electromotive force (EMF) in a receiver coil (also called a secondary coil). This EMF causes current to flow in the secondary coil, allowing for the wireless transfer of energy. A common example of a device that transfers power via inductive coupling is an electric toothbrush charger; however, the performance of such a system degrades rapidly as the distance between the source and receiver is increased, due to the small size of the coils used and the fact that the two coils are not operated at resonance. In a resonant system, the inductive reactance of the coils is cancelled by the capacitive reactance (either from the self-capacitance of the coil in a self-resonant system, or from that of an associated loading capacitor), which dramatically reduces the coil impedance at the resonant frequency. Since the power transfer efficiency is proportional to the frequency of operation, a system with a high resonant frequency is desirable. However, a tradeoff exists due to the fact that the coil resistance increases with frequency due to the skin effect, radiative losses etc.

Nikola Tesla first demonstrated WPT via resonant inductive coupling in the early 1900's [4]. However, very little further research was conducted on the topic for

over 100 years, most likely due to the lack of a pressing need for the wireless transfer of power at high efficiencies over moderate distances. With the advent of portable electronics, the technology has in the last ten years become one of great interest. In 2007, researchers at MIT demonstrated, via resonantly tuned coils, the wireless transfer of 60 watts at 40% efficiency over a distance of 2 meters [5]. This system used helical coils made from copper wire with a self-resonant frequency of approximately 10 MHz. A paper by the same team of researchers presented a framework for analyzing the resonant coupling system performance using coupled-mode theory [6]. Their results highlight the advantage of a resonant inductive system, as the analysis indicates that the resonant scheme can transfer 10^6 times more power than a typical non-resonant setup.

1.3: Resonant Inductive Near-field Generation System (RINGS)

Due to the physical similarities of the coils required for both EMFF and inductively coupled WPT, a hybrid system is an appealing option. The design of one such hybrid system, called the Resonant Inductive Near-field Generation System (RINGS), is the primary focus of this thesis.

RINGS is a technology demonstrator experiment consisting of two vehicles that will launch to the International Space Station (ISS) in the summer of 2013. Its goals are to demonstrate the feasibility of, and provide a testbed for, EMFF operations in a full 6 degree of freedom (DOF) environment. Additionally, RINGS will demonstrate resonant inductive WPT on the order of tens of watts over distances of approximately 1 meter.

Launched to the ISS in 2006, the Synchronized Position Hold, Engage, Reorient Experimental Satellites (SPHERES) experiment serves as a testbed for formation flight. The SPHERES satellites, shown in Figure 1, feature a metrology system that uses ultrasound and infrared sensors to determine both the position and attitude of the satellites within their operational volume on the ISS. Additionally, each SPHERE contains 12 CO_2 thrusters that allow them to maneuver within the test environment. This overall setup allows for the testing of various formation flight control algorithms in the full 6 DOF micro-gravity environment provided by the ISS. The SPHERES expansion port allows subsequently launched ISS payloads to interface with the satellites for various science purposes.

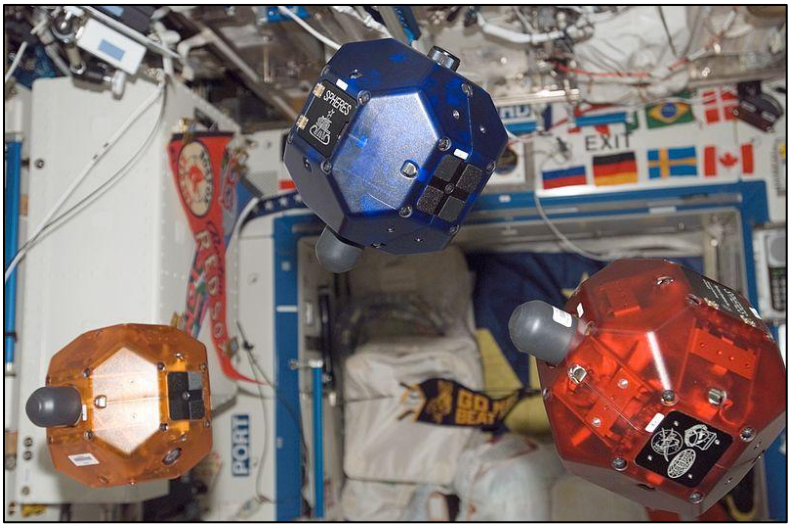

Figure 1 – SPHERES Satellites on the ISS

The RINGS vehicles are designed to attach to the SPHERES satellites and integrate with them through the expansion port. RINGS will utilize the SPHERES metrology system, allowing for the testing of various EMFF control algorithms. By firing their CO_2 thrusters in orthogonal pairs, the SPHERES satellites will provide the

torque control necessary for EMFF maneuvers. An early conceptual design for RINGS is shown in Figure 2.

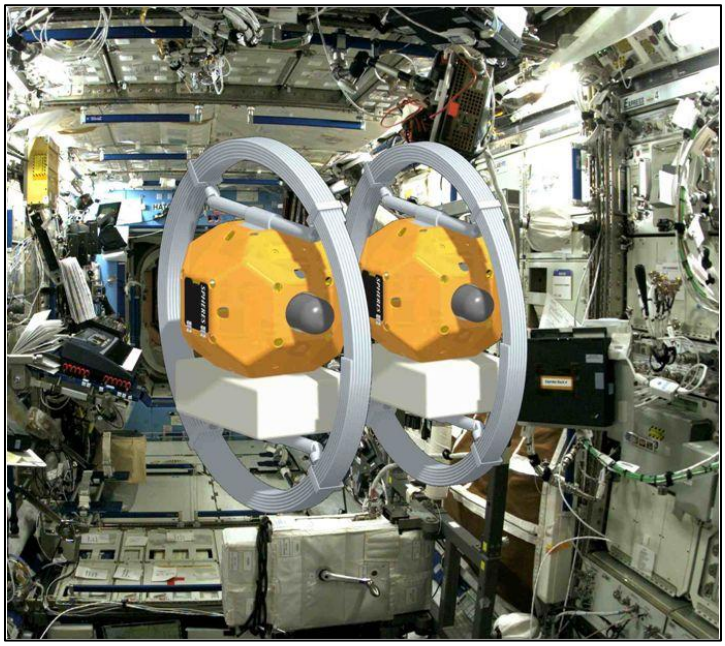

Figure 2 – Early RINGS Conceptual Design

The most important component of the RINGS vehicles is the wire coil, called the "resonant coil," which is used to generate the oscillating magnetic field used for EMFF operations and for WPT. While previous EMFF testbeds circulated direct current (DC) through the coil, RINGS is designed for AC EMFF operations. The main reason for this design decision is that a DC system is subject to parasitic torques caused by the coil's interaction with the Earth's magnetic field. An AC architecture, however, does not experience these parasitic torques. Additionally, since the coil currents must be AC for inductive WPT to occur, the overall coil drive circuit setup is simplified if EMFF is also operated at AC.

1.4: Statement of Contributions

The design, development, and construction of the RINGS experiment has been a largely collaborative effort. Significant contributions were made by other researchers from the University of Maryland Space Power and Propulsion Laboratory, our colleagues at Aurora Flight Sciences, as well as students and professors at the Massachusetts Institute of Technology Space Systems Laboratory. This thesis, however, aims to highlight the work to which the author made a distinct contribution.

The salient contributions of this work to the state of the art are as follows:

1. Design and construction of the first alternating current implementation of an EMFF system. Because the torque generated between two magnetic dipoles is proportional to the product of those dipoles, a direct current system, such as those presented in [2] and [3], interacts with the Earth's magnetic field, producing a net parasitic torque. If one of the dipoles is oscillating, however, the product of that dipole with the Earth's static dipole has an average value of zero, and no torque is generated.

2. Implementation of the first system which is capable of both electromagnetic formation flight and wireless power transfer, and the lessons learned regarding tradeoffs in coil design to optimize performance for both technologies. The ability to transfer power between vehicles could be a benefit to a satellite cluster that utilizes electromagnetic

formation flight technologies, so a hybrid EMFF/WPT design is an attractive option.

3. Development of practical construction techniques for manufacturing a multi-layer, low-dielectric flat spiral coil made from uninsulated ribbon wire. The space between the windings of an inductive coil is typically occupied by wire insulation. By removing this insulation, cooling air can penetrate the innermost windings of the coil, enhancing thermal performance and allowing for higher levels of power dissipation. Additionally, the low-dielectric loss design could be applied to self-resonant coils to improve their performance, since an uninsulated coil is not subject to dielectric losses in the insulation.

4. Experimental investigation of frequency variation of coil impedance up to 8 kHz, showing that the Dowell method [7] is largely inaccurate for such a compact coil design. Coil resistance and inductance change with frequency, which is a critical factor in determining the optimum power coupling frequency for a resonant inductive WPT system. Due to the large discrepancy between the analytical predictions of the Dowell method and the experimental results obtained, attempting to optimize a coil design using the Dowell method alone may prove unsuccessful.

5. Development of an analytical model of power coupling losses for a resonant inductive WPT system and application of this model to optimize performance for the presented coil design. The model examines the system in the frequency domain using a traditional block diagram composed of transfer functions, which is simpler to manage and more intuitively clear than a system of differential equations. This has value as a design tool, as it allows for the predicting of performance for different system parameter values, such as load resistance, operational frequency, etc.

6. Development of an analytical method for predicting the effective overall impedance of a coil whose impedance varies with frequency for the case of non-sinusoidal applied voltage waveforms. The examples presented in this thesis explore the case of an applied AC rectangular wave, but this method could be applied to any non-sinusoidal input, such as sawtooth or triangle waveforms, for any coil whose inductance and resistance are frequency dependent.

Chapter 2: Resonant Coil

2.1: Design

Early in the design process for the resonant coil, the decision was made to construct the coil from uninsulated wire having a rectangular cross section, also known as "ribbon" wire. The primary reason for this is the thermal advantage that it presents over a coil made from insulated wire. Power dissipation due to ohmic losses in the wire will cause the wire temperature to increase. The micro-EMFF testbed presented in [3], which utilized insulated wire coils, was ultimately limited by this power dissipation. To prevent the micro-EMFF coils from overheating required using pulsed currents of short duration or low amperage. RINGS was designed to operate continuously over a period of minutes or hours, and had the added constraint of operating in a microgravity environment where free convection does not exist. To maintain a healthy operating temperature, cooling fans had to be included to circulate air over and through the resonant coil. By eliminating the insulation, airflow from the fans is able to penetrate the inner windings of the coil, resulting in significantly improved cooling performance. A second reason for using ribbon wire is that its rectangular geometry is inherently easier to affix parts to than is wire with a round geometry. This allowed us to construct a coil with a secure, rigid geometry that could be firmly mounted within the coil housing.

The three basic design parameters for the resonant coil are the electromagnetic force generated between the two coils, the power dissipated in the coil due to ohmic losses, and the combined mass of the coil and SPHERES satellite. Using the far-field

approximation presented in [3], the force between two axially aligned coils can be approximated by

$$F = \frac{3\pi\mu_0}{2} I^2 N^2 \frac{r^4}{D^4} \tag{1}$$

where μ_0 is the permeability of free space ($4\pi \times 10^{-7}$ N·A^{-2}), I is the current in the wire in amps, N is the number of turns of wire, r is the coil radius in meters, and D is the axial separation distance of the two coils in meters. The power dissipated in the coil due to ohmic losses is approximated by

$$P = I^2 R \approx I^2 \bar{\rho}_R \frac{rN}{16\bar{w}\bar{h}} \tag{2}$$

where R is the resistance of the coil in ohms, $\bar{\rho}_R$ is the resistivity of the wire material in μohm·cm, $\bar{w}$ is the wire width in millimeters, and $\bar{h}$ is the wire height in millimeters. The combined mass of the SPHERES satellite and the coil is approximated by

$$M \approx M_S + \frac{rN\bar{w}\bar{h}\bar{\rho}_m}{160} \tag{3}$$

where M_S is the mass of the SPHERES satellite in kilograms and $\bar{\rho}_m$ is the mass density of the wire material in g·cm^{-3}. Equations (1), (2) and (3) can then be combined into a single cost function given by

$$C = \frac{MP}{F} = 66\bar{\rho}_m\bar{\rho}_R \frac{D^4}{r^2}\left[1 + \frac{160M_S}{\bar{\rho}_m rN\bar{w}\bar{h}}\right] \tag{4}$$

Based on operational volume constraints within the ISS, the mean radius of the coil was chosen to be approximately 30 centimeters. This coil size also comfortably encircled the SPHERES satellite while still providing ample room for the

RINGS to SPHERES support structure and the RINGS electronics. Both copper and aluminum were considered for the wire material, but we see in (4) that the product of mass density and resistivity needs to be minimized to increase system performance. This product is 50% lower for aluminum than it is for copper, despite the lower resistivity of copper. For this reason, as well as due to its wide commercial availability, aluminum was selected as the wire material.

The cost function given in (4) is composed of two terms. With the coil radius and separation distance fixed, the first term is ultimately governed by the material properties of the wire, namely its resistivity and mass density. The second term is governed by the coil geometry, represented by the product $N\bar{w}\bar{h}$. It was decided to weight these two terms equally, which required that $N\bar{w}\bar{h} \approx 800\ mm^2$. Prior experience in the University of Maryland Space Power and Propulsion Laboratory (SPPL) with manufacturing similar coils from superconducting tapes led to the selection of a wire aspect ratio, $\bar{w}/\bar{h}$, of roughly 6 to 1. Choosing $\bar{h}$ = 1 mm and $\bar{w}$ = 6 mm resulted in a number of turns, N, of 140, and a total coil mass of 4.25 kg. To achieve a mostly square overall cross section for the coil, it was decided to split these 140 turns into 7 layers of 20 turns per layer, with each of the 7 layers connected electrically in series. The prescribed height and width dimensions also provided a wire cross section with a good size and profile for attaching "combs", which are components used to prevent wire windings from contacting one another and are discussed in more detail later in this section. The distance between adjacent turns was chosen to be 1 mm, which was a compromise between manufacturability and the desire for a compact coil cross section. Additionally, the decision for the distance

between windings to be equal to the thickness of the wire itself dramatically simplified the manufacturing process, which is explained further in Section 2.2.

The maximum design current in the coil was calculated from the force required to execute a baseline circular maneuver. The parameters of this maneuver are that the RINGS complete a circular rotation about their common center of mass in a period of 1 minute with an axial separation distance of 1.5 meters. These times and forces are similar to those of commonly executed SPHERES maneuvers. The required centripetal force on a vehicle is given by

$$F_c = 4\pi^2 \frac{mD}{T^2} \tag{5}$$

where m is the total mass of the RINGS vehicle (including the SPHERES satellite), D is the axial separation distance, and T is the period of rotation. By setting equations (1) and (5) equal, we calculate the required number of amp-turns as

$$NI = \sqrt{\frac{4}{3}\frac{mD^5}{\mu_0 T^2 r^4}} \tag{6}$$

In addition to the coil itself, the final RINGS assembly would also have to contain other elements such as a support structure for attaching to SPHERES, a housing to encompass the coil, and other heavy items. As such, the mass of the entire operational vehicle was estimated to be three times the mass of the coil itself, plus the additional 4 kg of the SPHERES satellite.

The resulting root mean square (RMS) current required was calculated to be 2100 amp-turns RMS, or 15 amps RMS circulating through the 140 turn coil. The

resulting coil resistance was approximately 1.4 Ω and the dissipated power at 15 amps RMS was about 315 watts.

After becoming aware of the significant amount of time and effort required to manufacture a single layer of the coil, the decision was made to reduce the number of layers to 5 instead of 7, resulting in a 100 turn coil. As an added benefit, the 100 turn coil had a squarer cross section than the 140 turn coil, which was more desirable from a packaging standpoint and also reduced its resistance to approximately 1 Ω. At this point, the thermal design was already finalized to our original design point of 315 watts of power dissipated in the coil. To utilize the same power dissipation level, the maximum coil current was increased from 15 to 18 amps RMS. As a result, the total number of amp-turns at maximum current was decreased slightly from 2100 amp-turns to 1800 amp-turns. However, due to the $1/D^4$ force scaling, reducing the separation distance of the baseline maneuver by 7% (or only by 9 cm) compensated for the decrease in force while still achieving the rotational period of 1 minute.

The final design of the coil cross section is shown in Figure 3, with the key dimensions being summarized in Table 1. The notation used for the coil dimensions in Figure 3 and Table 1 have been modified so as to agree with the notation commonly used in the Dowell method for evaluating the change in coil impedance with frequency, the details of which are discussed in Section 2.3. The final alloy selected for the wire material was 6061 aluminum. This choice was made due to the desirable heat treatment properties of 6061, as well as the availability of this alloy in the cross-sectional dimensions (0.040" x 0.250") that were needed.

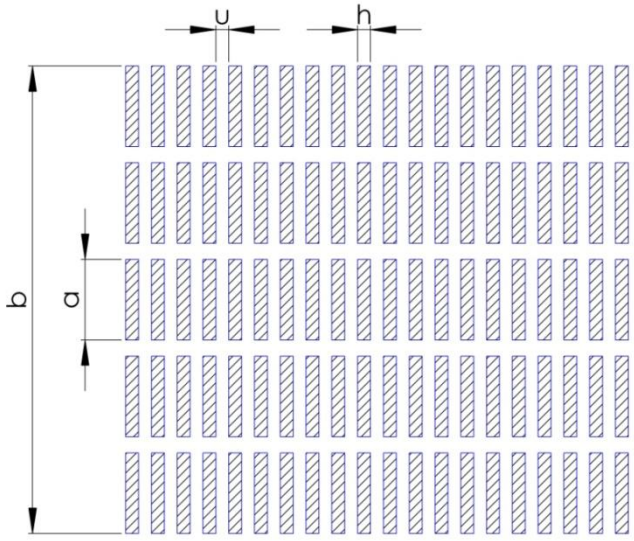

Figure 3 – Cross-Sectional View of Resonant Coil

Table 1 – Major Dimensions of Resonant Coil

Dimension	Description	Value
a	Breadth of a conductor	6.350 mm
b	Winding breadth	36.830 mm
h	Height of a conductor	1.016 mm
u	Height of an interlayer gap	1.016 mm
N_l	Number of turns per layer	5
η	$\frac{N_l a}{b}$	0.862
l_T	Mean turn length	200.289 mm
m	Number of layers	20
ρ	Resistivity	3.700E-8 Ω-m

To prevent neighboring windings from contacting one another and to help to maintain a rigid coil geometry, a polycarbonate part known as a “comb” was designed, as shown in Figure 4. Each comb has 20 grooves into which the windings of each layer are glued. Eight of these combs are placed on each layer of the coil with equal spacing in the circumferential direction. To minimize their impedance to the cooling airflow, the part was designed to have a very small volume in comparison with the total inter-winding and inter-layer volume within the coil. There are two types of combs used: double-sided combs, which have grooves on both sides, and single-sided combs, which have the same outer dimensions as the double-sided combs but only have grooves cut into one side. Single-sided combs are placed on the outer surfaces of the top and bottom layers, and double-sided combs are used between layers. The double-sided combs also serve to prevent inter-layer wire contact by providing an air gap of 0.050” between layers. The single-sided combs provide a means to secure the resonant coil within the housing, as will be discussed later.

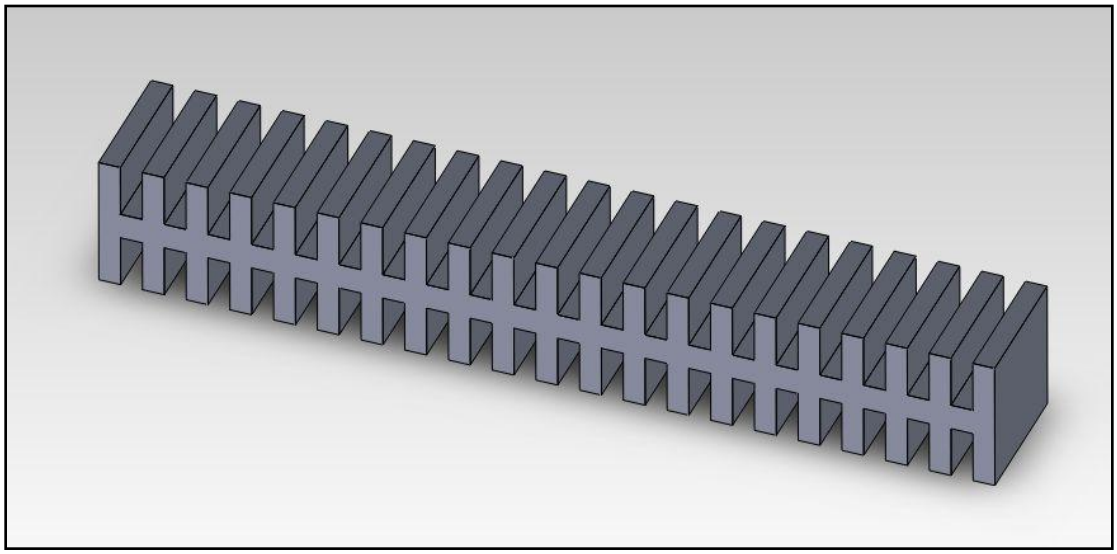

Figure 4 - Double Sided Comb

A total of 48 combs are installed in the resonant coil – 32 double-sided combs and 16 single-sided combs. Figure 5 shows an exploded view of the resonant coil and comb setup, with the coil layers shown in blue and the combs shown in red for clarity. Figure 6 shows a collapsed view of the same components, with the camera zoomed in on one of the eight comb locations.

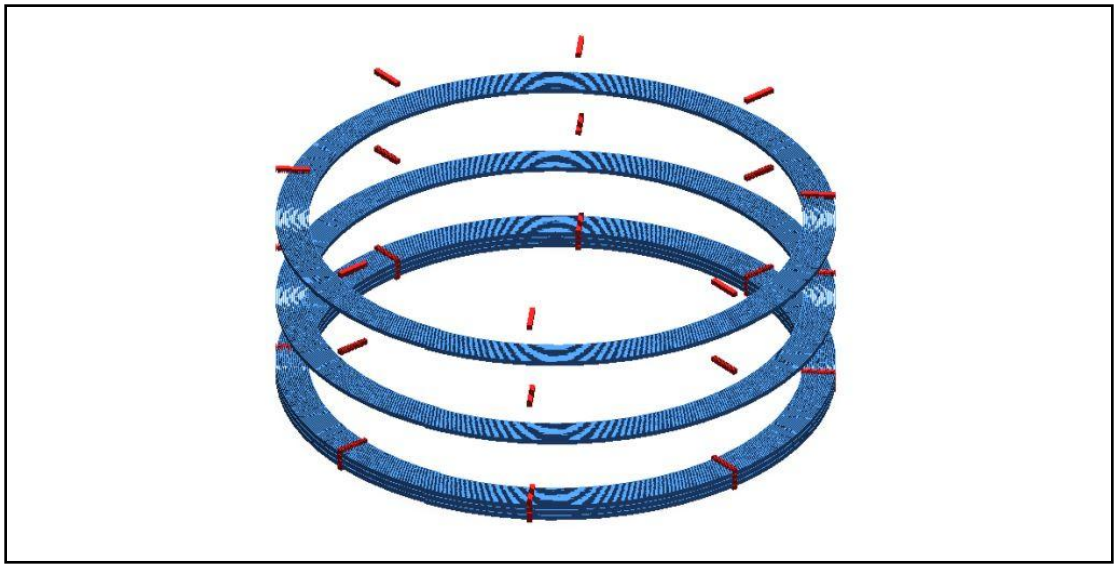

Figure 5 – Exploded View of Resonant Coil and Combs

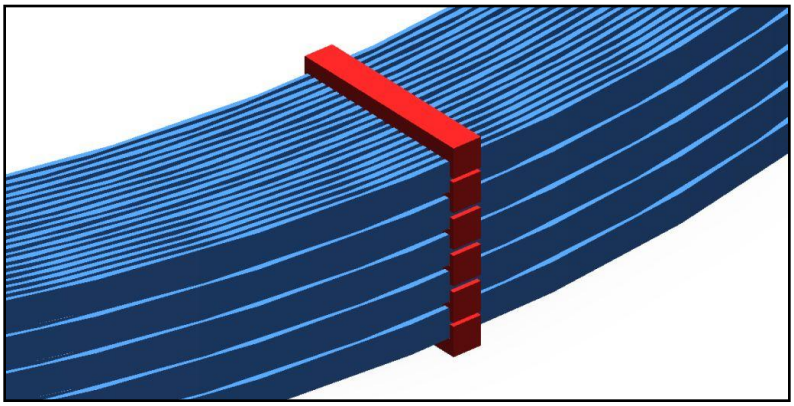

Figure 6 – One of the Eight Comb Locations on the Resonant Coil

It should be noted that the cross-sectional view shown in Figure 3 is an approximation, since successive layers of the coil spiral in opposite directions. More

specifically, layers 1, 3 and 5 are right-handed spirals and layers 2 and 4 are left-handed spirals. Since the end of one layer is connected to the beginning of the next layer, the alternating spiral design allowed for the layer-to-layer electrical connections to be made in a compact manner. Had all five layers spiraled in the same direction, the innermost winding of one layer would have to connect to the outermost winding of the next layer. This would require a jumper wire to be routed either above or below the entire stack, which was undesirable from a packaging standpoint. The inter-layer electrical connections are discussed further in Section 2.2.

2.2: Construction

The resonant coil was manufactured one layer at a time using a specially made, two-piece spool, which is shown in Figure 7. The inner piece of the spool has a spiral cut of the proper dimensions along its outer circumference, as well as a notch cutting in towards the center of the part, which provided a location to firmly anchor the wire at the beginning of the wrapping process. The backing plate of the spool is larger in diameter than the inner piece and provides support to the wire as it is wrapped around the inner piece. Both parts of the spool are made from 6061 aluminum and have 8 notches located around their circumference to allow for the installation of the combs.

Figure 7 – Spool Used to Manufacturer Coil Layers

The coil wire arrived wrapped on a factory spool, as shown in Figure 8, which had a much smaller diameter than was required for the coil layers. At the start of the wrapping process, a small 90 degree bend was made in the end of the wire and this bend was inserted into the notch on the two-piece spool. Then, the wire was carefully unwound from the factory spool and wrapped onto the two-piece spool.

Figure 8 – Coil Wire on the Factory Spool

As the wire was wrapped, "spacers" were regularly inserted around the circumference of the spiral so as to properly space out the windings of the layer.

These spacers were cut from the wire itself, since the desired gap between windings (0.040”) was the same thickness as the wire. Two types of spacers were used, called long spacers and short spacers. Long spacers were of an appropriate length to nearly span the distance between adjacent spool notches. Short spacers were slightly longer than the width of the notch. A section of one fully wrapped layer is shown in Figure 9. Throughout the wrapping process, the coil wire was periodically pulled on with a pair of pliers in order to ensure a tightly packed, snug wrap with no visible gaps between the coil wire and the spacers.

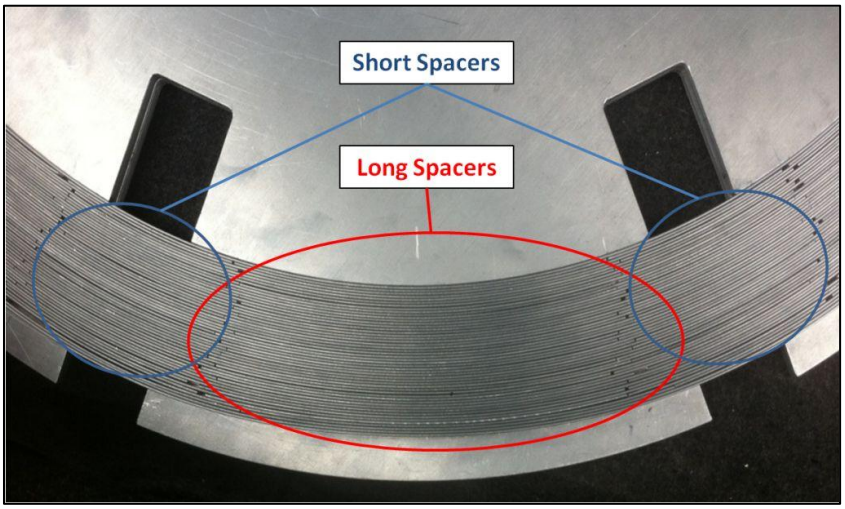

Figure 9 – Fully Wrapped Layer with Long Spacers and Short Spacers

While only 20 windings per layer were required for the design, each layer was wrapped with at least 23 windings. Later in the construction process, these excess windings were trimmed away to leave a coil with the desired number of 20 windings. The reason for wrapping a few additional windings was that after the wire was released from the pliers, the first one or two of the outermost windings tended to loosen slightly. For the windings away from the outermost windings, however, friction between the coil wire and spacers prevented them from loosening. After at

least 23 windings had been wrapped, a “holding band” was placed around the wrapping to secure the assembly. The holding band, which was also made from the coil wire material, was a hoop of appropriate size to snugly fit around the completed layer. A 90 degree bend was placed in the two ends of the holding band and these two bends were held together in a C-clamp.

The next step in the construction of a coil layer was a heat treatment process. Because of the smaller radius of the factory spool as compared to the custom two-piece spool, the wrapping process results in there being stored stresses in the wire. At this point, had the spacers been removed, these stored stresses would cause the windings to deflect back towards their smaller radius, resulting in wire-to-wire contact between adjacent windings. The result of an attempt in which the spacers were removed without a heat treatment is shown from overhead in Figure 10, where we can see unacceptable contact between neighboring windings. The heat treatment process, called a stress relief anneal, was used to remove the internal stresses so that the windings “relaxed” into their desired geometry. For the stress relief anneal the entire wrapped spool assembly, including the holding band and C-clamp, was placed into a furnace at 650°F for 1 hour. After the heat treatment, the part was air cooled. This resulted in the wire having the properties of 6061-O aluminum.

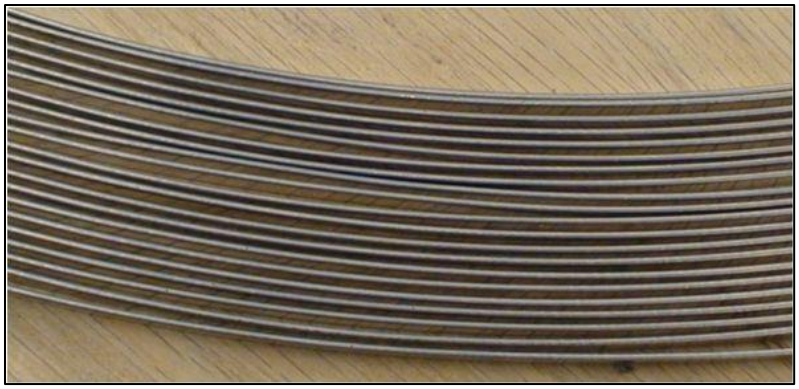

Figure 10 – Undesirable Winding-to-Winding Contact as a Result of No Heat Treatment

After cooling, and with the holding band still in place, the short spacers were removed from the wrapping with the use of a small flathead screwdriver. Care had to be taken when removing these spacers so as not to cause any out of plane bending of the coil wire. The combs (either single-sided or double-sided, depending on what layer number was being made) were then inserted into the windings. A digital caliper was used to center the combs within their notches, in an attempt to have all 8 combs equally spaced around the circumference of the coil. Figure 11 shows an overhead view of a double sided comb installed into the windings. The long spacers, still in place, are also visible on both sides of the spool notch.

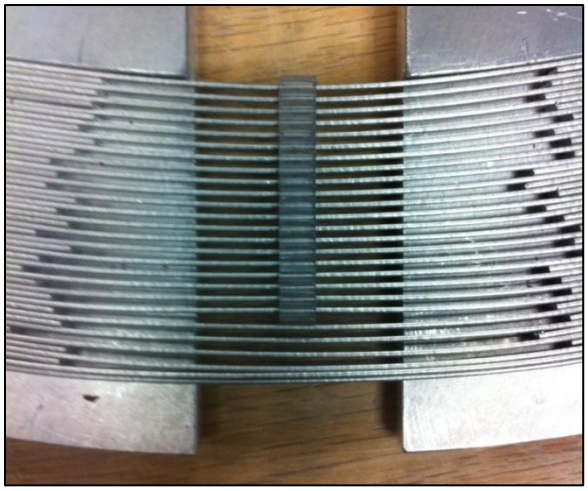

Figure 11 – Short Spacers Removed and Comb Installed into Windings

Next, the combs were glued into place. Permabond 820, a cyanoacrylate adhesive, was chosen because of its good strength retention at higher temperatures. Even at 125 degrees Celsius, the adhesive retains over 70% of its room temperature strength. A syringe was used to apply the adhesive along both long edges of the comb, as shown in Figure 12. This application method was advantageous because it allowed the glue to wick into the small space between the top of the wire and the trough of each comb channel. This wicking behavior was easily seen due to the transparency of the polycarbonate combs. The curing time of the adhesive is only 10-15 seconds, so after a few minutes the combs were securely attached to the windings.

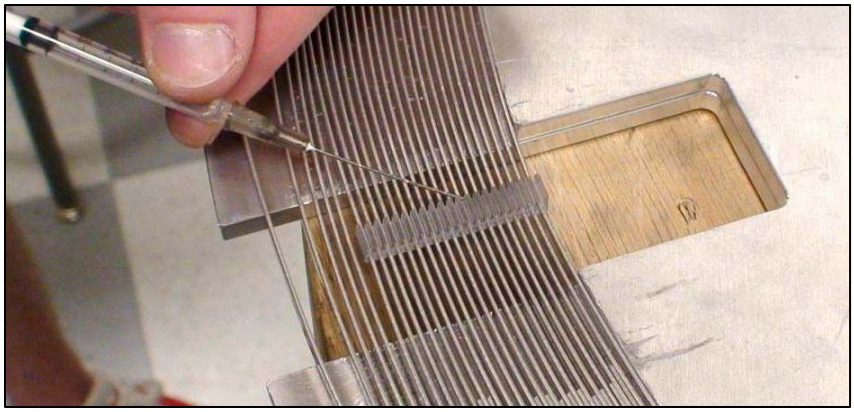

Figure 12 – Gluing a Comb in Place with Permabond 820

With the combs firmly attached to the windings, the next step was to remove the long spacers. Just as with the short spacers, care had to be taken when removing the long spacers to prevent bending the coil windings up and out of the plane of the coil. Then, the entire layer was slid up off of the spool and the excess windings trimmed away. As can be seen in the overhead view in Figure 13, the resulting coil layer had the geometry we desired – a near perfect 0.040" air gap between each winding. Note that in Figure 13 the two nearest combs to this section of windings are just out of view on either side of the image.

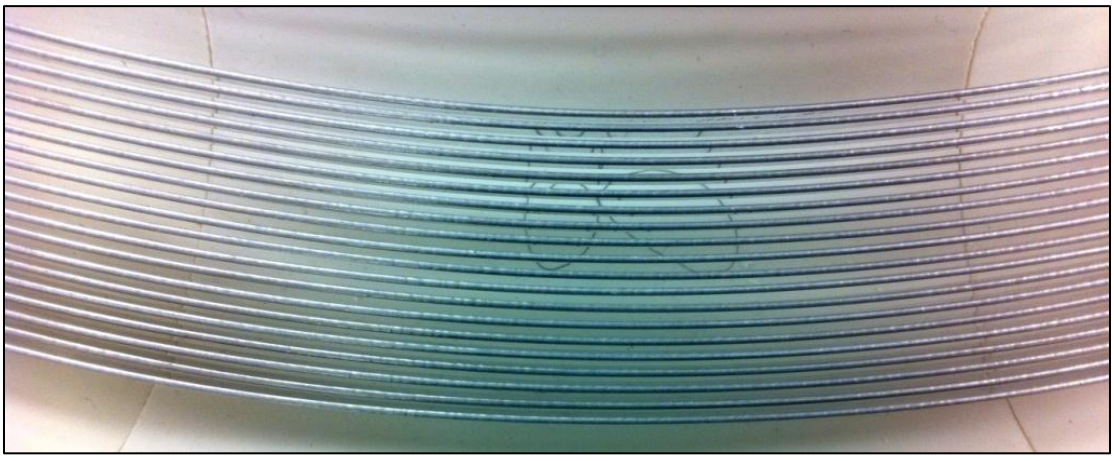

Figure 13 – Coil Layer with Proper Air Gap Between Windings

This process was repeated with the remaining 4 layers, using either double-sided combs or single-sided combs as necessary to construct either an outer layer or an inner layer of the coil stack. After each layer was completed, it was affixed to the previous layer using the same syringe gluing technique. During the assembly of the stack, layers 2 and 4 were flipped over as compared to layers 1, 3 and 5 so that the spiral direction of each layer was opposite to that of its adjacent layers.

The inter-layer electrical connections were made using a combination of silver "tabs" and small pieces of copper sheet. Due to the difficulty associated with making solder connections to 6061, a small rectangular tab of silver sheet was affixed to the outer face of the ends of each layer using high temperature soldering techniques. After the silver tabs were installed, small pieces of copper sheet were easily soldered onto the tabs to make the necessary layer to layer electrical connections. Finally, the electrical connections to the two ends of the coil stack were made by soldering a piece of insulated 12 AWG round copper wire onto the copper sheet. Note that the layers were connected in a manner that resulted in the current flow being in the same circumferential direction in all 5 layers. The overall layout of the coil electrical connections is shown in Figure 14 and Figure 15.

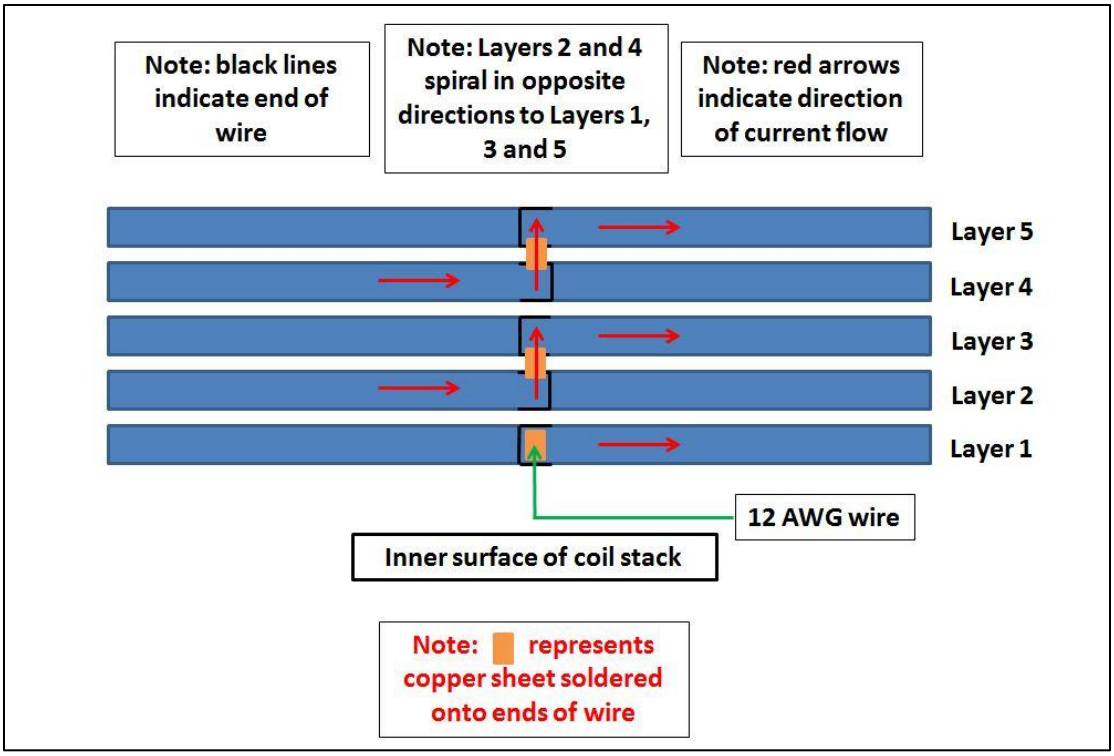

Figure 14 – Electrical Connections on Inner Surface of Coil Stack

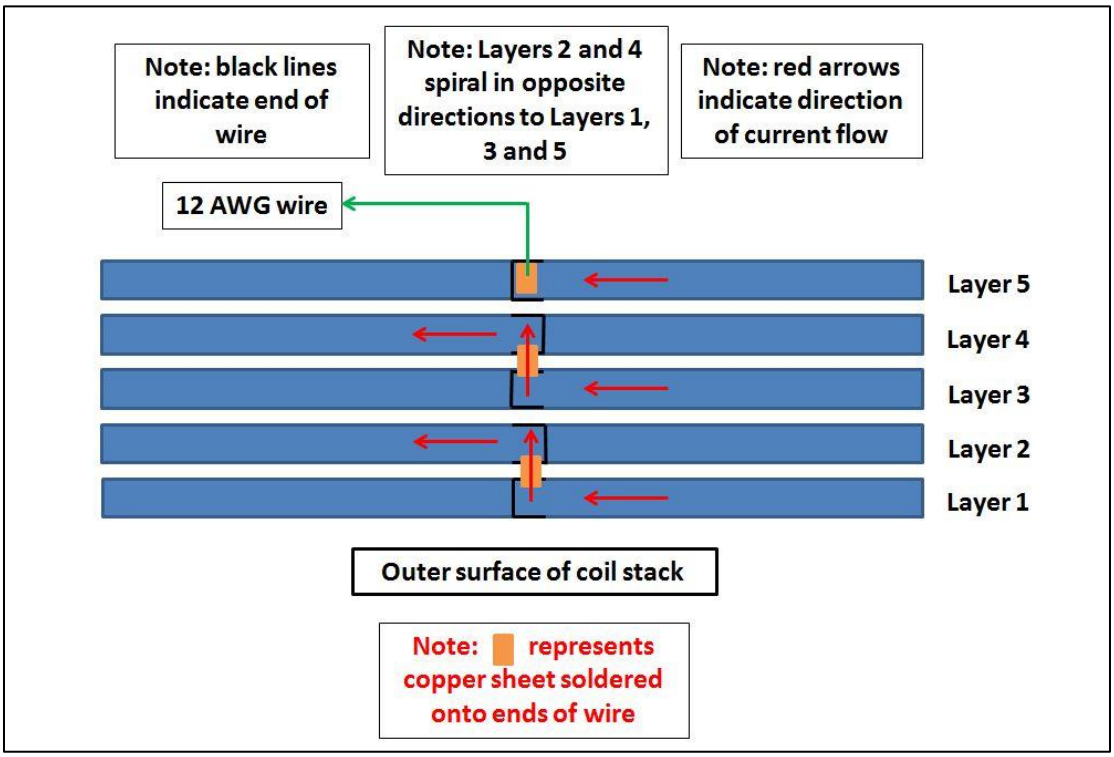

Figure 15 – Electrical Connections on Outer Surface of Coil Stack

2.3: Electrical Testing and Characterization

The AC current flowing through a single winding of the coil will induce eddy currents in the neighboring windings of the coil. These eddy currents cause the impedance of the coil to change with frequency. More specifically, the coil's resistance increases at higher frequencies and its inductance decreases at higher frequencies. These frequency dependent effects are commonly referred to as the proximity effect. An analytical approximation for predicting the AC behavior of coils, known as Dowell's method, is presented in [7].

To measure the effect of increasing frequency on coil resistance and inductance, test capacitors (also called loading capacitors) of various values were connected in series with the coil. The experimental test setup is shown in Figure 16. Two Fluke 87V multimeters were utilized – one connected in series with the load to measure the load current I_L, and the other connected across the load to measure the load voltage V_L. This two-multimeter arrangement allowed for calculating the load impedance as V_L / I_L. For each test capacitor value, the resonant frequency was determined by locating the frequency of minimum load impedance. It should be noted that due to changes in R and L with frequency, the point of minimum load impedance is not guaranteed to be the point of zero reactance, and hence the minimum load impedance may not be purely resistive. However, as will be shown later, for the frequency ranges used in our tests, a numerical analysis shows that the difference between the minimum impedance and the impedance at zero reactance is less than 4%. We therefore assume that the minimum impedance measured is in fact the AC resistance of the coil at each frequency.

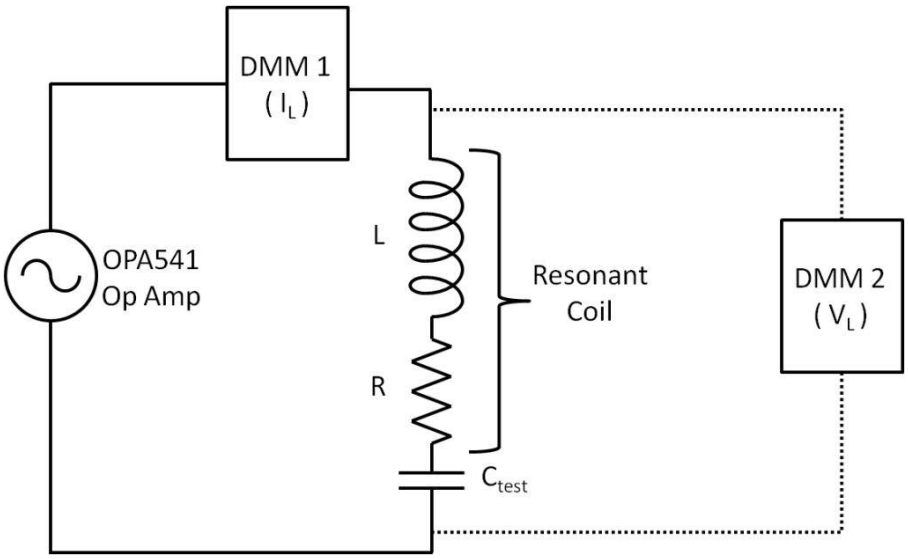

Figure 16 – Test Setup for Measuring Proximity Effect

Another source of possible error in this setup is dielectric losses in the capacitors themselves. However, all loading capacitors used were film capacitors with a metallized polypropylene dielectric. Due to the extremely low dissipation factor of this dielectric, the predicted equivalent series resistance (ESR) for each loading capacitor was less than 1% of the measured load impedance, so these losses were neglected.

The measured AC resistance of the coil at different frequencies is shown in Figure 17. Also shown is the AC resistance as calculated by the Dowell method. The Dowell method equation for resistance is

$$R_{AC} = \frac{m\rho N_l^2 l_T}{\eta b h}\left\{M' + \frac{(m^2-1)D'}{3}\right\} \tag{7}$$

where M' and D' are the real parts of M and D, respectively, with M and D given by

$$M = \alpha h \coth \alpha h \tag{8}$$

and

$$D = 2\alpha h \tanh\frac{\alpha h}{2} \tag{9}$$

with

$$\alpha = \sqrt{\frac{j\omega\mu_0\eta}{\rho}} \tag{10}$$

Note that the notation used here matches that presented in Table 1.

It is clear (see Figure 17, below) that the Dowell method significantly under-predicts AC resistance for our coil cross section. This could be due to the fact that our rectangular conductor has a high aspect ratio a/h, and the Dowell method is better suited for square conductors. Furthermore, the gap between successive turns, u, is not insignificant in comparison to the height of the conductor, h (they are in fact equal), which could be introducing additional errors. As stated in [8], one classical approach to deal with this air gap is to increase the conductor height so that the air gap is eliminated and modify the resistivity such that the DC resistance of the coil remains the same. Making this modification requires us to double the value of h and double the value of ρ. As seen in Figure 17, the modified Dowell method is closer to the experimentally measured values, but still under-predicts the AC resistance.

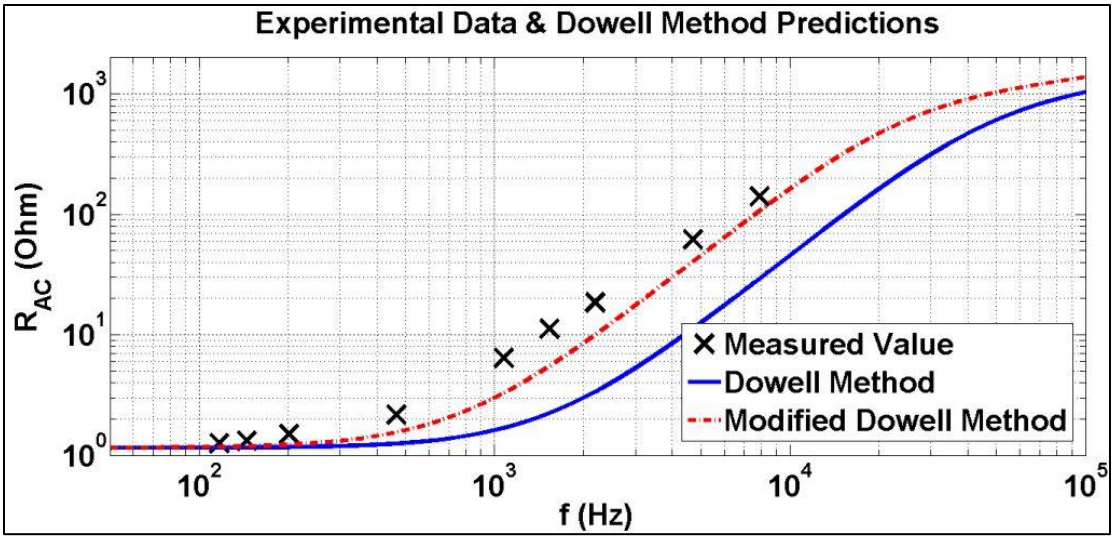

Figure 17 – Frequency Dependent Behavior of Coil Resistance

The capacitance of each test capacitor was also measured with a Fluke 87V multimeter. With these capacitance measurements, it was possible to calculate the coil inductance at each resonant frequency. These AC inductance values are plotted in Figure 18. Dowell's method also provides a prediction for coil inductance versus frequency, which is given as the sum of two components. The first component, L_U, is the contribution from the gap between layers and is frequency independent. The second component, L_ω, is called the AC leakage inductance and is dependent on frequency. The Dowell method equation for inductance is

$$\begin{aligned} L_{AC} &= L_U + L_\omega \\ &= \left(\frac{\mu_0 m^2 N_l^2 l_T (m-1) u}{3b}\right)\left(1 - \frac{1}{2m}\right) \\ &+ \frac{\mu_0 m^3 N_l^2 l_T h}{3b}\left\{\frac{3M'' + (m^2-1)D''}{m^2|\alpha^2 h^2|}\right\} \end{aligned} \tag{11}$$

where M'' and D'' are the imaginary parts of M and D, respectively.

Total coil inductance, $L_U + L_\omega$, is plotted in Figure 18. We can see that while the DC inductance L_U predicted by Dowell's method is lower than what was determined experimentally, the measured data does follow the predicted trend somewhat qualitatively. However, the Dowell method does not predict any significant decrease in inductance until 10 kHz, whereas the measured values start to show an inductance decrease beginning around 1 kHz.

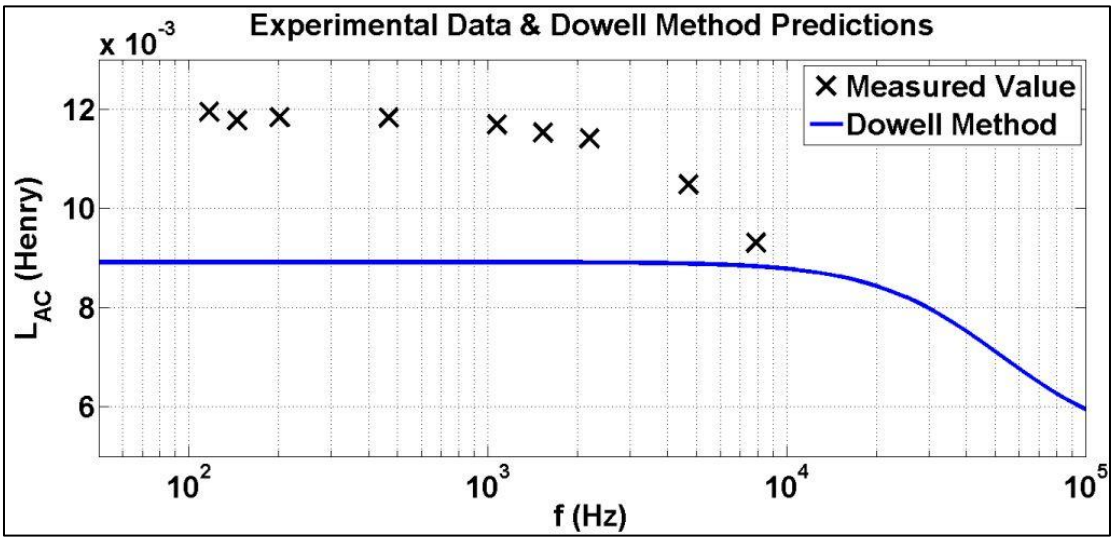

Figure 18 – Frequency Dependent Behavior of Coil Inductance

Since we expect the measured data to follow a Dowell-like trend at least qualitatively, a "Dowell method curve fit" was applied to the experimental data for resistance and inductance. The two curve fits follow the Dowell method equation forms given in equations (7) and (11). For the resistance fit, the number of layers was set to 20 and η and h were set as the free parameters. For the inductance fit, the number of layers was again set to 20 and η, h, L_U, and $L_{\omega 0}$ were set as the free parameters. Both curve fits, shown in Figure 19 and Figure 20 below, match the data well and have an R^2 value greater than 0.99.

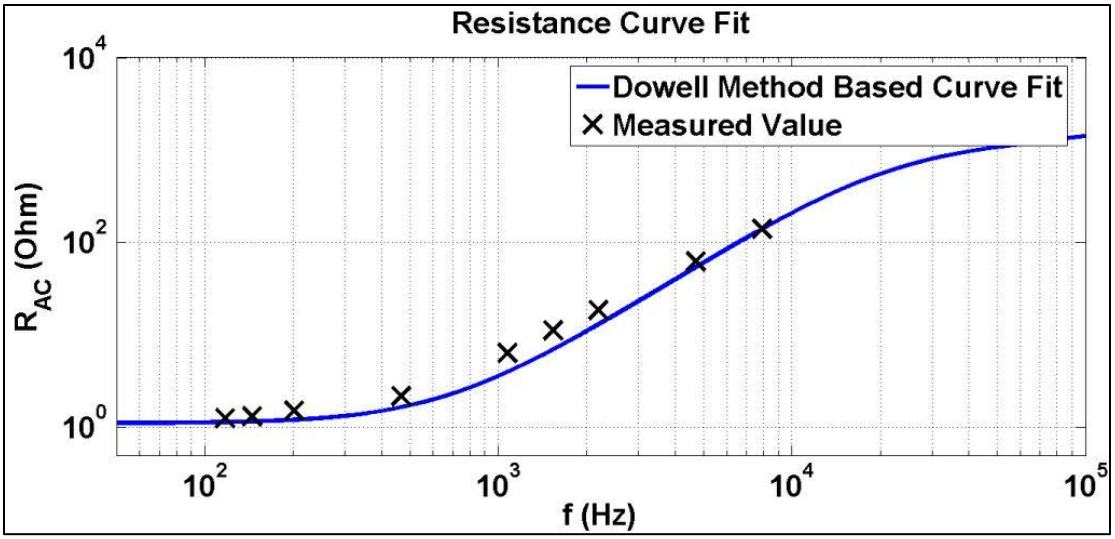

Figure 19 – Curve Fit Applied to Measured Resistance Data

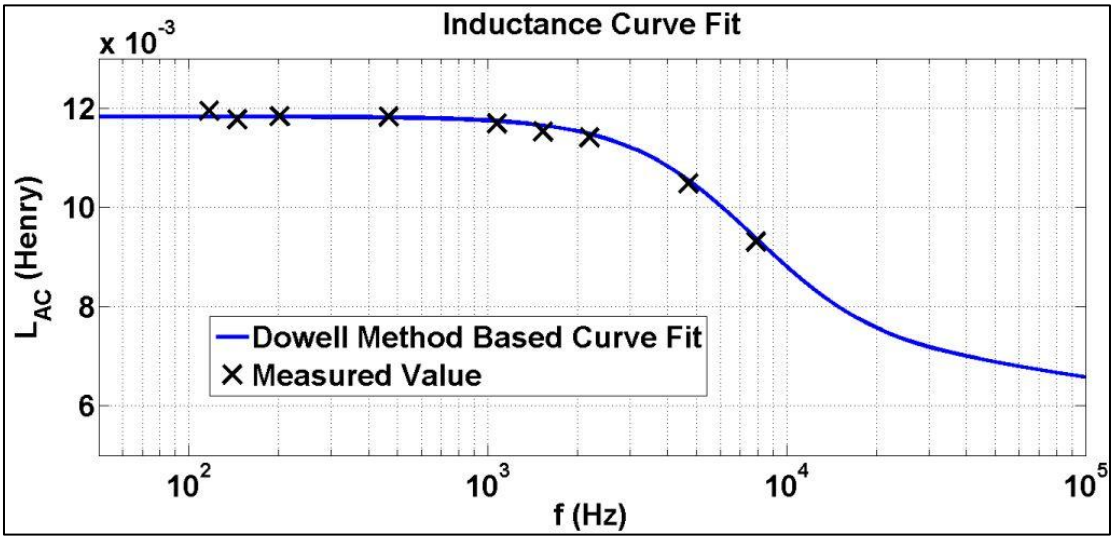

Figure 20 – Curve Fit Applied to Measured Inductance Data

As mentioned earlier, the dependence of R and L on frequency can theoretically lead to a discrepancy between the frequency of minimum impedance and the frequency of zero reactance. Using the curve fits for resistance and inductance, a MATLAB script was written to numerically calculate the magnitude of this discrepancy. The script loops over a frequency range of 1 Hz to 8 kHz in 1 Hz increments. The procedure for each loop iteration is then as follows:

1. Given a frequency f, use the inductance curve fit to calculate the AC inductance of the coil at that frequency. Then, calculate the capacitance C required to make f the zero-reactance frequency of the system, given by

$$C = \frac{1}{L_{ZR}(2\pi f_{ZR})^2} \tag{12}$$

where we have called the AC inductance result from the curve fit L_{ZR}, as this is the value of the coil's inductance at the frequency of zero reactance.

2. Create an additional frequency sweep vector f_{sweep} which has a range of 0.5*f to 1.5*f.
3. Use the inductance and resistance curve fits to calculate L_{AC} and R_{AC} at each point in f_{sweep}.
4. Calculate the impedance at each point in f_{sweep} by

$$Z = \left| 2j\pi f_{sweep} L_{AC} + R_{AC} + \frac{1}{2j\pi f_{sweep} C} \right| \tag{13}$$

5. Numerically locate the frequency in f_{sweep} at which the impedance is minimum. This value is the minimum impedance of the circuit, called Z_{MinZ}.
6. At the frequency corresponding to Z_{MinZ}, use our inductance and resistance curve fits to calculate the inductance at minimum impedance, called L_{MinZ}, and the resistance at minimum impedance, called R_{MinZ}.

The results of the investigation are shown in Figure 21. The solid blue line represents the discrepancy between the value of minimum impedance, Z_{MinZ}, and the AC resistance of the coil, R_{MinZ}, at the same frequency. Up to 8 kHz, which was the highest measured frequency, the difference is less than 4%, so we conclude that it is sound to assume that the measured values of minimum impedance are equal to the AC coil resistance. The dashed red line represents the discrepancy between the coil inductance at minimum impedance, L_{MinZ}, and the coil inductance which corresponds to zero reactance, L_{ZR}. At frequencies less than 8 kHz, the difference is less than 1.5%, so we also proceed with the assumption that the measured inductance values are accurate.

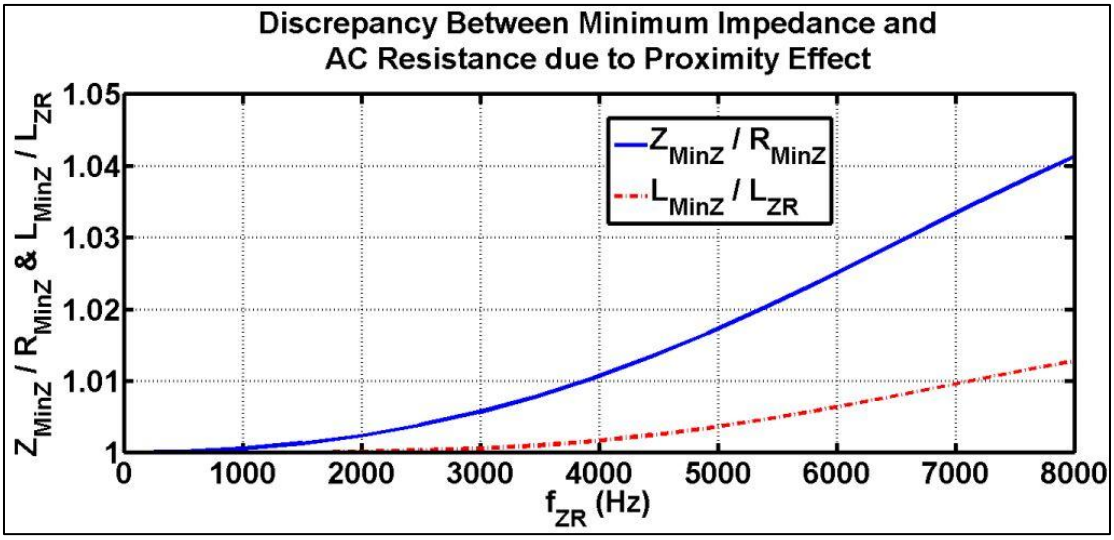

Figure 21 – Comparison of Minimum Impedance and Zero Reactance for Resonant Coil Circuit

Chapter 3: Housing and Interior Components

3.1: Housing Design

3.1.1: Structural Requirements and Design

The choice for the basic shape of the RINGS housing – a torus which encompasses the resonant coil – was a natural consequence of the shape of the resonant coil itself. This torus design was split into two halves, allowing the interior components to be assembled in the bottom half before the final step of installing the top half of the housing. This split housing concept is illustrated in Figure 22.

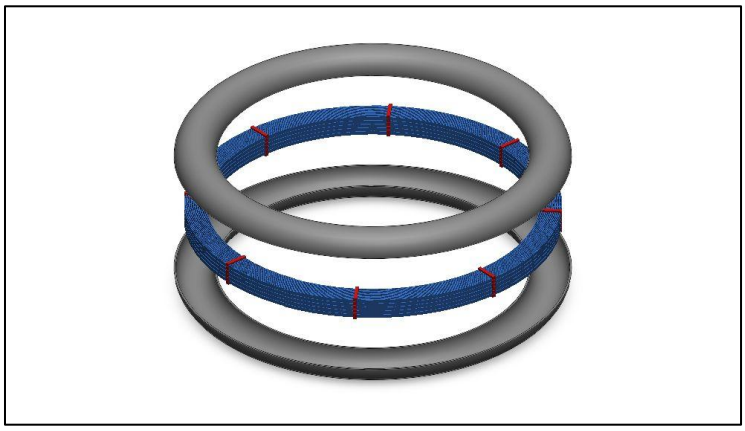

Figure 22 – Split Torus Housing Concept

NASA voiced early concerns about the risk of possible crew contact with the high voltage resonant coil, so it was decided to use a lap joint design at the interface between the top and bottom housing halves. This overlapping joint provides a good means of preventing access to the interior of the housing. To avoid occlusion of the infrared sensors and cold gas thrusters located on the SPHERES satellite, the minor diameter of the torus was set to 3". This also provided ample room around the

resonant coil for wire routing and the placement of interior components. A conceptual cross section of the two housing halves encompassing the resonant coil is shown in Figure 23.

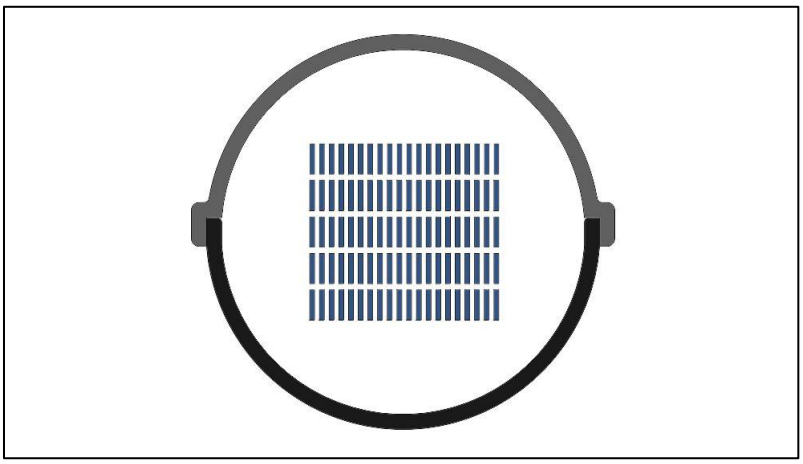

Figure 23 – Cross-Sectional View of Housing Halves and Resonant Coil

Due to the high costs associated with manufacturing the housing via injection molding, it was decided instead to use vacuum forming techniques. In vacuum forming, a flat sheet of plastic material is heated to a temperature at which it is pliable and then lowered around a mold. A vacuum is then created between the sheet and the mold, drawing the plastic into the desired shape. As a consequence of this manufacturing method, the part must be designed with uniform thickness throughout. Additionally, the finished part may exhibit localized thinning of the plastic in areas of high deformation. Also, the final part will have a much better tolerance on the side of the plastic which is in contact with the mold. To ensure a tight tolerance at the lap joint, the housing bottom was made on a female mold and the housing top was made on a male mold. This ensured that the exterior surface of the housing bottom and the interior surface of the housing top both had tight tolerances, producing a good fit at the lap joint.

NASA encouraged the use of polycarbonate for the housing material due to its low outgassing properties and its high resistance to impact and fracturing. To determine the necessary housing thickness, a finite element analysis (FEA) simulation was performed for two different static loading scenarios. For simplicity, the housing in both analyses was modeled as a hollow, one-piece torus, and the simulations were carried out using SolidWorks Simulation.

The first loading scenario, known as the "push-off load," was based on a NASA requirement. This setup is representative of the loads created when a crew member pushes on the housing while it is attached to an ISS wall for stowage. The requirement nominally calls for an application of 125 lbf over an area of 4 in^2. However, due to the curvature of the housing wall, this load was applied over a 2" x 1" rectangle located on the top face of the housing, as this was more representative of the actual contact area in a push-off scenario. An annulus having a thickness of 0.25" and located on the opposite face of the housing was used as the constrained area, as it was felt this was a good approximation for the contact area between the RINGS housing and the ISS wall. The loading setup and results of the FEA simulation are shown in Figure 24. With a shell thickness of 0.080", the minimum factor of safety (FOS) based on the yield strength of polycarbonate was found to be greater than 2.

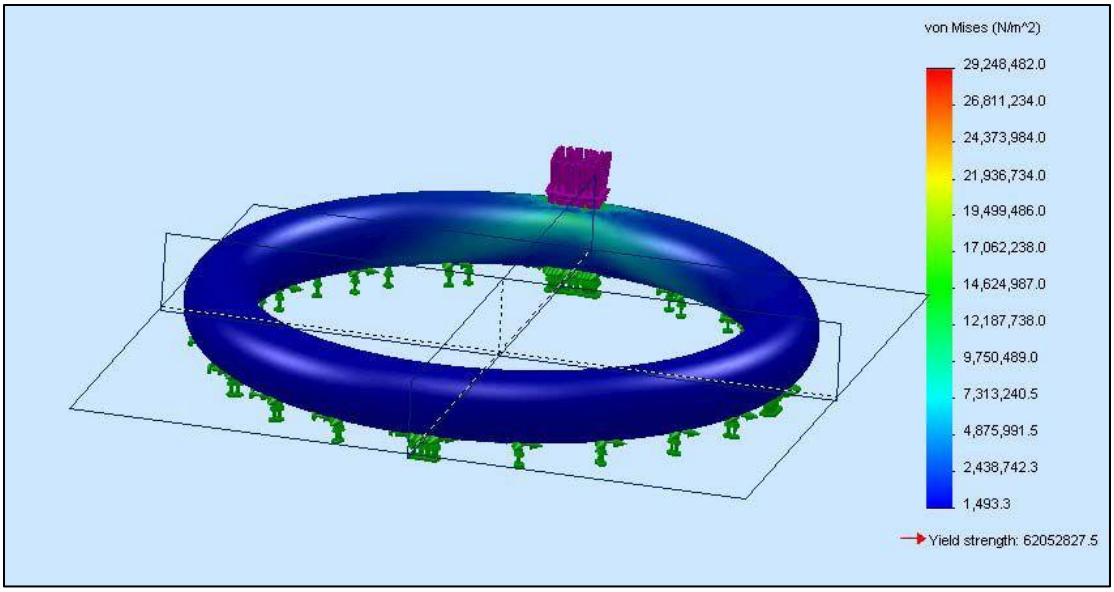

Figure 24 – FEA Analysis of Push-off Loading Scenario

The second FEA analysis is known as the "pick up quickly" loading scenario and is more applicable to the handling of the housings before launch than it is to operations on the ISS. This setup is representative of a situation in which the housing is picked up with two hands and swiftly accelerated upwards. Two 45 lbf loads were each applied over a 1" x 1" area, and these two areas were diametrically opposed to one another on the underside of the torus. These loads are a highly conservative estimate that model the resonant coil as dead mass under a 2.5g acceleration. Two diametrically opposed constraints were also placed on the underside of the torus, having an area of 1" x 1". The loading setup and results of the FEA simulation are shown in Figure 25. With a shell thickness of 0.080", the minimum FOS based on the yield strength of polycarbonate was found to be greater than 6.

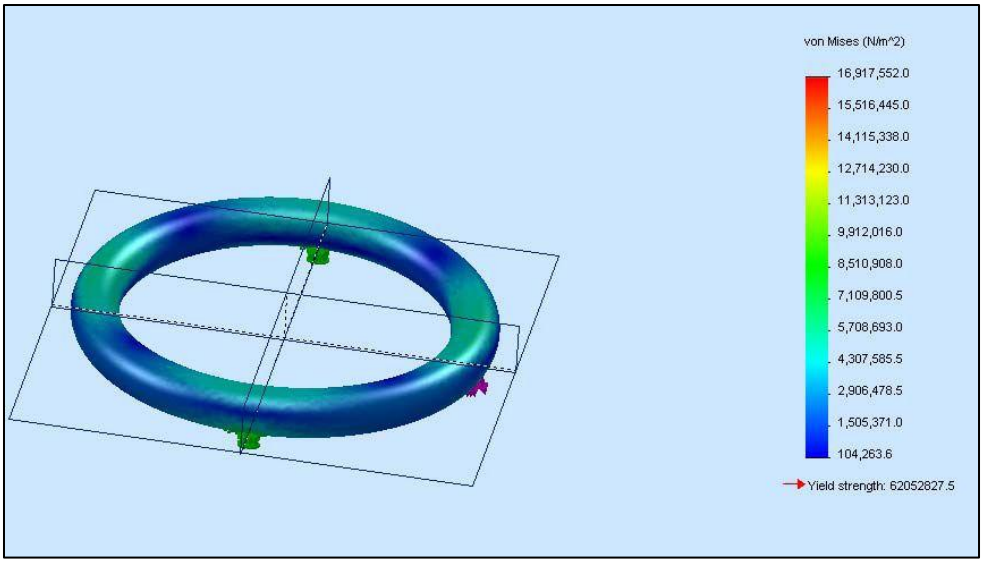

Figure 25 – FEA Analysis of Pick Up Quickly Loading Scenario

It should be noted that both of these loading scenarios are overly conservative since the interior components of the housing provide additional structural rigidity. Using these results, a housing thickness of 0.125" was chosen, which is a readily available size for polycarbonate sheets. It was estimated that localized part thinning could reduce this thickness to as low as 0.080" in some places, which was deemed acceptable based on our FEA results for a 0.080" thick housing.

3.1.2: Cooling Requirements and Thermal Design

The next step in designing the housing was a thermal analysis used for the sizing of the cooling fans. At the maximum design current of 18 amps RMS, the predicted power dissipation in the coil was calculated to be approximately 315 watts. Due to the absence of natural convection in the microgravity environment onboard the ISS, all of this power must be removed via forced convection using fans. It was assumed the temperature of the entering air was 75°F (24°C) and a nominal exit air temperature of 100°F (38°C) was prescribed. NASA requirements dictated that the

exiting air have a temperature less than 115°F, so this choice provided additional margin. The power required to increase the temperature of the air is then given by

$$P = \dot{m}_{air} c_p \Delta T \tag{14}$$

where $\dot{m}_{air}$ is the air mass flow rate in kg/s, c_p is the specific heat capacity of air at constant pressure in J/(kg·K), and ΔT is the difference between the temperature of the entering air and exiting air in °C. The required mass flow rate is then

$$\dot{m}_{air} = \frac{P}{c_p \Delta T} = \frac{315}{1005(38-24)} = 0.022 \frac{kg}{s} \tag{15}$$

Assuming an air density of 1.10 kg/m^3, which is slightly lower than the density of air at 38°C to provide additional margin, the corresponding volumetric flow rate is

$$\dot{V}_{air} = \frac{\dot{m}_{air}}{\rho_{air}} = 0.020 \ \frac{m^3}{s} = 42 \ \frac{ft^3}{min} \tag{16}$$

With the necessary volumetric flow rate calculated to be 42 cubic feet per minute (CFM), the NMB 1604KL-04W-B50-B00 fan was selected. This box shaped fan produces a nominal flow rate of 6 CFM and has dimensions of 40mm x 40mm x 10mm. This small size and thin profile allowed for easy integration into the housing wall. From the energy analysis, only 7 fans are required, but it was decided to include 10 fans to provide additional margin. Eight of these 10 fans are located on the outer surface of the housing, spanning the joint between the two housing halves. The remaining two fans are located on the oblique walls of the "powerbox" area of the housing, which is discussed in more detail in Section 3.1.3. A conceptual overhead view of the fan locations is shown in Figure 26.

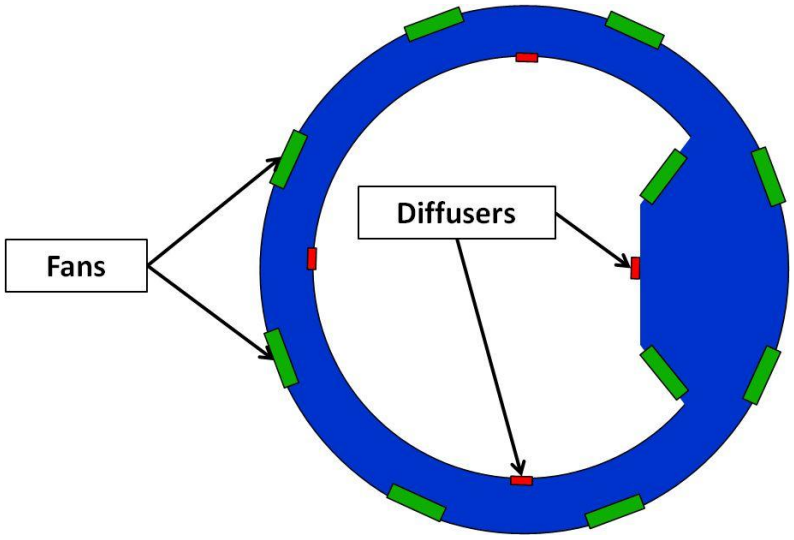

Figure 26 – Fan and Diffuser Locations

Also shown in Figure 26 are the locations of the four exit air diffusers. The diffusers are located on the inner face of the torus and consist of a simple matrix of drilled holes, as shown in Figure 27. By placing them on the inner face, the exiting air impinges on the SPHERES satellite. This is advantageous because the net momentum gain from the exiting air is zero, eliminating a possible source of error from EMFF operations. Additionally, the exit air diffusers are offset from the outer fan locations so that the cooling air is forced to travel some distance in the circumferential direction within the housing, which serves to improve the cooling of the resonant coil.

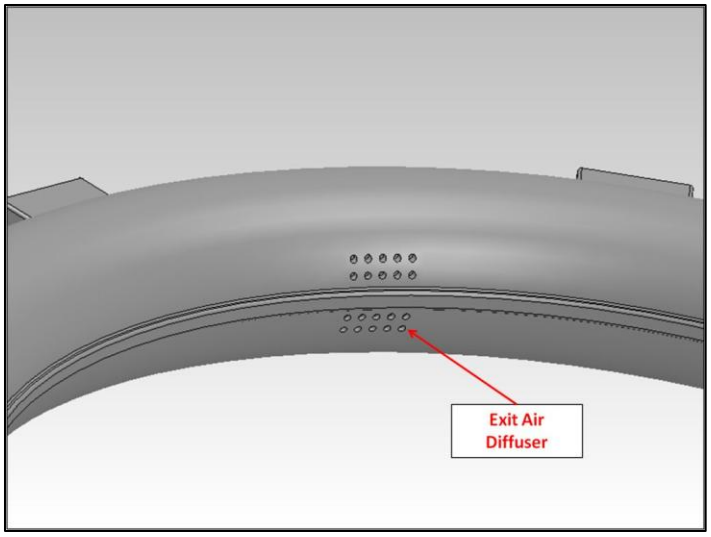

Figure 27 – Exit Air Diffuser

To facilitate the mounting of the outer housing fans, a molded boss feature was designed into the housing which can be seen in Figure 28. The boss extends outward and away from the resonant coil so that space within the housing is preserved. Additionally, the lap joint design is carried through into the fan boss. A hexagonal cutout in the boss allows for entering air to be drawn into the fans. Surrounding the cutout are four screw holes that allow for the installation of the fan and finger guard, as well as provide the means for securing the two housing halves together. More details on the fan mounting and housing closure methods are discussed in Section 3.2.2.

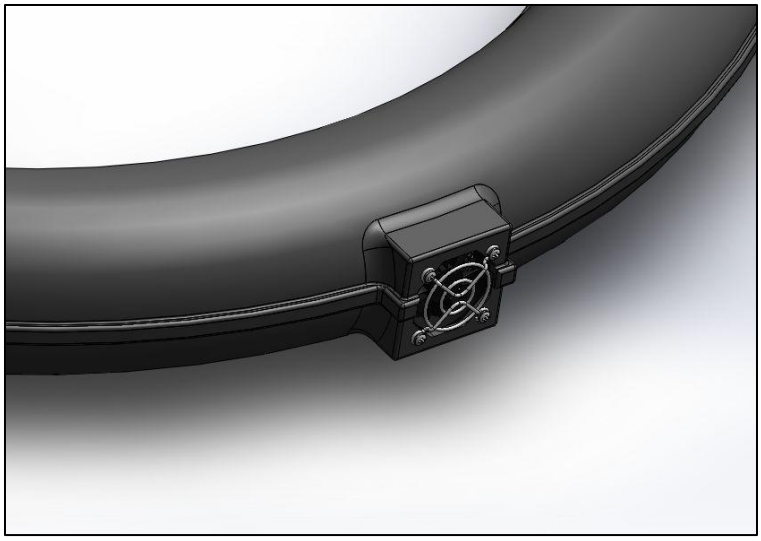

Figure 28 – Outer Fan Boss

3.1.3: Electronics Box

With the torus diameter and housing cross section dimensions finalized, our colleagues at Aurora Flight Sciences (AFS) proceeded to design the RINGS to SPHERES support structure. The support structure consists of four struts, four cuffs, and a mating sleeve. Each of the four struts extend radially outward from the mating sleeve and attach to a cuff. The cuffs are made from two halves in the same manner as the RINGS housing. After the housing top is installed, the top cuff is bolted to the bottom cuff and to the strut. The support structure assembly is shown with a SPHERES satellite installed in Figure 29. For reference, the SPHERES satellite is shown in blue, the mating sleeve in red, the four struts in black, and the four cuffs in yellow.

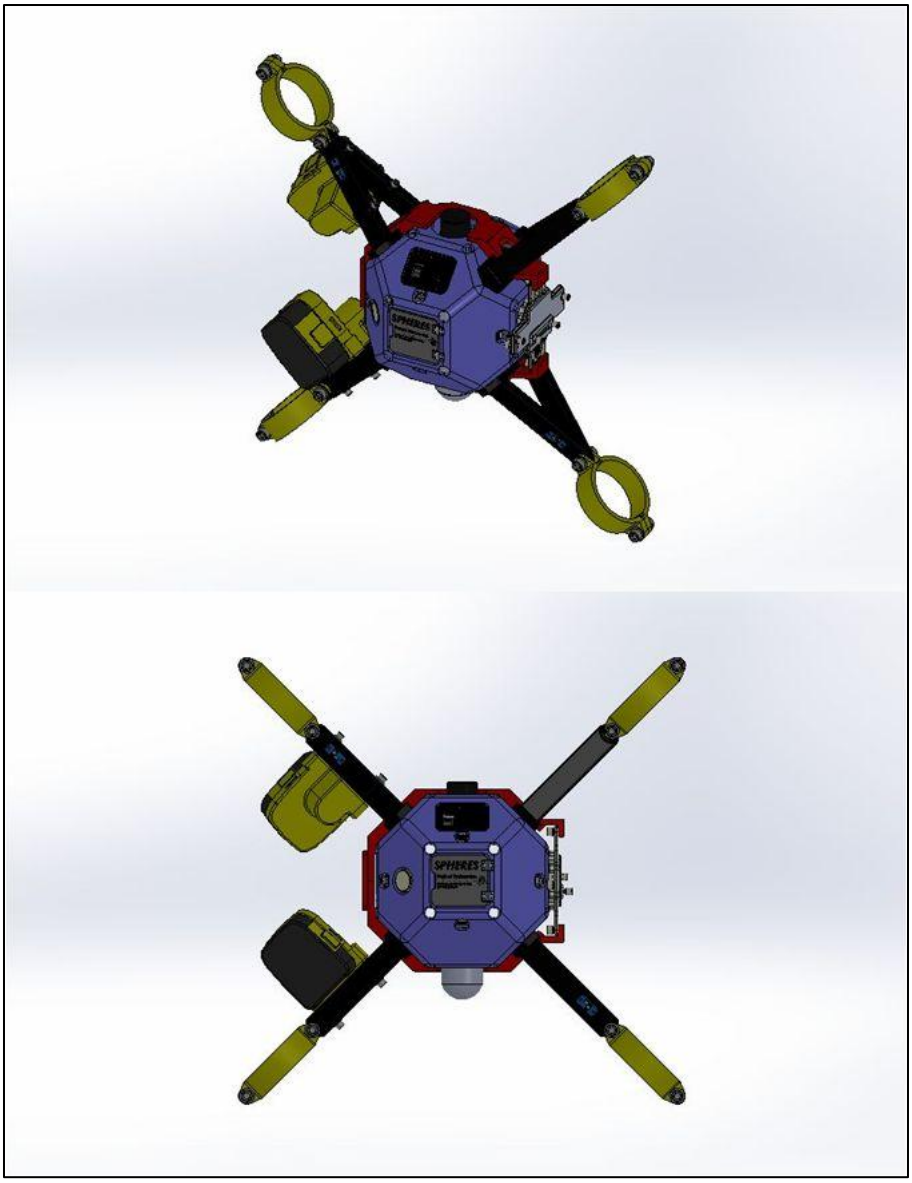

Figure 29 – Support Structure and SPHERES Satellite

Also shown in Figure 29 are the two RINGS batteries installed into their battery mounts. These batteries, part number DC9180 made by DeWalt, have a nominal output voltage of 18 volts and a capacity of 2.2 amp-hours. Located opposite the two battery mounts is the SPHERES expansion port interface, which RINGS connects two with a 50 pin cable to facilitate communication between RINGS and SPHERES. The "powerbox" portion of the housing, which provides space for the

RINGS electronics, was placed in the quadrant nearest the expansion port for two reasons. First, having the powerbox near the expansion port meant that the SPHERES to RINGS communication cable would not have to be undesirably long, making the installation of this cable easier for the RINGS operators. Additionally, since the batteries shift the center of mass of the assembly away from its geometric center, placing the RINGS electronics opposite them helps to bring the center of mass back closer towards the center of the satellite.

The powerbox was designed to provide the maximum possible volume within its quadrant. However, a gap of just over 1.5" was left between the powerbox and the expansion port to allow for the installation of the communications cable. A similar sized gap was left between the two struts and the oblique walls of the powerbox to provide room for strut installation and clearance for the two fans located on the oblique walls of the powerbox. The height of the powerbox was set to 3", the same as the height of the torus cross section, so as not to occlude the infrared or ultrasound sensors on the SPHERES satellite. To accommodate the installation of various electronic components, several cutouts were designed into the face of the powerbox. The final design of the RINGS housing, attached to the support structure, is shown in Figure 30.

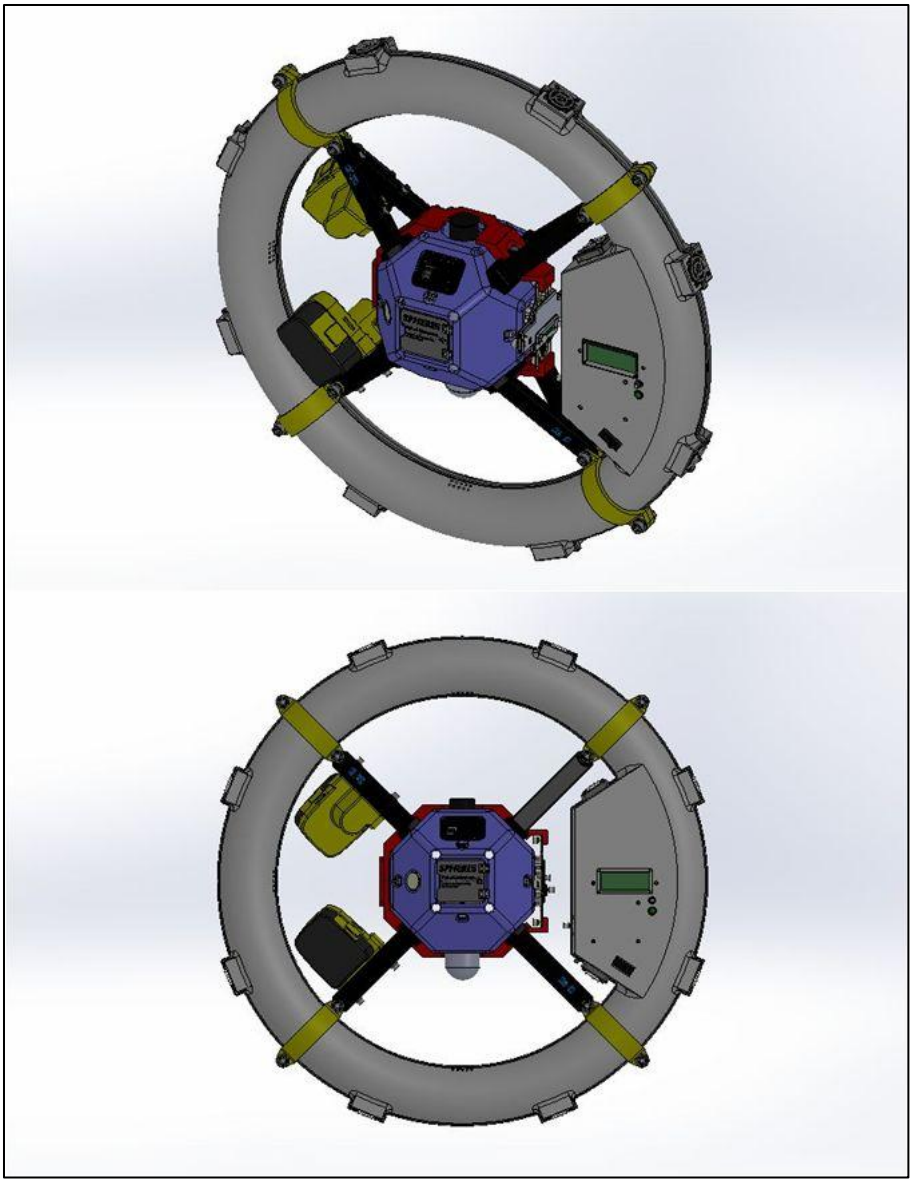

Figure 30 – Final Design of RINGS Housing Attached to Support Structure

3.2: Interior Component Design

3.2.1: Mounting the Resonant Coil

The resonant coil is secured within the housing using a series of polycarbonate parts known as "comb supports." As shown in Figure 31, the comb support has a curved surface on its underside which is machined to the same radius as the housing

wall. On the top surface, a groove is designed to capture the portion of the single sided combs that extend above and below the outer layers of the resonant coil. In addition, a cut through the center of the underside of the part provides an area for routing various wires within the housing.

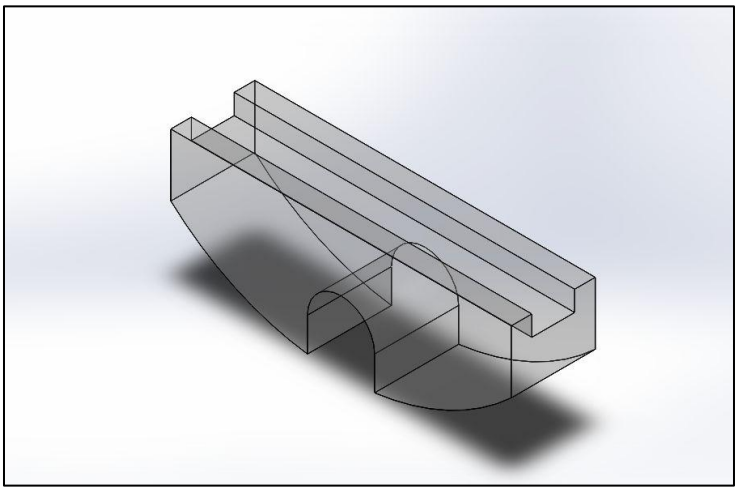

Figure 31 – Comb Support

Eight of these comb supports are glued into each housing half, for a total of 16 per RINGS vehicle. The adhesive used is Permabond 820, the same as was used for attaching the combs to the resonant coil wire. An exploded and collapsed view of the comb support setup is shown in Figure 32, with the comb supports shown in yellow for clarity.

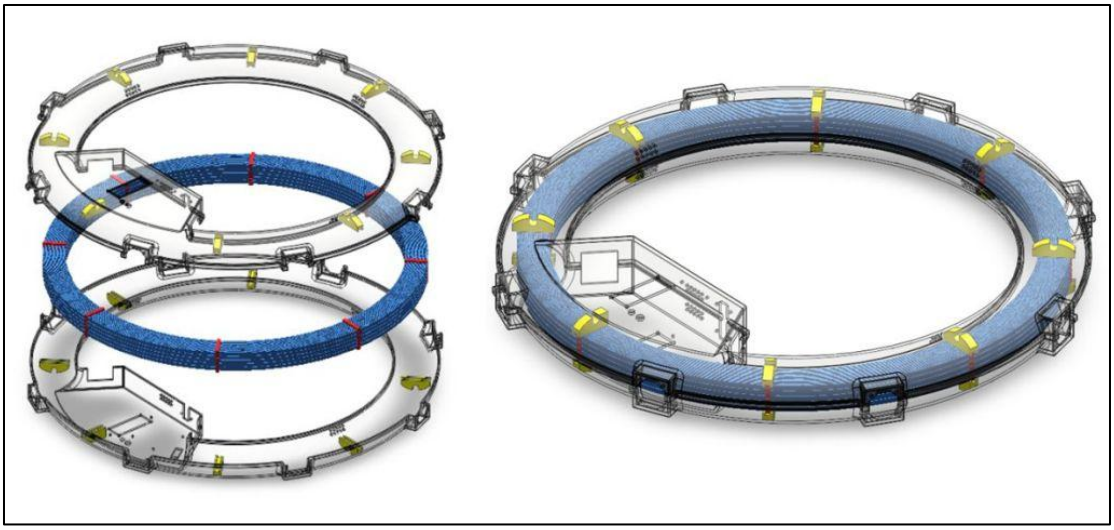

Figure 32 – Comb Support Setup

3.2.2: Flow Guide Fins

There are two types of "flow guide fins" installed in the RINGS housing: inner fins and outer fins. The fins serve two purposes. First, they act as a physical barrier between the airflow cutouts in the housing and the high voltage resonant coil. More specifically, they prevent line of sight access to the resonant coil through the outer housing fan cutouts and the exit air diffuser holes. This prevents the operators from contacting the resonant coil with a finger or a tool such as a screwdriver. The second purpose of the fins is to control the flow direction of the cooling air inside the housing to enhance cooling performance.

The inner fins are curved pieces made from 1/16" thick polycarbonate sheet. Three identical inner fins, which are mounted to four inner fin mounts, are used in the housing to block access to the resonant coil through the exit air diffusers. An inner fin and an inner fin mount are shown in Figure 33. The inner fin mounts are also made from polycarbonate, and they are glued to the bottom half of the housing using

Permabond 820. The curved face on the back of the inner fin mounts matches the curvature of the housing wall, and the small flat portion of this curved face mates to the flat section at the top of the housing bottom to ensure they are accurately located during installation. The front of the inner fin mount features a flat face to which the ends of the inner fins are adhered with Permabond 820. Additionally, a cutout through the center of the inner fin mount provides an area for wire routing.

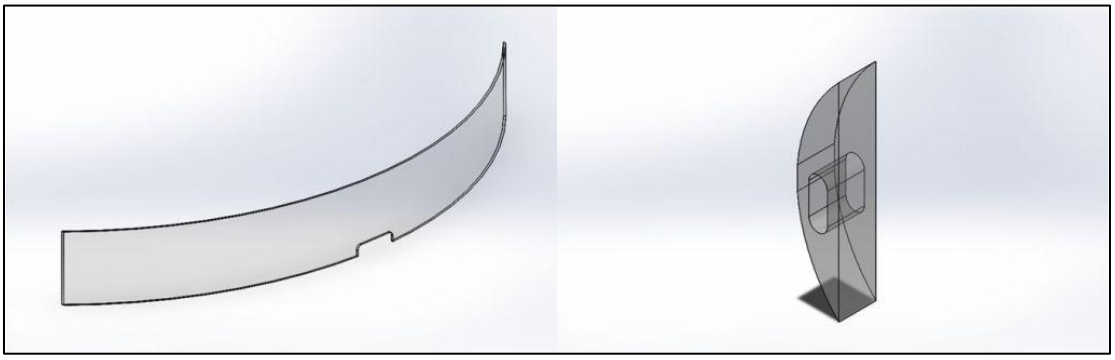

Figure 33 – Inner Flow Guide Fin and Inner Fin Mount

The three inner fins are mounted end to end in the housing, as shown in the exploded and collapsed views in Figure 34. Though small, the inner fin mounts can be seen in the left image of Figure 34, where they are displayed already mounted to the housing bottom.

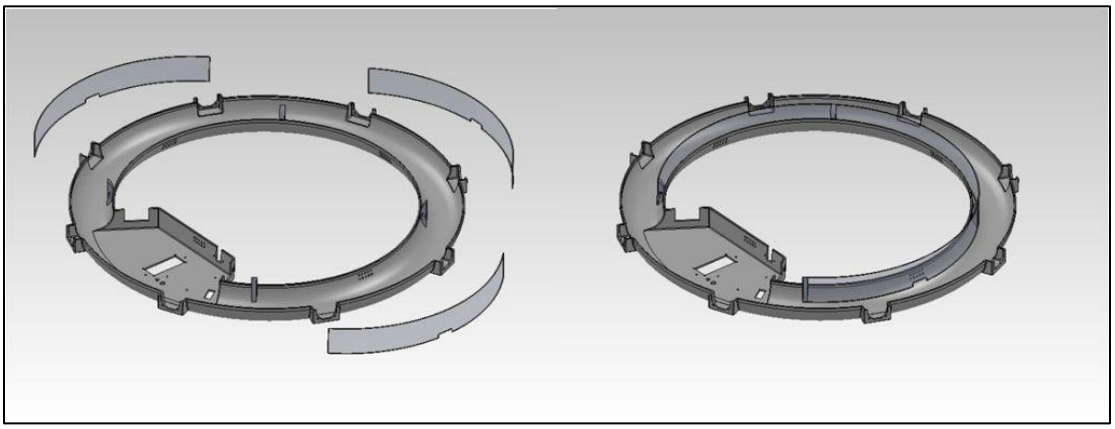

Figure 34 – Inner Fin Setup

The outer fins are similar to the inner fins and are also made from 1/16” thick polycarbonate sheet. A total of eight outer fins are used in the housing to prevent access to the resonant coil through the outer fan inlets. As opposed to the inner fins, which are curved into shape using a heating process before installation, the outer fins are straight pieces. By joining the eight outer fins end to end into a ring, the pliable fins are curved into their appropriate shape. An outer fin and the assembled outer fin ring are shown in Figure 35.

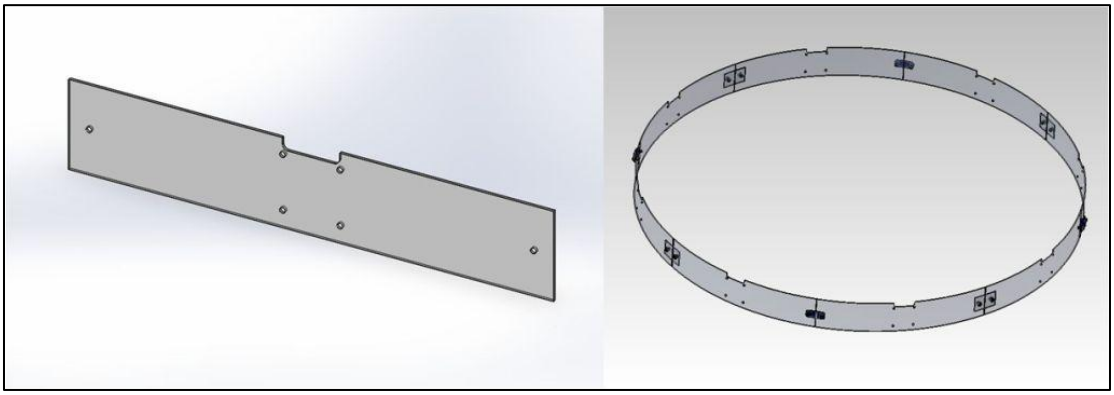

Figure 35 – Outer Fin and Outer Fin Ring

There are a total of eight end to end joints in the outer fin ring. Four of these joints are held together with a small polycarbonate piece. Two #4-40 stainless steel screws and two steel nuts with nylon inserts (for back-out prevention) are used to hold the outer fin joint to the outer fins. The remaining four joints are connected using an infrared sensor (IR) board. The same screws are used to mount the IR board, but two 1/8” long steel spacers are included to provide clearance for the surface mount components located on the rear side of the IR board. Figure 36 shows the two different types of outer fin joint connections.

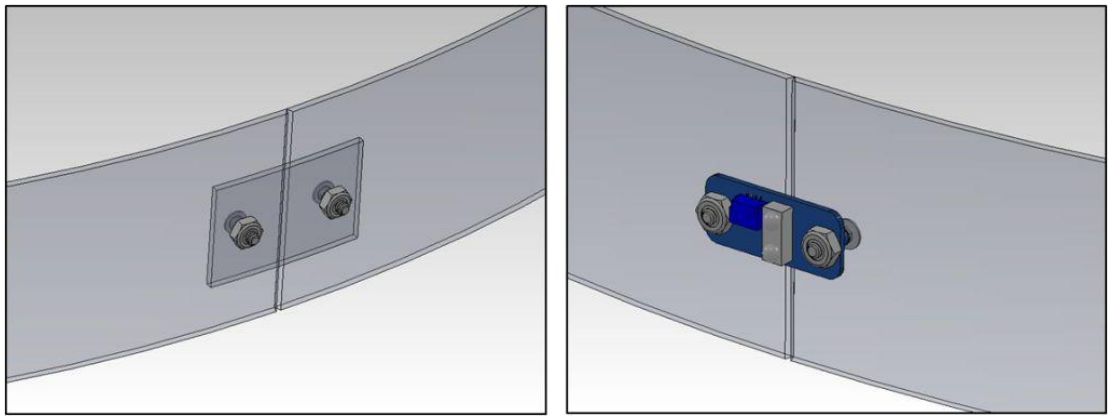

Figure 36 – Outer Fin Joint Connections

Once assembled, the outer fin ring is placed into the housing as shown in Figure 37. Note that no glue is used to install the outer fin ring. Rather, it is held in place by the outer housing screws which also serve to hold the outer fins in place and to attach the housing top to the housing bottom.

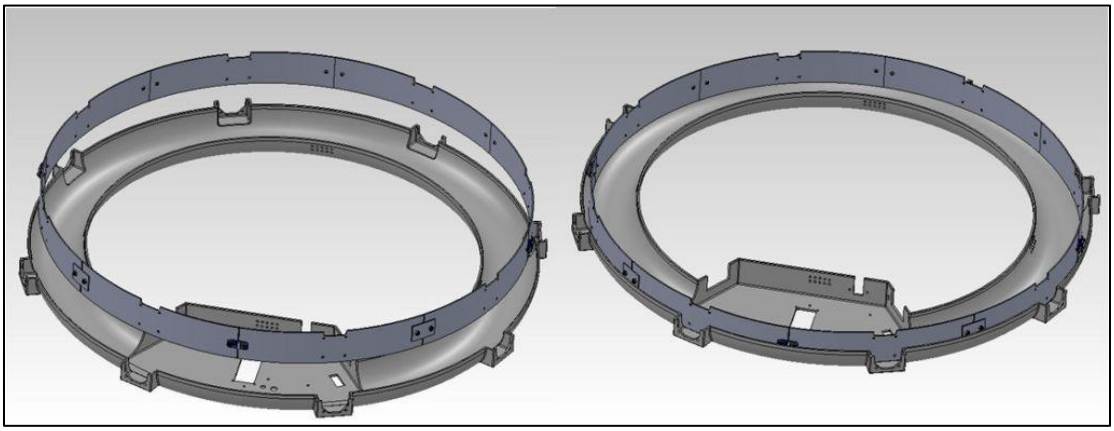

Figure 37 – Outer Fin Setup

In the center of each outer fin are four screw holes. A #4-40 stainless steel screw is inserted through each screw hole from the inner face of the fin and threaded into a #4-40 threaded polycarbonate standoff. Next, a 1/8” long #4-40 nylon set screw is threaded into the standoff through the open end. The fans are then placed in the housing. The outer end of the standoffs sit inside four recesses on the inner face

of the fans, preventing the outer fin ring from rotating in the circumferential direction and properly locating the outer fans in the housing. Finally, after the housing top is installed, four #4-40 stainless steel screws are inserted through the steel finger guards, the housing screw holes, and the fan screw holes, and are then threaded into the open end of the polycarbonate standoff. An exploded view of this design is shown in Figure 38.

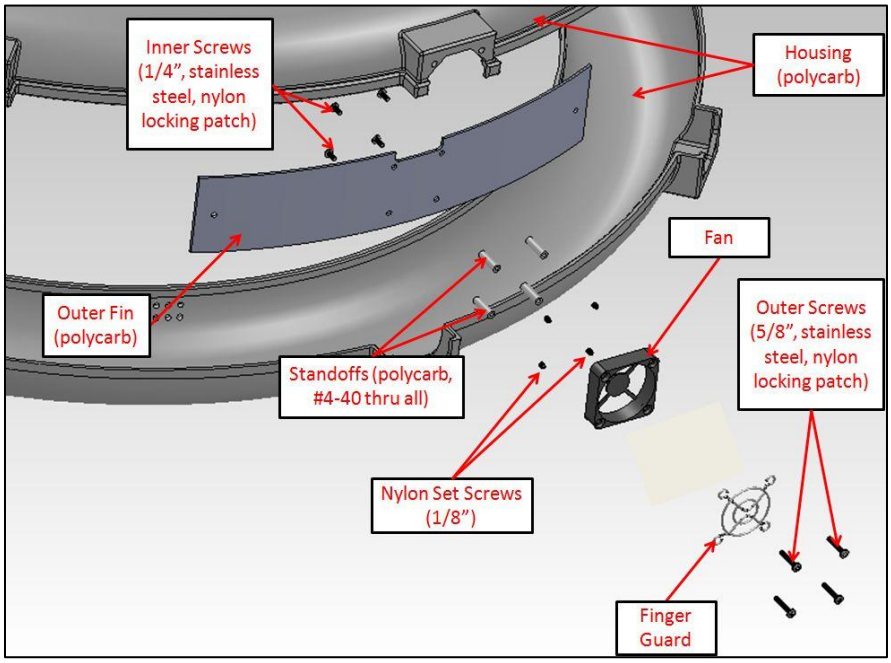

Figure 38 – Outer Fan Mounting Setup

Polycarbonate and nylon were used for the standoffs and set screws to provide electrical insulation between the inner screw head and outer screw head. In the unlikely event that the inner screw head contacts the resonant coil, this design guarantees that the outer screw head, which is accessible to the crew, is well insulated from the resonant coil. For back-out prevention, both the inner screws and outer screws have a nylon locking patch on their threads. A cross-sectional view of the entire outer fan mounting setup is shown in Figure 39.

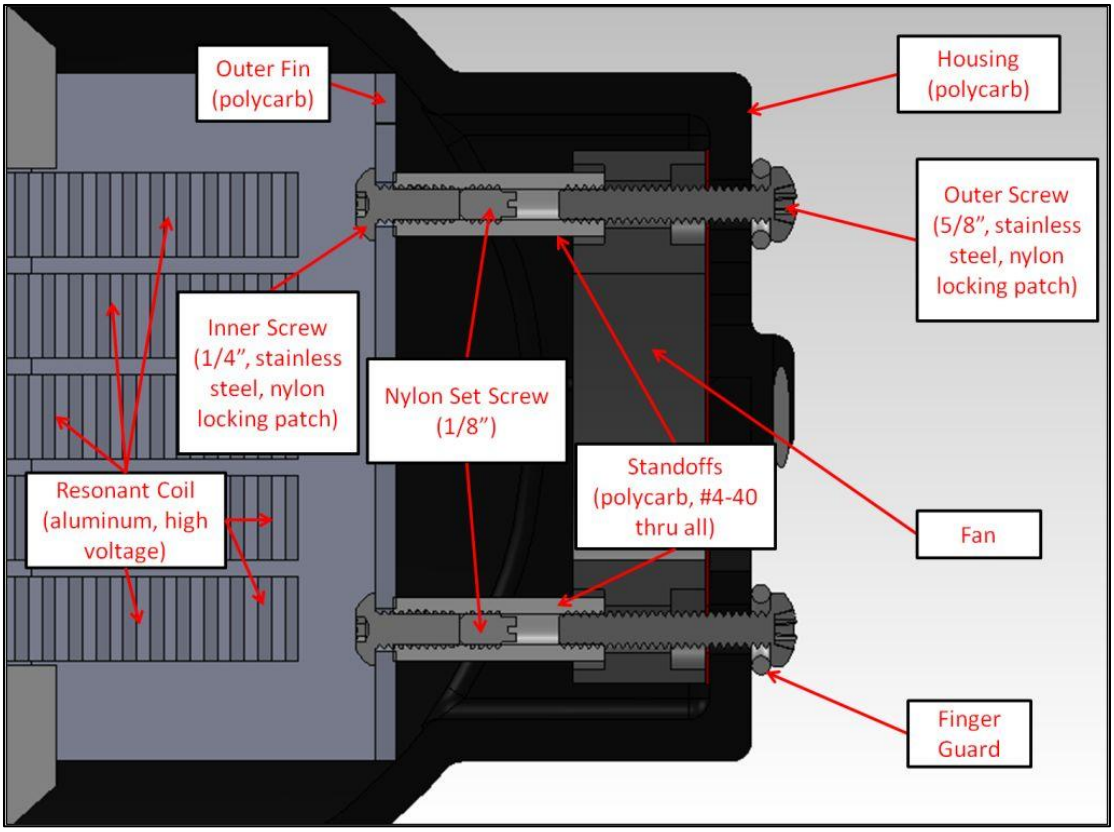

Figure 39 – Cross-Sectional View of Outer Fan Mounting Setup

As mentioned earlier, the inner and outer fins also function as flow guide devices. Both fin types are designed such that their top and bottom surfaces sit flush against the inner face of the housing, forming a seal. This can be seen in Figure 40, which is a cross-sectional view with the cut made through a comb support location. For clarity, the outer and inner fins are shown in black, the inner fin mount in green, the comb supports in yellow, the combs in red, and the resonant coil in blue.

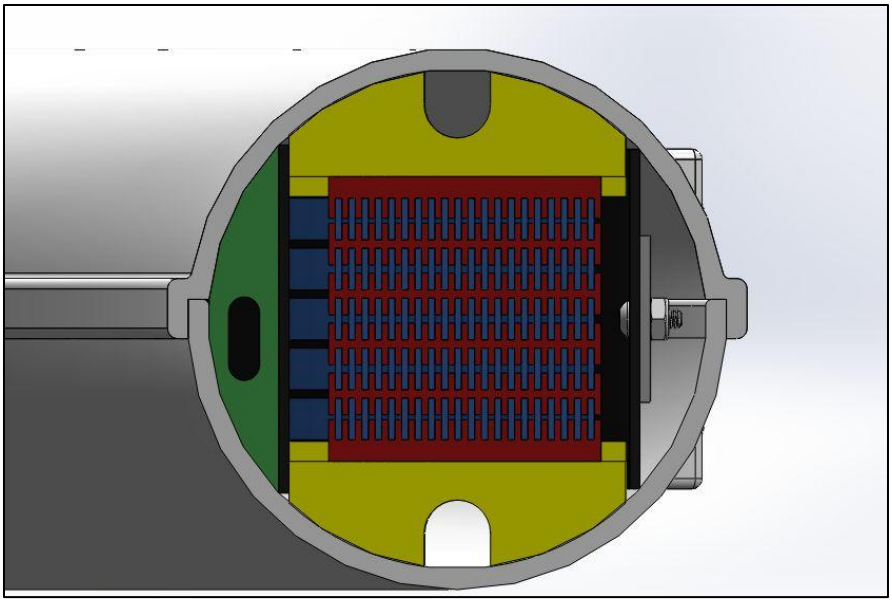

Figure 40 – Comb Support Cross-Sectional View

Because the top and bottom edges of the fins sit flush against the inner wall of the housing, a "cooling channel" is formed around the resonant coil. An added benefit of this setup is that wiring which runs from the powerbox to components located at a distance from it, such as the IR boards and outer fans, can be routed in the two cavities formed on either side of the channel. This setup ensures that this wiring is safely isolated from the high voltage, high temperature resonant coil.

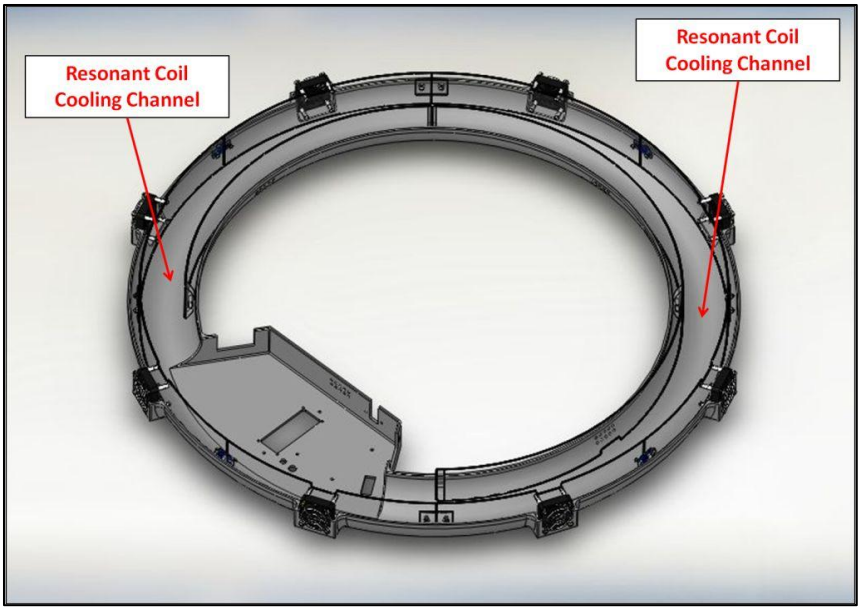

Figure 41 – Resonant Coil Cooling Channel

All inner and outer fins have a notch cut into their center to allow cooling air to pass through. As can be seen in Figure 33 and Figure 35, the inner fin notch is placed at the bottom of the fin, and the outer fin notch is placed at the top of the fin. Based on the locations of the outer fin notches, the cooling air is forced to pass up and over the top of the outer fins, so that it contacts the top layer of the resonant coil first. Similarly, to exit the housing the cooling air must pass through the bottom notch locations of the inner fins, below the bottom layer of the resonant coil. Figure 42 shows the fin notch locations in more detail. This notch design forces the cooling air to pass through all five layers of the resonant coil, enhancing thermal performance. Without the notches, the majority of the airflow would most likely travel completely over or under the resonant coil, without much flow penetration into the core of the windings.

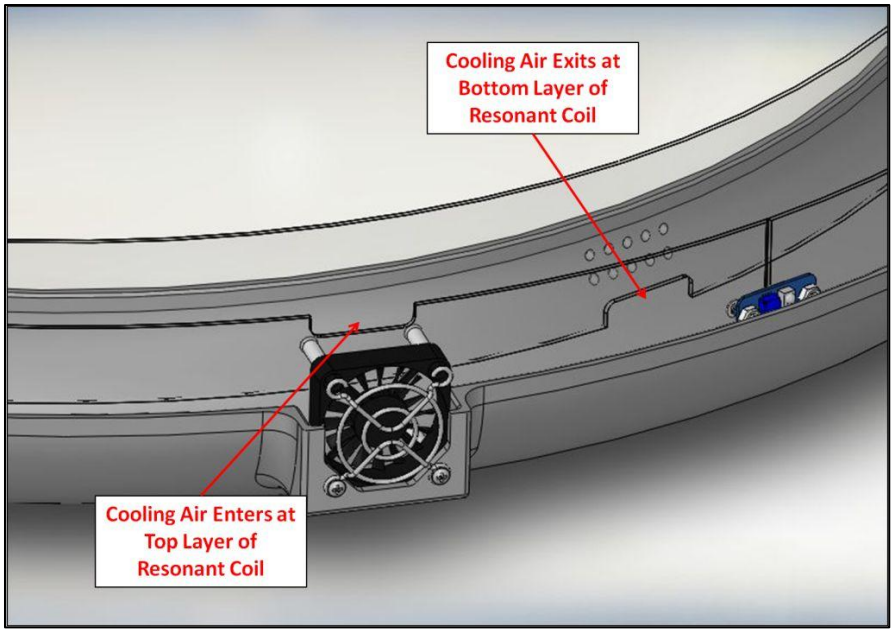

Figure 42 – Outer and Inner Fin Notch Locations

3.2.3: Powerbox Fans

In addition to the eight outer housing fans, two fans are located on the oblique walls of the powerbox area of the housing. The powerbox fans are enclosed in a polycarbonate part called a "fan box." An image of a fan box is shown in Figure 43. Two mounting grooves are located on the top and bottom edges of the fan box to allow it to be mounted in the housing walls.

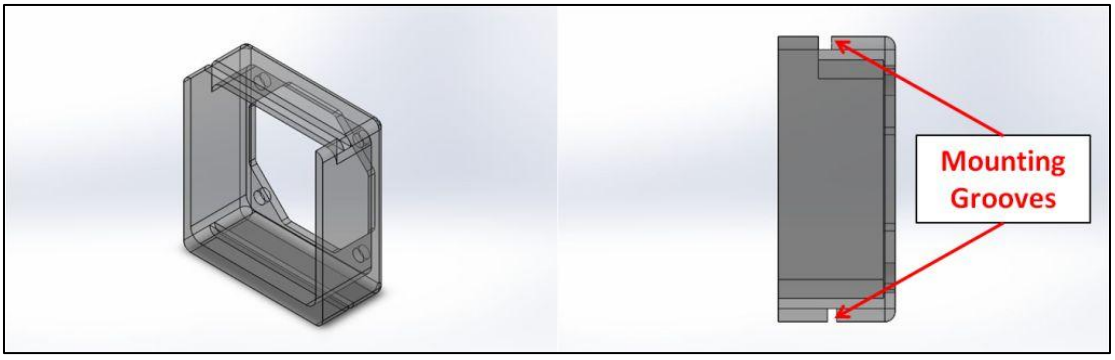

Figure 43 – Fan Box

Four #4-40 screws and four nylon insert nuts are used to secure the fan inside the fan box. These screws also secure the fan guard to the outside of fan box. To prevent line of sight access through the fan inlet and into the powerbox, a "fan box plug," also made from polycarbonate, is adhered to the inner face of the fan box using Permabond 820. Similar to the outer fins, the fan box plug forces the cooling air to flow upwards and exit the fan box near the top of the powerbox. The fan box assembly is shown in Figure 44.

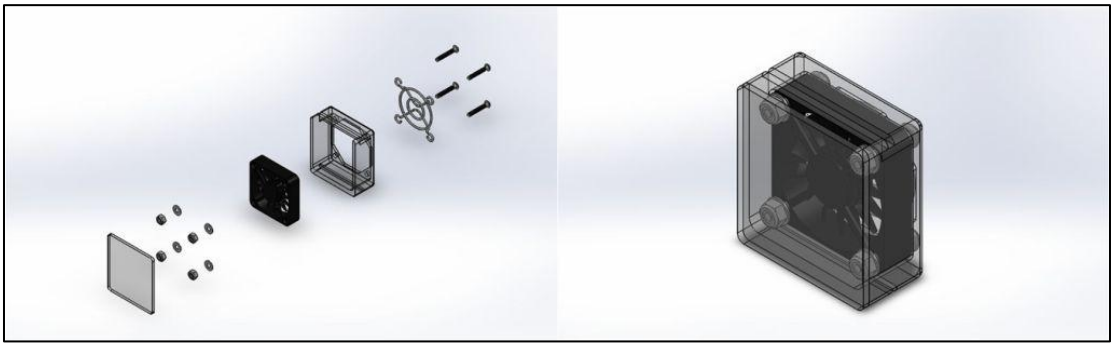

Figure 44 – Fan Box Assembly

As mentioned earlier, two mounting grooves on the top and bottom faces of the fan box facilitate their mounting into the housing wall. This setup is shown in Figure 45. First, the fan boxes are placed into the housing bottom with the housing wall occupying the bottom groove of the fan box. Then, as the housing top is installed, its wall slides into place in the top groove of the fan box, which securely traps the fan box in place.

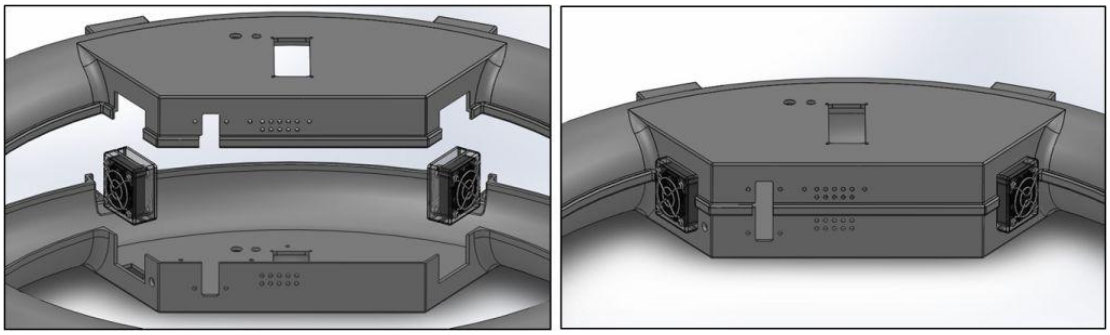

Figure 45 – Fan Box Mounting

. While access into the housing through the three exit air diffusers on the curved surfaces of the housing is blocked by the three inner fins, the diffuser on the powerbox is blocked by a separate component. Made from polycarbonate, the "diffuser safety cap" is shown in Figure 46. Two flanges on either side of the diffuser safety cap contain screw holes which allow it to be mounted to the housing top.

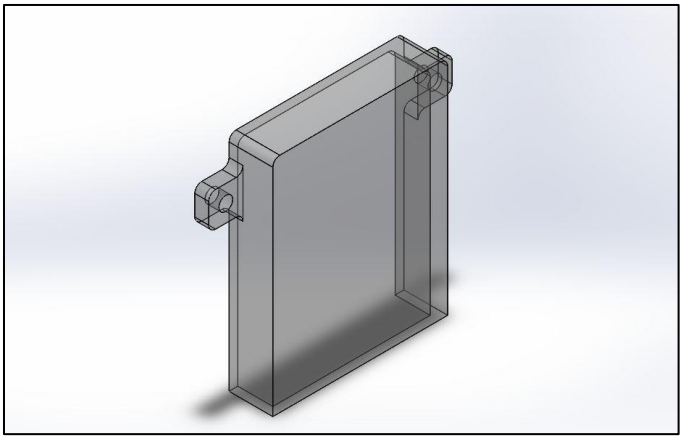

Figure 46 – Diffuser Safety Cap

The diffuser safety cap is mounted to the housing top using two #4-40 screws with nylon insert nuts. Once the housing top is installed, it properly blocks access into the powerbox through the exit air diffuser. This setup is shown in cross-sectional views in Figure 47. Only the bottom face of the safety cap is open, so that once it is installed, the cooling air can only exit the diffuser by traveling up into the diffuser

from the bottom of the housing. Since the fan box plugs force the air to enter the powerbox at the top of the housing, cooling performance is enhanced since the air must travel down through the powerbox before exiting, similar to the notch setup in the outer and inner fins.

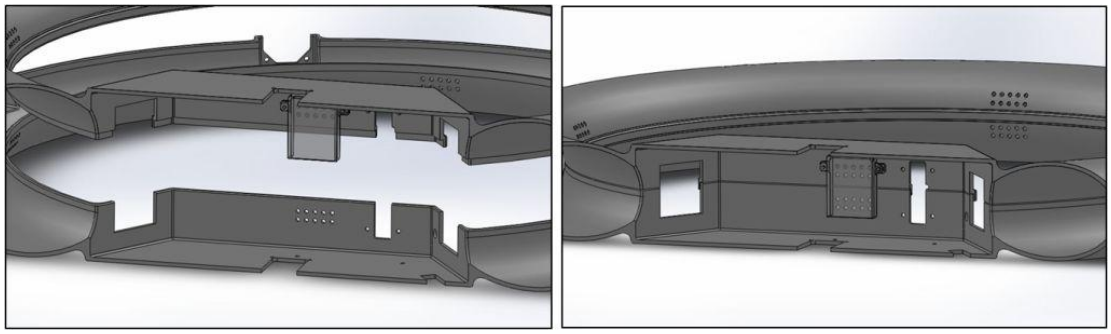

Figure 47 – Diffuser Safety Cap Setup

Chapter 4: Electronics

4.1: Circuit Design

4.1.1: Resonant Coil Drive Circuit

At the heart of the RINGS electronics is the resonant coil drive circuit, which must convert the DC voltage of the batteries into an AC voltage to be applied to the load. A drive architecture based upon a high power operational amplifier (op amp) was considered, but due to the high currents that were needed in the coil, the power dissipated in the op amp would have been unmanageably large. It was estimated that the power dissipated in an op amp would be at least 150 watts, which would have been too much of a thermal burden, in addition to significantly reducing the battery depletion time due to the extra power draw.

Since the op amp was not a viable option, it was decided instead to use an H-Bridge architecture. An H-Bridge uses four metal-oxide-semiconductor field-effect transistors (MOSFETs) in a switching configuration. By rapidly switching these transistors in a controlled manner, an AC voltage having a rectangular waveform can be produced from a DC voltage source. Since the MOSFETs have an extremely low resistance in their "on" state, power dissipation in the H-Bridge is drastically lower than in an op amp. In addition, another benefit of the H-Bridge setup is the ability to precisely control both the frequency and duty cycle of the applied voltage. One drawback of using the H-Bridge architecture is the presence of higher frequency harmonics in the rectangular wave AC voltage. These harmonics slightly increase the power dissipated in the resonant coil; however, the total power dissipated in the drive

circuit and resonant coil is significantly lower with the H-Bridge setup than it would be with an op amp architecture.

It was decided to use a commercial off-the-shelf (COTS) H-Bridge circuit board made by Robot Power. Known as the open source motor controller (OSMC), the board is marketed as a high current motor controller for use in robot combat. The OSMC features many built in safety devices and is designed to avoid the common problems encountered in H-Bridge circuit design. It has a maximum continuous current rating of 160 amps and a maximum source voltage rating of 50 volts, both of which are higher than is necessary for the RINGS drive circuit. A picture of the OSMC is shown in Figure 48.

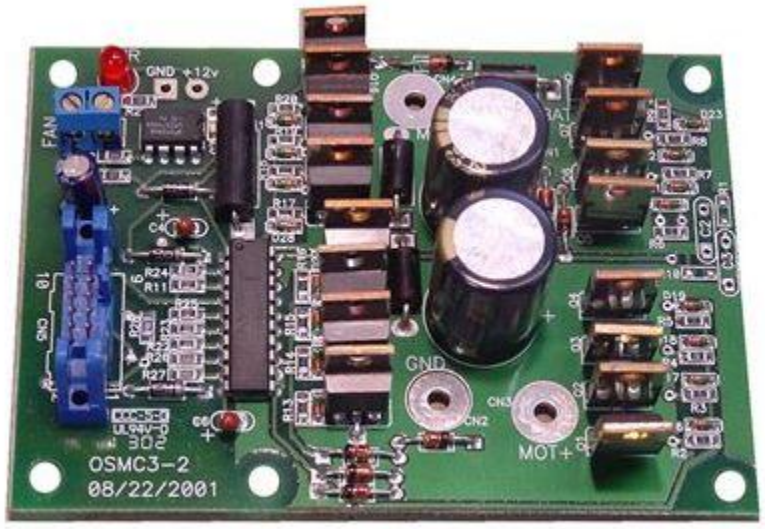

Figure 48 – Open Source Motor Controller (OSMC) made by Robot Power

The resonant coil can be modeled as an inductor and resistor in series. By adding a capacitor in series with the coil, the load becomes a series RLC circuit. Since RINGS operates at two different resonant frequencies (one for EMFF mode and one for WPT mode), two different amounts of capacitance must be added to the coil

depending on the operational mode selected. Additionally, a load resistor must be connected in series with the coil in WPT Receive mode. To achieve this three mode operational capability, the drive circuit was designed as is shown in Figure 49.

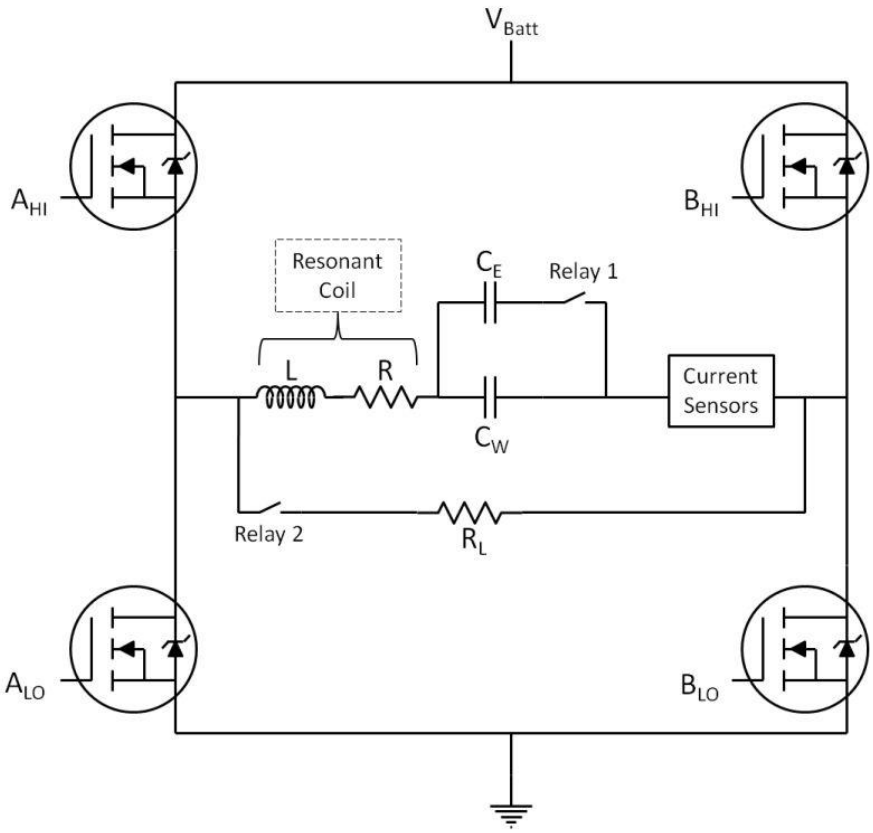

Figure 49 – RINGS Drive Circuit Schematic

In Figure 49, the four MOSFETs of the H-Bridge are labeled as A_{HI}, A_{LO}, B_{HI}, and B_{LO}. The resonant coil is represented by L and R, and C_E and C_W are the capacitors utilized in EMFF and WPT modes, respectively. The load resistor necessary for WPT Receive mode is shown as R_L. Finally, two relays are included as well as a group of three current sensors. By toggling the two relays, three different operational modes can be achieved, as summarized in Table 2. The last column in Table 2 shows the actual resonant frequencies of the completed RINGS units. All

four RINGS units which have been built are extremely well matched and exhibit less than 1 Hz (which is the maximum resolution of the commanded frequency) of resonant frequency difference for both EMFF and WPT Transmit operational modes.

Table 2 – Drive Circuit Operational Modes

Operational Mode	Relay 1	Relay 2	RLC Capacitance	Resonant Frequency (Hz)
WPT Transmit	Open	Open	C_W (10 μF)	462
WPT Receive	Open	Closed	C_W (10 μF)	462
EMFF	Closed	Open	$C_W + C_E$ (310 μF)	83

In EMFF and WPT Transmit modes, the H-Bridge MOSFETs are actively switched to apply the AC voltage to the load. In WPT Receive mode, the H-Bridge MOSFETs are disabled and a 2 ohm load resistor with a maximum power rating of 70 watts is connected in series with the resonant coil. The rationale for setting the load resistor value at 2 ohms is discussed in Section 5.1.2, and the choice of 462 Hz for the WPT operating frequency is discussed in Section 5.1.1.

Because the proximity effect causes increased resistance and hence higher power dissipation at higher frequencies, it was sought to make the EMFF operational frequency as low as possible. Due to the high currents involved, it was necessary to use capacitors made from metallized polypropylene, a dielectric with a low loss tangent, to prevent the capacitors from overheating. Capacitors made of these high quality film dielectrics are, unfortunately, quite a bit larger than other capacitor chemistries. As a result, the EMFF capacitor selection was ultimately governed by available space within the powerbox. The best available option was to use two 150 μF capacitors in parallel for the EMFF capacitance. In EMFF mode, these two capacitors are connected in parallel with the 10 μF WPT capacitor via Relay 1 as

shown in Figure 49. The total of 310 µF utilized in EMFF mode sets the resonant frequency of the RLC circuit to approximately 83 Hz.

In addition to safely handling the large currents, the resonant circuit capacitors must also be able to withstand the large voltages associated with a resonant circuit. At resonance, the energy in the circuit oscillates back and forth between the inductor and the capacitor. This allows us to write an energy balance equation for the inductor and capacitor as

$$\frac{1}{2}LI^2 = \frac{1}{2}CV^2 \tag{17}$$

where L is the inductance of the coil, I is the peak value of the current through the coil, C is the added capacitance, and V is the peak voltage seen across the capacitor. In EMFF mode, the values are: L = 11.9 mH, I = 18 amps RMS = 25.5 amps peak, and C = 310 µF. This results in a maximum AC voltage across the EMFF capacitors of 158 volts peak. To provide margin, the selected EMFF capacitors have a voltage rating of 600 volts peak. The currents generated in WPT Transmit mode are lower than 18 amps RMS, due to the higher resistance of the coil at the WPT frequency, as well as the need to stay safely beneath the power dissipation limits of the WPT capacitor. The onboard microcontroller, discussed in more detail in Section 4.1.2, monitors the current while in WPT transmit mode to ensure that a current limit of 15 amps RMS is not exceeded. The WPT mode parameters are therefore L=11.9 mH, I = 15 amps RMS = 21.2 amps peak, and C = 10 µF. This results in a maximum AC voltage across the WPT capacitor of 732 volts peak. To provide margin, the selected WPT capacitor has a voltage rating of 1300 volts peak.

At the EMFF operational frequency of 83 Hz, the results from the experimental characterization of the proximity effect indicated a coil resistance of approximately 1.1 ohms. Since the DeWalt batteries present a voltage as low as 15 volts when they are near depletion, connecting them in parallel would not allow for achieving the goal current of 18 amps RMS in the resonant coil. Accordingly, the decision was made to connect the batteries in series so that even when they are nearly depleted, 18 amps RMS can still be achieved.

Relay selection was governed by the maximum current and voltage that the relays have to withstand. In EMFF mode, Relay 1 must be able to carry 18 amps RMS. As previously stated, the maximum voltage that the WPT capacitor will see is approximately 732 volts peak. Since Relay 1 is open when in WPT transmit mode, all 732 volts are dropped across the open relay contacts. The K41A734 relay was selected, a single pole single throw normally open (SPST-NO) model manufactured by TE Connectivity. It features a maximum current rating of 30 amps DC and a maximum contact voltage rating of 5 kilovolts, both of which are well in excess of the RINGS design parameters. For simplicity, the same relay was used for both Relay 1 and Relay 2, even though Relay 2 did not require quite as high of a current and voltage rating.

4.1.2: Low Power Board

With the resonant coil drive circuit design finalized, the next step was the design of the "low power board." The low power board contains a PIC microcontroller, various voltage regulators to supply power to sensors, integrated circuits (ICs) and other components, several op amps used for signal conditioning, a

pair of battery protection diodes, the low battery detection circuit, and a set of logic gates. Off-board components that connect directly to the low power board include two liquid-crystal displays (LCDs), a pair of low battery indicator light-emitting diodes (LEDs), a single "master clear" pushbutton used for resetting the PIC, two pushbuttons used for toggling the display mode of the LCDs, and two temperature sensors.

The microcontroller selected for RINGS is part number PIC32MX340F512H, manufactured by Microchip. Among its many features are several analog and digital inputs, multiple digital outputs, an 80 MHz primary oscillator, and a universal asynchronous receiver/transmitter (UART) port, all based around a 32-bit core processor. The analog inputs are used to read in data from three Hall Effect current sensors, a pair of RMS-to-DC converter ICs, and two temperature sensors. Signals read in via the digital inputs include the IR sensor trigger, the low battery signal, the LCD pushbutton signal, and the PIC master clear pushbutton signal. In addition, the Hall Effect current sensors have a "fault" pin that transitions from 5 volts to ground in the event of an "overcurrent" scenario (more information on the overcurrent fault can be found in Section 4.1.3). These three fault signals, as well as the result from a logic gate voting scheme, are read into the PIC via its digital inputs. The digital outputs are used to send control signals to the OSMC which set the duty cycle and frequency of the voltage applied to the resonant coil circuit, relay state command signals to set the proper operational mode, and signals used for commanding the two LCDs. Three additional digital out pins connect to "fault enable" inputs on the Hall Effect current sensors, which are used to activate or deactivate their fault sensing capability. The

UART port allows for communications with the SPHERES satellite. Through this port, RINGS periodically sends test data such as the current waveform in the resonant coil and the temperature of the exiting air and the coil. The primary data sent from SPHERES to RINGS is the desired magnitude and phase of the coil current, which the PIC then translates into an appropriate duty cycle and phase angle to achieve the desired current.

The low power board contains a total of five voltage regulators. Two of these regulators provide a 12 volt output which is used for powering the ten cooling fans and for actuating the two relays. Because of the noise produced by the fans, the outer housing fans are only turned on when the drive circuit is operating and current is circulating in the coil. The two powerbox fans, however, are always turned on when the RINGS power switch is in the on position. To achieve this outer housing fan toggling capability, the first 12 volt regulator is used solely to power those eight fans, and features an on/off signal input which is commanded by a PIC digital output. The second 12 volt regulator is connected to the two powerbox fans and is also used to actuate the relays when the relay circuits are commanded by the PIC digital outputs. Since the current required for powering the fans and relays is higher than that required for the rest of the components, the two 12 volt regulators have a switching architecture to reduce power dissipation. The other three voltage regulators, however, are linear regulators. The first of these three regulators supplies the necessary 3.3 volts to the PIC. The other two voltage regulators have a 5 volt output, which is used for powering various logic gates, op amps, and sensors, as well as the two LCD backlights.

Also contained on the low power board are five op amps that are used for signal conditioning. The first three of these op amps modify the output from the three Hall Effect current sensors. The output from the current sensors is an AC voltage signal proportional to the AC coil current, with a DC offset of 2.5 volts. Since the analog inputs on the PIC only have a range of 0-3.3 volts, it was desired to reduce the DC offset in the current sensor signal from 2.5 volts to 1.65 volts so that it was centered within the read-in range. This offset shift is achieved using an LT1077 op amp with the layout shown in Figure 50. In Figure 50, VHE1 is the output signal from the first Hall Effect current sensor, and HE1 is the properly shifted signal read into one of the PIC's analog inputs. In addition to the DC offset shifting op amps, two additional LT1077 op amps are used to condition the signal from two RMS-to-DC converters. These converters, part number LTC1968, convert the AC output from two of the Hall Effect sensors into a DC value equal to the RMS value of the signal. To reduce the error in the output of the converters, as well as to improve their settling time, the op amp schematic shown in Figure 51 was used. In Figure 51, VRMS1 is the output signal from the first LTC1968 chip, and HE1 RMS is the conditioned signal which is read into an analog input on the PIC. This setup is a basic second order post filter, the design of which is outlined in the data sheet for the LTC1968. In addition, all five of these op amps act as current buffers. Since they are capable of supplying higher levels of current than the sensors themselves, the sampling capacitor in the analog-to-digital converter of the PIC can be charged more rapidly, resulting in a faster sample acquisition time.

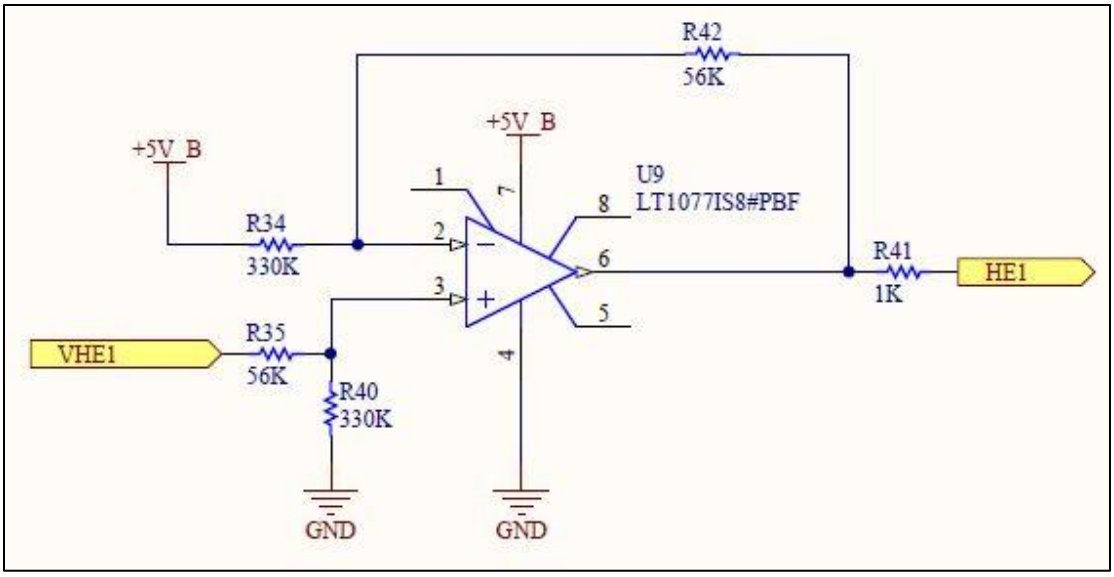

Figure 50 – Op Amp for Shifting DC Offset of Hall Effect Sensor Output

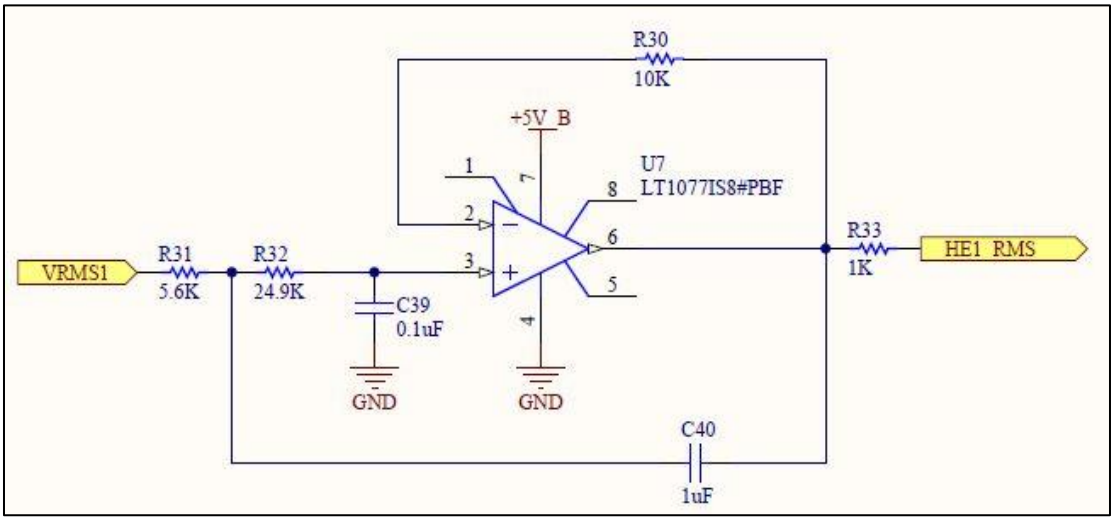

Figure 51 – Op Amp for Improving Performance of RMS-to-DC Converter

NASA safety requirements dictated the need for a pair of battery protection diodes, connected in series, immediately downstream of the batteries. The purpose of these diodes is to prevent any stored energy in the resonant coil circuit from traveling upstream and charging the batteries. Since these diodes must be able to safely handle the full 18 amps of coil current, plus approximately 1 amp to supply the voltage regulators, a diode was sought with the lowest possible voltage drop in order to

reduce its dissipated power. Part number SBR30U30CT, manufactured by Diodes Incorporated, was selected. This diode is rated to 30 amps and exhibits a forward voltage drop of approximately 0.5 volts. Therefore, the power dissipated in each diode at the maximum draw current of 19 amps is, at most, 9.5 watts. During typical operations, however, the dissipated power is lower since a duty cycle of approximately 60% produces the full 18 amps in the coil, depending on the charge level of the batteries. In this case, the dissipated power is closer to 0.6 × 19, or 5.7 watts. The SBR30U30CT comes in a TO-220 package, to which a small heat sink was added for improved cooling.

To alert the software and the operators of a low battery state, a circuit was designed around the LTC1540 comparator, made by Linear Technology. The two inputs to the comparator circuit are the battery voltage and a 1.182 volt reference which is supplied by the comparator itself. By passing the raw battery voltage through a properly sized voltage divider, the comparator's output transitions from 5 volts to ground in the event that the battery voltage dips below 30 volts. The trip point of 30 volts (15 volts per battery) was selected because just before depletion, the batteries present approximately 14 volts. When the coil is being driven at high current levels, however, the battery voltage drops with each driving pulse due to internal resistance in the batteries, and then recovers to a higher value after each driving pulse. This presented a problem for the low battery circuit wherein the output of the comparator would switch rapidly from high to low at the driving frequency when the batteries were nearing depletion. To remedy this, the comparator output is fed into a set-reset (SR) latch IC. At the first instance of the comparator output

transitioning from high to low, the SR chip output latches in a low state. The output from the SR latch is treated as the low battery signal line, which is connected to a digital input on the PIC to alert the software that a low battery state has occurred. Additionally, the low battery signal line is connected to the gate of a P-channel MOSFET which, when activated, causes the low battery indicator LEDs to illuminate.

As mentioned earlier, the three Hall Effect current sensors have a built-in feature in which a fault pin on the chip is pulled from 5 volts to ground in the event that the current reading exceeds a user-set threshold. These three fault lines are each directly connected to a digital input on the PIC. In addition, the fault feature of the sensors can be enabled or disabled via their fault enable pins, which are connected to digital outputs on the PIC. This design provides the capability to deactivate the fault detection capability of a sensor in the unlikely event of sensor failure. For added redundancy, the three fault lines from the current sensors are also fed into a logic gate voting scheme. Shown in Figure 52, the output of this circuit is a logic low in the event that at least 2 out of any of the 3 fault signal inputs are low, corresponding to an overcurrent condition. The overcurrent signal from the voting scheme is connected to a digital input on the PIC, as well as directly to one input on a pair of OR logic gates which carry signals from the PIC to the OSMC to activate the lower MOSFETs of the H-Bridge. By connecting the overcurrent signal directly to the drive circuit logic gates in this manner, the voting scheme provides a hardware shutdown of the system that will occur even if the PIC fails to act.

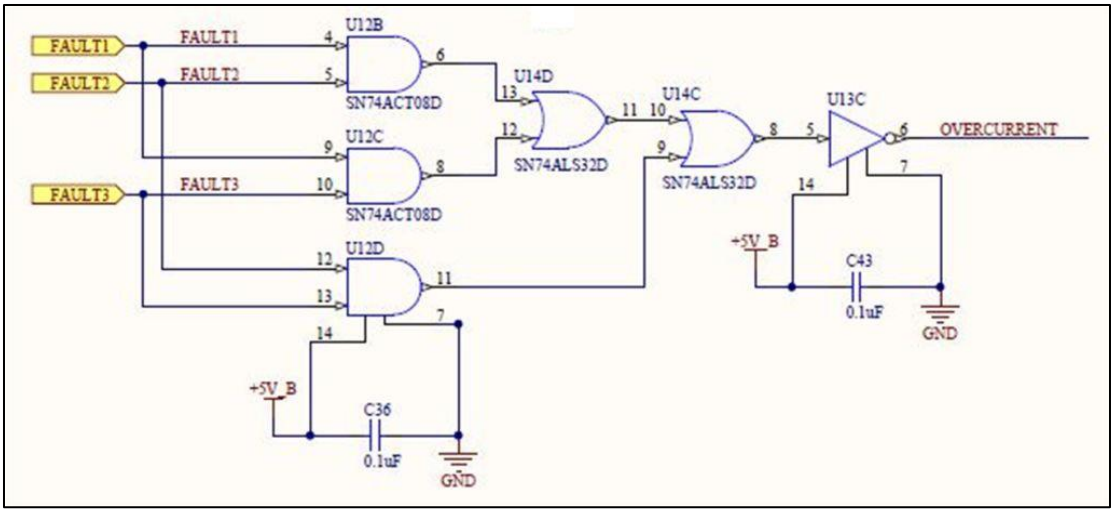

Figure 52 – Overcurrent Voting Scheme

4.1.3: Capacitor Board

In addition to the OSMC and low power board, a third board called the "capacitor board" was designed to contain or directly connect to the majority of the high current carrying components. This includes all of the resonant coil circuit components shown in Figure 49 (except for the MOSFETs, which are located on the OSMC), as well as the Hall Effect current sensors, RMS-to-DC converters, relay activation circuits, and capacitor bleed resistors.

To measure the coil current, the ACS709LLFTR-20BB-T Hall Effect current sensor, made by Allegro Microsystems, was selected. This sensor is designed to be placed in series with the current carrying path of the circuit. It features a conductor resistance of just 1.1 mΩ, which is an order of magnitude lower than the resistance of the coil itself, meaning that the presence of the current sensors has a negligible impact on the circuit behavior. The sensor gain is 56 mV/A, with a maximum sensing range of -37.5 to 37.5 amps, which are both well suited for the expected maximum current

level of 18 amps RMS. For redundancy, three of these sensors were placed in series in the resonant coil circuit.

A chief benefit of the ACS709 sensor is a built-in "overcurrent fault" feature. This feature allows an overcurrent fault value to be set via a voltage divider. When the measured current exceeds this value, the "fault" pin of the sensor transitions from 5 volts to ground and latches low. For operations on the ISS, RINGS received a waiver from NASA which allows the generation of a magnetomotive force (MMF) up to 2100 amp-turns RMS. Since each coil is made of 100 turns, this meant that the coil current could not exceed 21 amps RMS. The error in the overcurrent fault switchpoint is listed in the ACS709 datasheet as +/- 1 amp. With this in mind, the overcurrent fault level was set to 19.5 amps RMS, or 27.6 amps peak, which is halfway between the maximum goal current of 18 amps RMS and the maximum allowable current of 21 amps RMS. Additionally, the overcurrent detection feature can be enabled or disabled via a "fault enable" pin, each of which is connected to digital outputs on the PIC. This setup allows the software to disable the fault detection capability of the three sensors in the event of sensor failure.

In addition to the current sensors, the capacitor board contains a pair of LTC1968 chips, made by Linear Technology. The LTC1968 is an RMS-to-DC converter, which outputs a DC voltage equal to the RMS value of the AC voltage applied to its input. These converters were included to provide additional redundancy against an overcurrent scenario. Their outputs are connected to analog inputs on the PIC, and the software continuously monitors their values so that the system can be safely shut down should an overcurrent event occur. The input of each LTC1968

sensor is connected to the output of a single Hall Effect current sensor. The reason that only two, instead of three, RMS-to-DC converters were included was a lack of available analog inputs on the PIC. As outlined in the LTC1968 datasheet, the converter output has an associated settling time and peak error based on the frequency of the input signal and the value selected for the averaging capacitor, C_{AVG}. The value of C_{AVG} was chosen to be 2.2 µF. With the inclusion of the buffered post filter shown in Figure 51, the peak output error of the LTC1968 is less than 0.2% at EMFF frequency and is even smaller at WPT frequency. For settling time, this setup results in a settling accuracy of 1% after approximately 150 msec.

Also included on the capacitor board are the two relay activation circuits. The K41A734 relays have a nominal pick-up voltage of 12 volts and a coil resistance of 70 Ω. This resulted in a power dissipation level in the relay of just over 2 watts, which was higher than was desired. To reduce power dissipation in the relays, a "spike and hold" circuit is used. Built around a 555 timer, this circuit, when activated by a signal from a PIC digital output, applies a full 12 volts to the relay for approximately 20 msec. This ensures that the relay is fully activated, since its datasheet lists an activation time of 10 msec. After the 20 msec period, the applied voltage is reduced to 5 volts. Electrical testing indicated that a holding voltage of 5 volts was more than adequate, as the relays never disengaged at a voltage above 3 volts. With the holding voltage set at 5 volts, the power dissipation in the relays is reduced to only 0.36 watts.

The last major components included on the capacitor board are two "bleed" resistors. In a nominal shutdown, both low MOSFETs of the H-Bridge are activated,

allowing the coil current to ring down naturally. However, in the event of an improper shutdown it is possible that the EMFF and/or WPT capacitors will remain charged. If this happens, the inclusion of the two bleed resistors ensures that these capacitors will be safely discharged. The EMFF bleed resistor is connected in parallel with the EMFF capacitors, and has a value of 47 kΩ, resulting in an RC time constant of approximately 14 seconds. A second bleed resistor, also 47 kΩ, is connected from one terminal of the WPT capacitor to ground, resulting in an RC time constant of approximately half a second. The 47 kΩ resistances are orders of magnitude higher than the coil resistance, so the effect of the bleed resistors on circuit behavior is negligible.

4.1.4: IR Sensor Board

To produce the desired inter-vehicle electromagnetic forces and torques used in EMFF operations, it is necessary that the current waveforms in each coil be synchronized with one another. When in phase, the two vehicles will attract towards one another and when out of phase, they will repel from one another. To achieve this synchronization, the RINGS vehicles use the same IR sensor scheme that the SPHERES satellites use for synchronization and metrology. During a test session, one of the SPHERES is designated as the primary or master vehicle, and the other SPHERES as secondary or tertiary vehicles. The master SPHERES satellite emits an infrared pulse at a nominal frequency of 5 Hz, which is detected by the IR sensors on the secondary and tertiary satellites. To detect this pulse, a total of nine IR sensor boards are included in each RINGS vehicle. The boards are located throughout the vehicle to provide the maximum possible field of view for detecting an IR pulse.

The IR sensor used in RINGS is the same chip that SPHERES uses: the TFDU4101 sensor, manufactured by Vishay Semiconductor. The output received pin of this chip is nominally at 5 volts. When an IR pulse is detected, the output received pin transitions from 5 volts to ground for a period of 2 μsec. Also included on each IR sensor board is an AND gate. By daisy-chaining the boards together, this design ensures that an IR pulse detected by any one of the nine sensors is received by the PIC. This daisy-chaining setup is accomplished via a modular design that allows each IR sensor board to be configured in three different styles. By removing or including certain resistors, each board can be set up as either a "root," middle," or "end" style board. The schematic for the RINGS IR sensor board is shown in Figure 53. A root style board connects directly to the low power board via the P3 connector and does not contain R2 or R3. Two upstream boards connect to the root board through connectors P2 and P3. The middle style board connects to a root board through the P3 connector and an end style board through the P2 connector. The P1 connector is left open, R2 is populated, and R3 is not included. An end style board can connect to either a root or middle board through its P3 connector. End style boards do not use the P1 or P2 connectors and have R2 and R3 populated. The nine IR boards are split into two branches with the root board of each branch connecting to the low power board. On the low power board, the signals from the two IR sensor branches are fed into an AND gate, and the output of this AND gate is connected to a digital input on the PIC. More information on the IR sensor board configurations and their locations is discussed in Section 4.2.3.

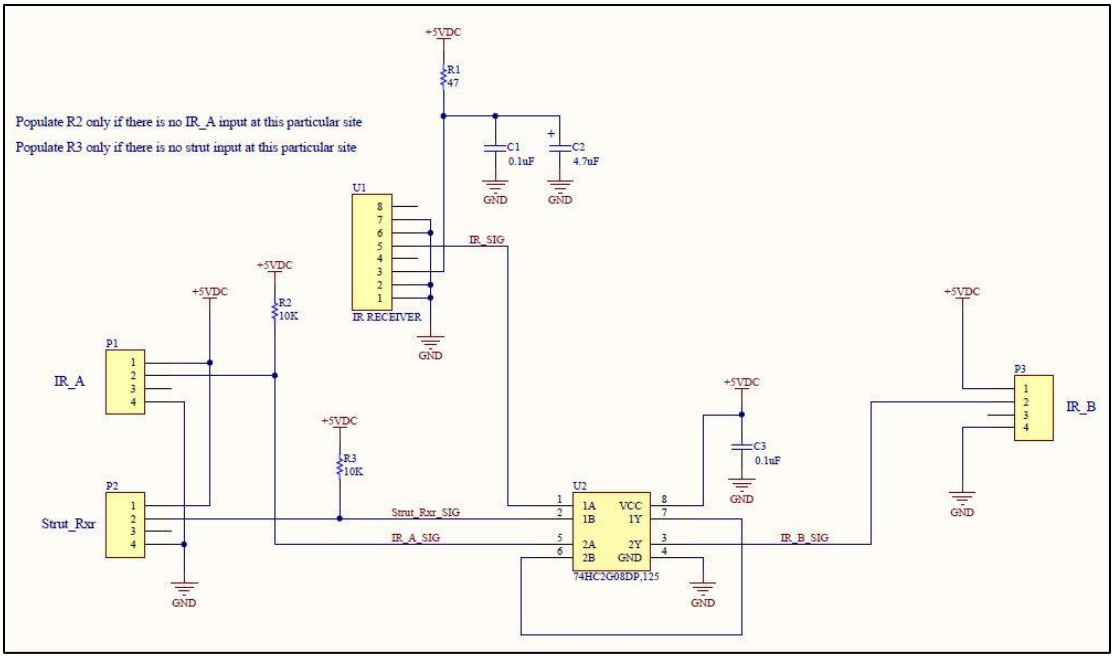

Figure 53 – RINGS IR Sensor Board Schematic

4.1.5: Connector Board

The "connector board" allows for communications between RINGS and SPHERES. It contains a MAX3232 transceiver chip, made by Maxim Integrated. This transceiver is capable of handling data rates up to 250 kilobits per second (kbps) and features enhanced electro-static discharge (ESD) protection. The enhanced ESD protection made it an appealing choice for RINGS, since this feature ensures that RINGS electronics cannot cause damage to SPHERES through the expansion port. Also included on the connector board is a 1 MΩ resistor placed between the SPHERES ground and the RINGS ground. This resistor ensures that RINGS and SPHERES share a common ground, as is necessary for communications, but its large value guarantees that no significant amount of current can be transferred between them.

4.1.6: Temperature Sensor Board

The last of the circuit boards included in the RINGS vehicles are the two "temperature sensor boards." The sensor selected was part number TC1047A, manufactured by Microchip. Specifically designed by Microchip to interface with the PIC, this sensor has an output whose voltage varies linearly with the temperature of the sensor itself. With a temperature sensing range of -40°C to +125°C, the TC1047A is well suited to the needs of the RINGS system. Since the circuit only requires a single surface mount capacitor in addition to the sensor chip, the temperature sensor boards were constructed using electrical prototype boards, also known as "surfboards." One temperature sensor board is attached directly to the face of the resonant coil, in an area about 10" away from the powerbox, as shown in Figure 54. This board is adhered to the coil using a two part adhesive called Arctic Alumina. This compound is thermally conductive but is a pure electrical insulator, allowing the temperature sensor to be directly attached to the high voltage windings of the coil without electrical interference. The second temperature sensor is placed on the inner face of the safety cap which covers the powerbox exit air diffuser to monitor the exit air temperature, as shown in Figure 55. This board is also mounted with Arctic Alumina.

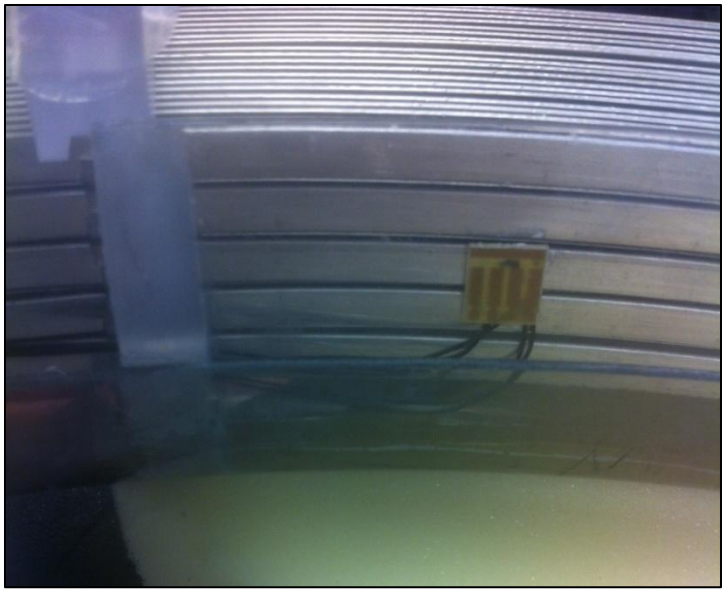

Figure 54 – Resonant Coil Temperature Sensor Board

Figure 55 – Exit Air Temperature Sensor Board

4.1.7: Off-Board Components

The remaining components of the RINGS electronics, known as the "off-board components," include the power switch, LCDs, pushbuttons, and low battery

indicator LEDs. These components are not mounted to any of the circuit boards. Instead, they are located in various cutouts in the powerbox area of the housing.

The power switch serves as the main power cutoff between the RINGS electronics and the DeWalt batteries. It is placed directly between the positive terminal of the "upper" battery and the positive power connection of the low power board. The ground terminal of the upper battery is connected to the positive terminal of the "lower" battery, so that the positive terminal of the upper battery has a nominal voltage of 36 volts. A rocker switch design was chosen due to their wide commercial availability and ease of mounting in the housing wall. The switch selected was CRE22F2FBBNE, manufactured by Cherry Electrical. This unit has a maximum current rating of 20 amps, which is suitable for the maximum battery current draw of 19 amps.

The LCDs selected for the RINGS vehicles were part number AND491GST-LED, made by Purdy Electronics. Two LCDs are included in the RINGS vehicle, each one located on the large flat face of the powerbox, so that they can be viewed from either side. The display includes an onboard LCD controller and drive circuit for easy integration with the PIC. It is capable of displaying 2 lines of 16 characters each, which was deemed adequate for the display needs. Also built into this unit is an LED backlight which makes the display easier to read. By pressing the LCD screen select pushbutton on the housing, the operator can cycle through various display modes. Among the various display modes are operational mode, the number of amp-turns RMS present in the coil, the exit air and resonant coil temperature, and the

amount of power received in the load resistor, if applicable. In the event of a PIC-initiated safety shutdown, the display indicates which violation has occurred.

Three pushbuttons are mounted in the powerbox area of the housing and are wired directly to the low power board. Two of these pushbuttons, located next to the LCD displays, are used to toggle the display mode of the LCDs. The third pushbutton is located on one of the oblique powerbox walls and serves as a master clear button which can be used to reset the PIC software if necessary. Part number 104-0013-EVX, made by Mountain Switch, was selected for all three pushbuttons.

The final off-board components are the two low battery indicator LEDs. These LEDs illuminate to alert the crew of a low battery state. The part selected was 249-7968-3732-504F, made by Dialight. This LED is green in color, which was necessary to meet NASA safety standards, as red, orange, and yellow LEDs are not permitted.

4.2: Printed Circuit Board Sizing and Mounting

With the circuit board schematics finalized and the off-board components selected, the next challenge was to size the boards so that the electronic components could fit into the available powerbox volume. All components had to be located at a safe distance away from the resonant coil, and the entire setup had to be designed to allow complete assembly in the housing bottom, since the installation of the housing top prevented any further access to interior components. A key strategy in achieving a compact layout was the stacking of various components to take full advantage of the available vertical volume.

4.2.1: LCD Displays, Low Power Board, OSMC and Connector Board

The two LCDs are located in the center of the two large faces of the housing top and housing bottom. To prevent the possibility of the LCD screen shattering and presenting a debris hazard, a safety cover was designed. The safety cover is composed of two pieces: a base plate and a lens, each made from polycarbonate. The LCD is attached to the housing using four #2-56 screws with nylon insert nuts, as shown in Figure 56. In addition, four 1/8" long stainless steel spacers are placed between the LCD and the housing wall to allow for clearance of various surface mounted components on the LCD rim.

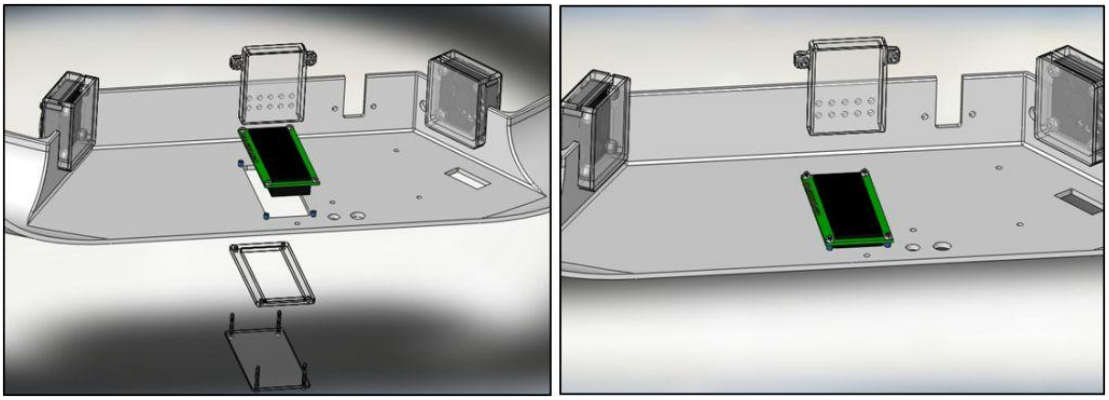

Figure 56 – LCD Mounting Setup with Base Plate and Lens

The low power board was designed to sit overtop of the bottom LCD. This enabled the use of a low profile board-to-board connection between the bottom LCD and the low power board, helping to conserve space in the powerbox. The low power board, shown in green in Figure 57, is mounted to the housing using five #4-40 screws. To provide clearance between the housing bottom and the underside of the low power board, a 7/16" long stainless steel spacer was used with each of the five mounting screws. As can be seen in Figure 57, the OSMC (shown in blue) and low power board are attached to each other using hex standoffs to form a "stack." The

hex standoffs, made from stainless steel, are 1” in length. This provides enough clearance between the underside of the OSMC and the top of the low power board to accommodate the battery protection diodes, which are stood vertical and are the tallest components on the low power board. The two orange cylinders shown in Figure 57 are electrolytic capacitors included on the OSMC for filtering of the raw battery voltage. When mounted, the tops of these capacitors fit just within the 3” of available vertical clearance within the powerbox.

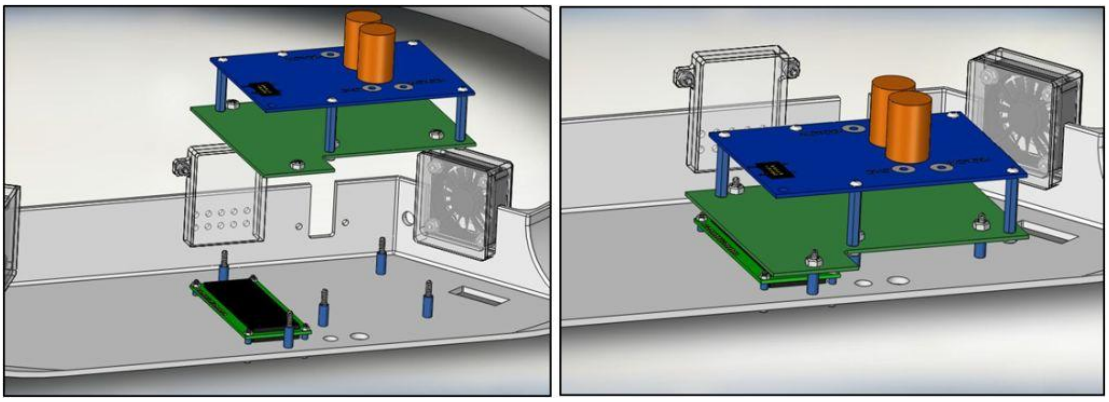

Figure 57 – Low Power Board and OSMC Stack

The connector board is mounted on the long wall of the powerbox, next to the diffuser safety cap, as shown in Figure 58. Its close proximity to the low power board allowed for a clean, non-intrusive cable connection between the two boards. Four #4-40 self-clinching or “PEM” nuts are pressed into the board to provide a screw anchor location. During assembly, the connector board is first installed into the housing bottom using two #4-40 machine screws. After the housing top is installed, the remaining two #4-40 machine screws are installed through the housing top into the two open PEM nuts. The two hex standoffs shown in Figure 58 allow the SPHERES to RINGS ribbon cable to be firmly anchored to the connector board to provide strain relief.

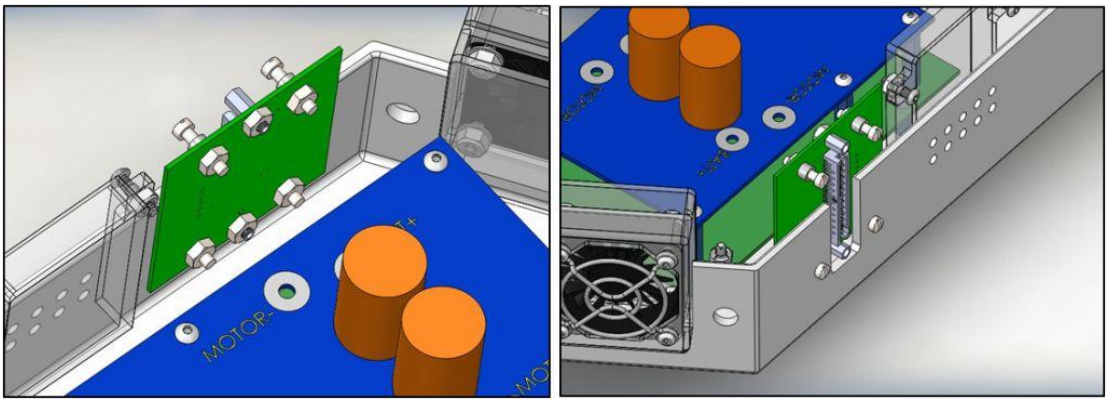

Figure 58 – Connector Board

4.2.2: Capacitor Board and Relays

To mount the relays, a small polycarbonate part known as the "relay mount" was designed. A steel "loop clamp" grabs onto the cylindrical body of each relay, and this loop clamp is then bolted to the relay mount using a #10-24 steel machine screw and corresponding nylon insert nut. The relay mount and the full relay assembly are shown in Figure 59. The relay mount was designed so that the relays, once installed, are horizontally staggered. This choice was made so that the high current carrying contacts of the relay are not aligned when viewed from overhead, allowing for easier installation of vertically oriented wiring.

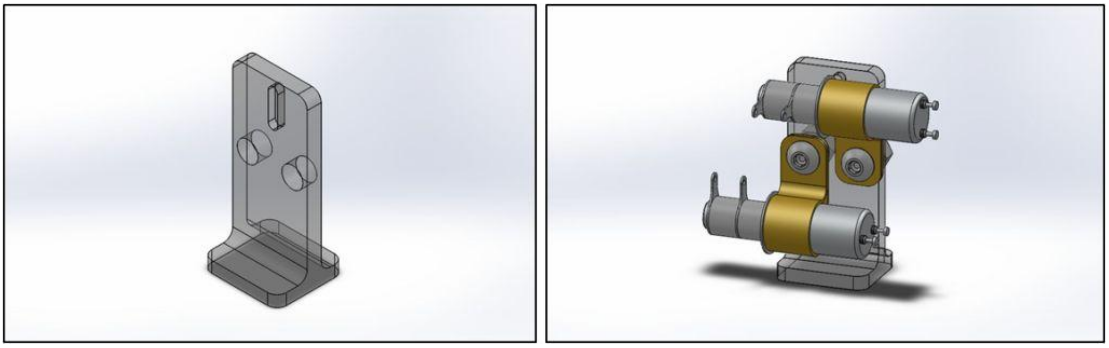

Figure 59 – Relay Mount and Relay Assembly

At this point, the four major remaining components to be fit into the available powerbox volume were the relay mount, WPT capacitor, and the two EMFF capacitors. These components were laid out as shown in Figure 60. In Figure 60, the two larger red boxes are the EMFF capacitors, and the smaller red box is the WPT capacitor. This arrangement provided sufficient space between the three capacitors themselves as well as between the capacitors and the side walls of the housing so as not to impede the cooling airflow. It also resulted in a safe amount of distance between the components and the resonant coil.

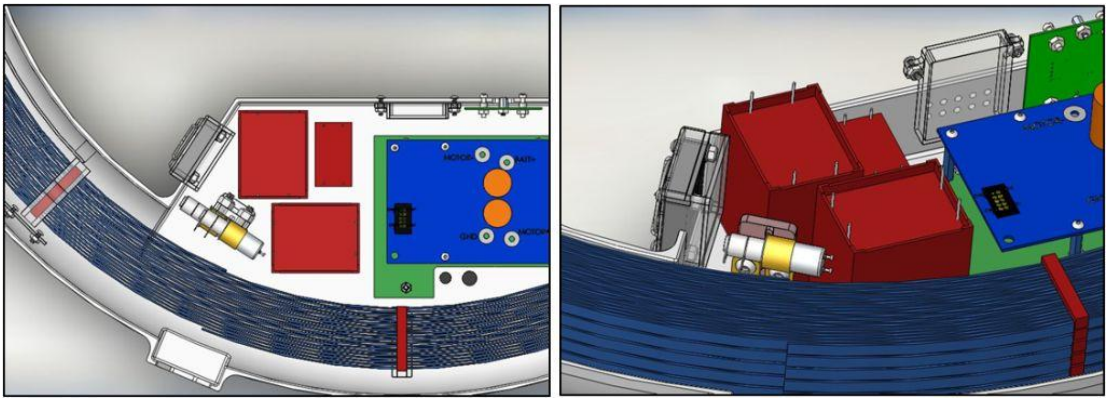

Figure 60 – Capacitor and Relay Mount Setup

The capacitor board was designed to mount directly to the terminals of the two EMFF caps. This placed the bottom surface of the capacitor board slightly above the top of the nearby fan box, as well as slightly above the top layer of the resonant coil. Single wire connections were chosen for the connections from the capacitor board to each of the four WPT capacitor terminals as well as to the two relays. The final size and shape of the capacitor board is shown in Figure 61, with the board shown in transparent yellow for clarity. Various flanges located around the perimeter of the board were included for the placement of cable headers and single wire connection terminals.

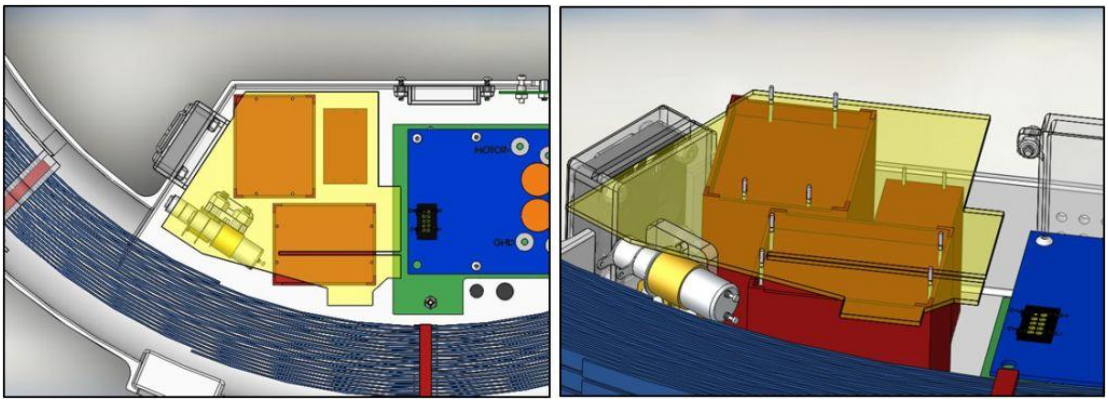

Figure 61 – Capacitor Board Setup

Before installation, the single wire connections to the relays and WPT capacitor are installed in a compact manner. These connections, as with all the high current carrying components, were made using American wire gauge (AWG) size 12 wire. Figure 62 shows a picture of the wire connections to the relays and the WPT capacitor. The heavy gauge of this wire makes it quite stiff, so once the relays and WPT capacitor were connected, the entire capacitor board unit was very rigid. Figure 63 is an overhead photo of the capacitor board assembly which highlights the compact nature of the single wire connections, which was imperative to ensure they did not get too near the resonant coil.

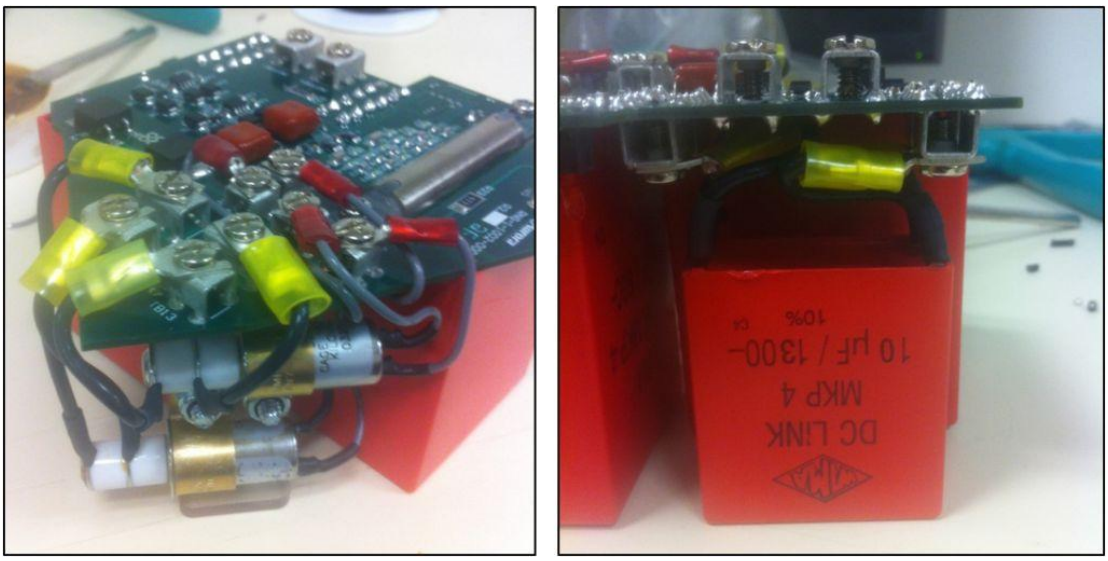

Figure 62 – Wire Connections from Capacitor Board to Relays and WPT Capacitor

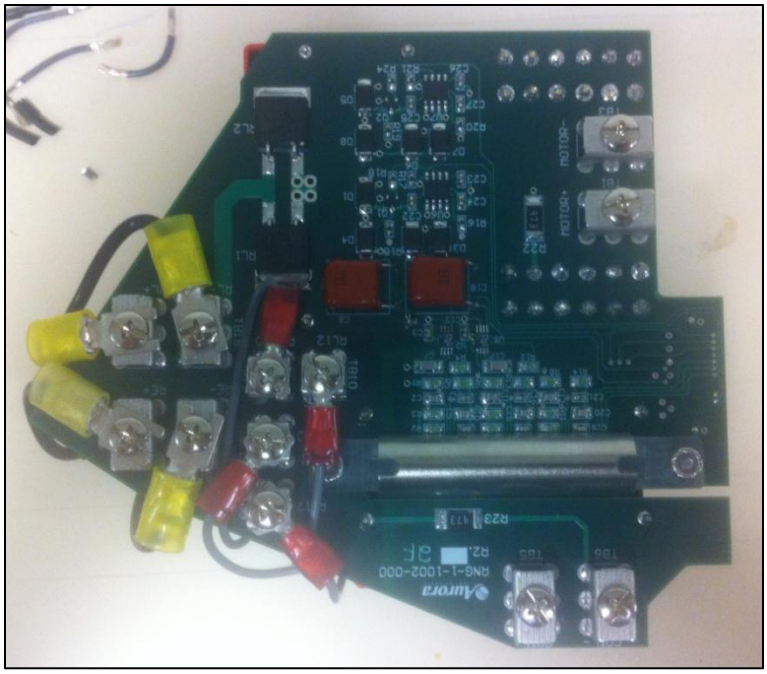

Figure 63 – Overhead View of Capacitor Board with Relays and WPT Capacitor Installed

After the relays and WPT capacitor are wired in to the capacitor board, the entire assembly is placed into the housing bottom and glued in place using

Permabond 820. The adhesive is applied to the bottom surface of the two EMFF capacitors, the bottom surface of the WPT capacitor, and the bottom surface of the relay mount. The large available gluing surface area ensures that the capacitor board assembly stays firmly attached to the housing bottom.

4.2.3: IR Sensor Boards

As discussed earlier, four of the nine IR sensor boards in each RINGS vehicle are located at joints in the outer fin ring. Since there was not much available volume here, the IR sensor board was designed to be as compact as possible. By using small connectors and placing components on both sides of the board, the final dimensions of the IR boards were reduced to 1.15" x 0.49".

In addition to the four boards placed on the outer fin ring, four more IR boards are placed into cavities in the attachment structure struts. As shown in Figure 64, a polycarbonate cover is placed over the face of the board. Two #4-40 machine screws thread into two threaded inserts in the strut and hold the cover and IR board in place. The small groove placed at the bottom edge of the cavity allows for wiring to exit the cavity and be routed into the housing.

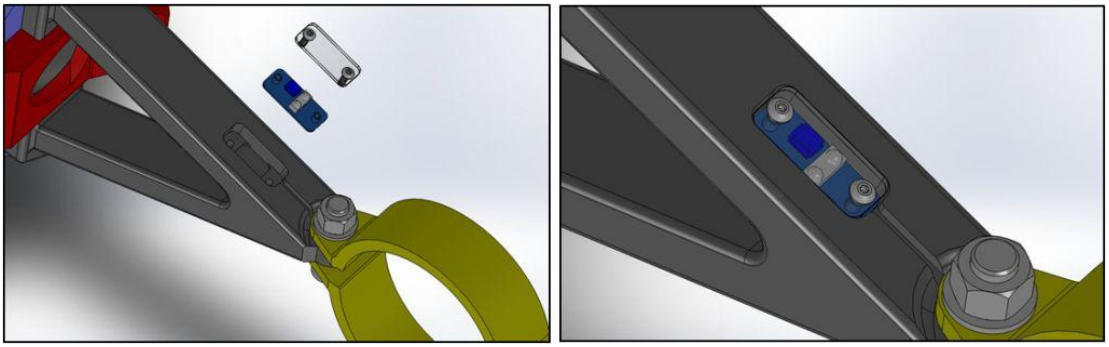

Figure 64 – IR Sensor Board Strut Mounting

The ninth and final board is mounted to one of the inner fins, as shown in Figure 65. This IR sensor board mounts vertically using the same hardware as is used to mount the outer fin joint IR boards. Whereas the other eight IR boards face away from the SPHERES satellite of their own vehicle, the inner fin IR board faces directly towards it. This board was included to guarantee that the IR pulse is detected by the RINGS vehicle, even if it is only emanating from the SPHERES satellite to which that RINGS unit is attached.

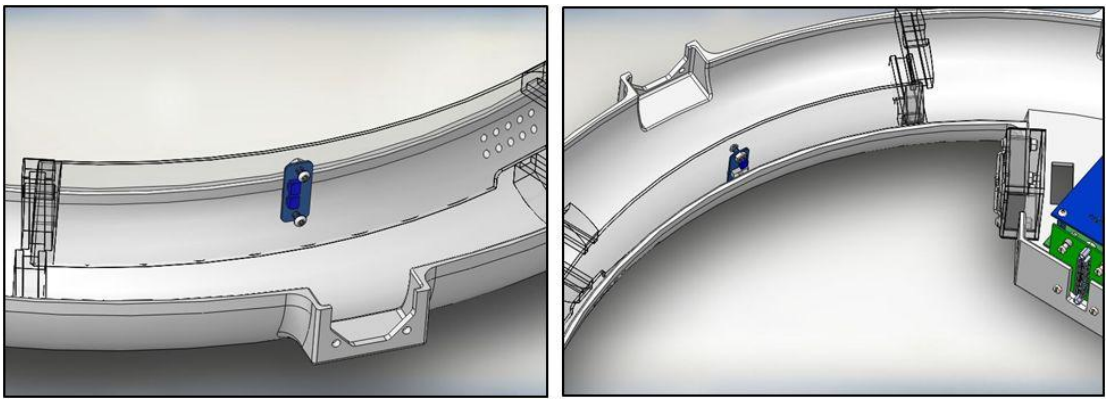

Figure 65 – Inner Fin IR Sensor Board

4.2.4: Pushbuttons and Switches

The rocker switch is mounted into the housing bottom as shown in Figure 66. The switch is a "panel-mount" design and contains four small clip features that lock into the side walls of the housing cutout. Once installed, the clip feature ensures the switch is securely mounted in place. Also visible in Figure 66 is the switch guard, which was included to meet NASA safety requirements. The switch guard is a small nylon piece which is sandwiched between the housing and the rocker switch. Its purpose is to prevent accidental toggling of the power switch during handling.

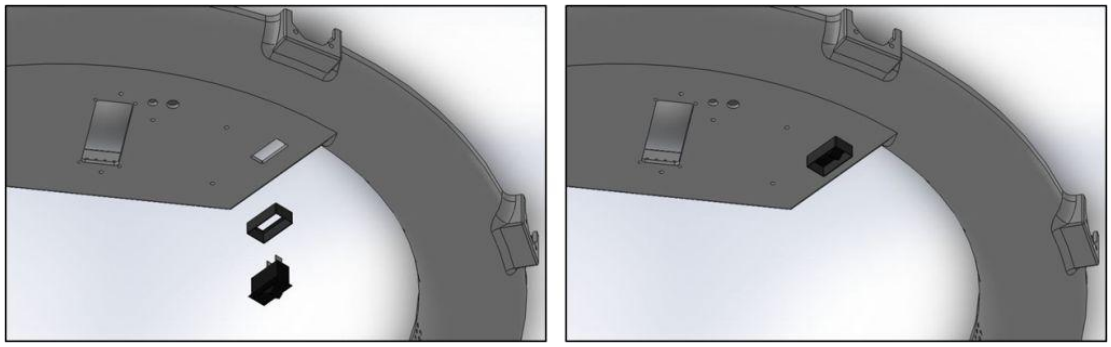

Figure 66 – Rocker Switch and Switch Guard

One LCD screen select pushbutton and one low battery indicator LED are each mounted in the housing bottom as shown in Figure 67. They are placed inside the elbow of the L-shaped cutout in the low power board, allowing for a short wiring connection to the low power board. Both the pushbutton and the LED are mounted using hex nuts and lock washers that are included with the components, which provide back-out prevention. In addition to the pushbutton and LED shown in Figure 67, an additional pushbutton and LED are mounted into a mirrored location in the housing top.

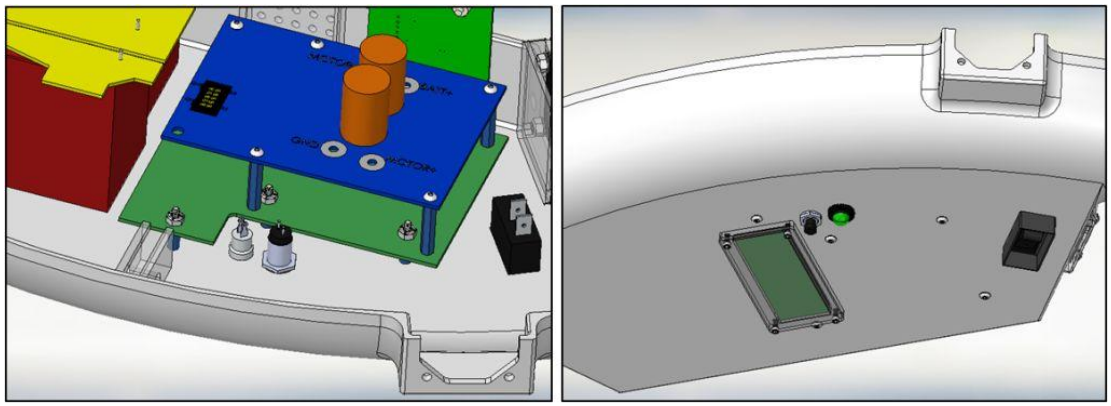

Figure 67 – LCD Pushbutton and Low Battery Indicator LED Locations

The master clear pushbutton is mounted into the housing bottom on the oblique powerbox wall nearest to the rocker switch, as shown in Figure 68. Since it is

not anticipated that this button will be regularly used, its placement in the small gap between the support structure strut and the powerbox prevents it from being accidentally depressed by the operators. Additionally, its close proximity to the low power board allows for a short wiring connection.

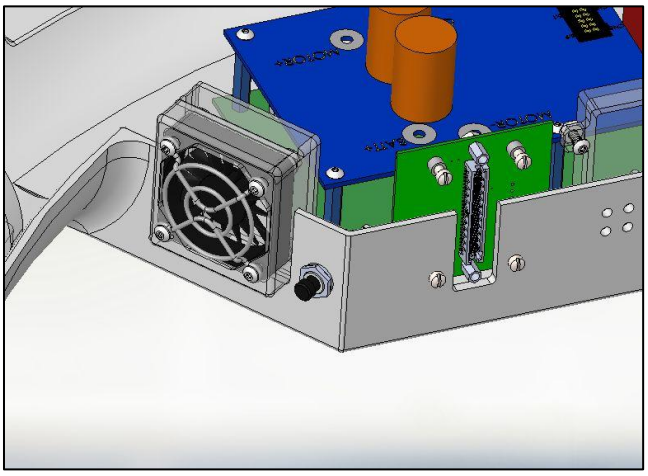

Figure 68 – Master Clear Pushbutton

Chapter 5: Simulations

5.1: WPT Modeling

5.1.1: Resonant Inductive Coupling Model

We begin by presenting a model used for investigating the performance of WPT. The block diagram shown in Figure 69 breaks down the various elements of the system into their respective transfer functions. Here we are assuming that the system is composed of two identical coils each having an inductance L and a resistance R. Some amount of capacitance C is added in series with each of the coils. Since C is much larger than the self-capacitance of the coils, it will dominate and hence we can model each coil circuit as a series RLC circuit. An additional component, the load resistor R_L, is placed in series with the secondary coil. The transfer functions for the primary and secondary coil circuits are shown as G_p and G_s.

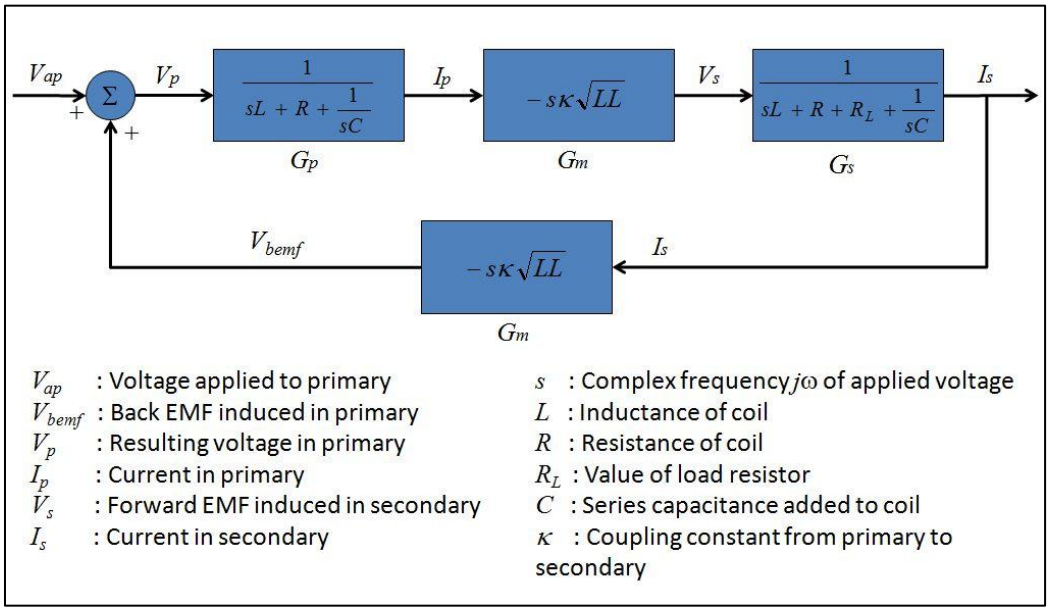

Figure 69 – Block Diagram for WPT

By Faraday's law of induction, the magnetic flux generated due to the current flowing in the primary will induce an EMF in the secondary. The magnitude of this induced EMF is proportional to the mutual inductance between the coils, which is a function of coil inductance L and the coupling coefficient κ. The coupling coefficient κ, which is always between 0 and 1 in value, is a geometric parameter which models how much of the magnetic flux generated by the primary coil actually penetrates the secondary coil. Additionally, the current flowing in the secondary will induce an EMF in the primary, known as the back EMF. The transfer function for mutual inductance is shown as G_m.

Now we assume that the system is driven by a sinusoidal voltage of frequency ω_0, where ω_0 is the resonant frequency of the primary and secondary coil circuits, given by

$$\omega_0 = \frac{1}{\sqrt{LC}} \tag{18}$$

where L is the coil inductance and C is the added capacitance. At resonance, our coil circuit transfer functions become

$$G_p = \frac{1}{R} \tag{19}$$

and

$$G_s = \frac{1}{R + R_L} \tag{20}$$

The peak current per volt applied to the primary is then given by

$$\left\|\frac{I_p}{V_{ap}}\right\| = \left\|\frac{G_p}{1 - G_p G_s G_m^2}\right\| = \frac{R + R_L}{L^2\kappa^2\omega_0^2 + R^2 + RR_L} \tag{21}$$

for the primary, and

$$\left\|\frac{I_s}{V_{ap}}\right\| = \left\|\frac{G_p G_s G_m}{1 - G_p G_s G_m^2}\right\| = \frac{L\kappa\omega_0}{L^2\kappa^2\omega_0^2 + R^2 + RR_L} \tag{22}$$

for the secondary. Similarly, the power consumed in each coil per volt squared applied to the primary is given by

$$\left\|\frac{P_p}{V_{ap}^2}\right\| = \frac{R(R + R_L)^2}{2(L^2\kappa^2\omega_0^2 + R^2 + RR_L)^2} \tag{23}$$

for the primary, and

$$\left\|\frac{P_s}{V_{ap}^2}\right\| = \frac{RL^2\kappa^2\omega_0^2}{2(L^2\kappa^2\omega_0^2 + R^2 + RR_L)^2} \tag{24}$$

for the secondary. The power consumed in the load resistor is given by

$$\left\|\frac{P_L}{V_{ap}^2}\right\| = \frac{R_L L^2\kappa^2\omega_0^2}{2(L^2\kappa^2\omega_0^2 + R^2 + RR_L)^2} \tag{25}$$

Power transfer efficiency is then given by

$$\eta = \frac{\left\|\frac{P_L}{V_{ap}^2}\right\|}{\left\|\frac{P_p}{V_{ap}^2}\right\| + \left\|\frac{P_s}{V_{ap}^2}\right\| + \left\|\frac{P_L}{V_{ap}^2}\right\|} = \frac{R_L L^2\kappa^2\omega_0^2}{(R + R_L)(L^2\kappa^2\omega_0^2 + R^2 + RR_L)} \tag{26}$$

Taking the partial derivative of η with respect to R_L gives

$$\frac{\partial\eta}{\partial R_L} = \frac{RL^2\kappa^2\omega_0^2(L^2\kappa^2\omega_0^2 + R^2 - R_L^2)}{(R + R_L)^2(L^2\kappa^2\omega_0^2 + R^2 + RR_L)^2} \tag{27}$$

which reveals an expression for the value of R_L which maximizes power transfer efficiency, given by

$$R_{L_{opt}} = \sqrt{L^2\kappa^2\omega_0^2 + R^2} \tag{28}$$

Substituting equation (28) back into equation (26) gives

$$\eta_{opt} = 1 + \frac{2R^2 - 2R\sqrt{L^2\kappa^2\omega_0^2 + R^2}}{L^2\kappa^2\omega_0^2} = 1 + \frac{2 - 2\sqrt{\frac{L^2\kappa^2\omega_0^2}{R^2} + 1}}{\frac{L^2\kappa^2\omega_0^2}{R^2}} \tag{29}$$

Defining Q as

$$Q = \frac{L\omega_0}{R} \tag{30}$$

equation (29) becomes

$$\eta_{opt} = 1 + \frac{2 - 2\sqrt{Q^2\kappa^2 + 1}}{Q^2\kappa^2} \tag{31}$$

Equation (31) shows that for any given coupling constant κ, which is a function of coil separation distance, the power transfer efficiency is maximized when Q is maximized, assuming that the load resistor is set to its optimum size as given by equation (28). Due to the proximity effect, L and R are functions of frequency – coil inductance will be reduced as frequency increases, and coil resistance will be magnified as frequency increases.

Using the curve fits for inductance and resistance versus frequency, the location of maximum Q for the coils was calculated to be approximately 460 Hz. To achieve this resonant frequency required the WPT capacitor to have a value of 10 μF.

5.1.2: Load Resistor Sizing

With the operating frequency for WPT now set at 460 Hz, we proceed with sizing a load resistor into which power will be transferred. First, however, we need an approximation for the coupling coefficient κ as a function of coil separation distance. Assuming that the coils are axially aligned with one another, [9] provides a means for predicting κ based on separation distance, which was used to calculate a set of 20 values for κ for separation distances ranging from 0.2 to 2 meters. Then, a curve fit was applied to these values having the form

$$\kappa = (d^{a_{fit}} + 1)^{b_{fit}} \tag{32}$$

where d is the axial separation distance between the coils and a_{fit} and b_{fit} are curve fit coefficients with values of $a_{fit} = 0.84$ and $b_{fit} = -6.25$. By using this form of curve fit equation, the value for κ agrees with the physical expectations that as $d \rightarrow 0$, $\kappa = 1$ and as $d \rightarrow \infty$, $\kappa = 0$. The calculated values and corresponding curve fit are shown in Figure 70.

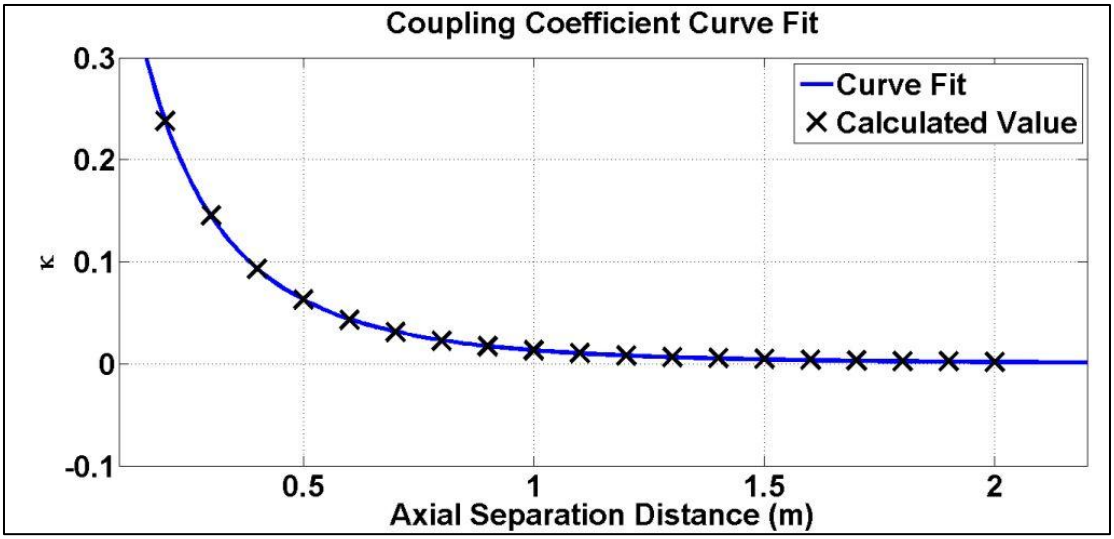

Figure 70 – Coupling Coefficient vs. Separation Distance

Now that we have an approximation for κ, we can model the predicted power transfer performance of the system at different separation distances. To do this, we again assume the primary coil is driven at resonance so that its transfer function is

$$G_p = \frac{1}{R} \tag{33}$$

where R is the coil's AC resistance at the WPT frequency of 460 Hz, which is predicted by the resistance curve fit to be 1.65 Ω. As before, the secondary coil circuit transfer function is

$$G_s = \frac{1}{R + R_L} \tag{34}$$

where R is 1.65 Ω and R_L is the value of the load resistor.

Figure 71 shows the predicted power transferred to the load for three different load resistor values. Due to the presence of the SPHERES vehicle inside each RINGS unit, there is a physical limit to how close together the two units can be positioned. This physical limit is approximately 30 cm and is represented by the vertical dashed line in Figure 71. For simplicity, each simulation assumes that the primary is driven with a sinusoidal voltage of 36 volts peak. In reality, the system is driven by a rectangular wave voltage which decreases in magnitude at higher current draws due to internal resistance in the batteries, so the predicted levels of transferred power shown here are slightly overestimated. However, the sinusoidal assumption still provides valuable insight into the qualitative behavior of the system for different values of load resistance R_L. We see that larger values of load resistance allow for higher maximum levels of power transfer, but the separation distance at which this maximum power transfer occurs decreases as the load resistance is increased. Since

the RINGS are physically limited to separation distances greater than 30 cm, the 2 Ω load resistor is most appealing as it allows for the investigation of system performance both above and below the optimum separation distance for maximum power transferred.

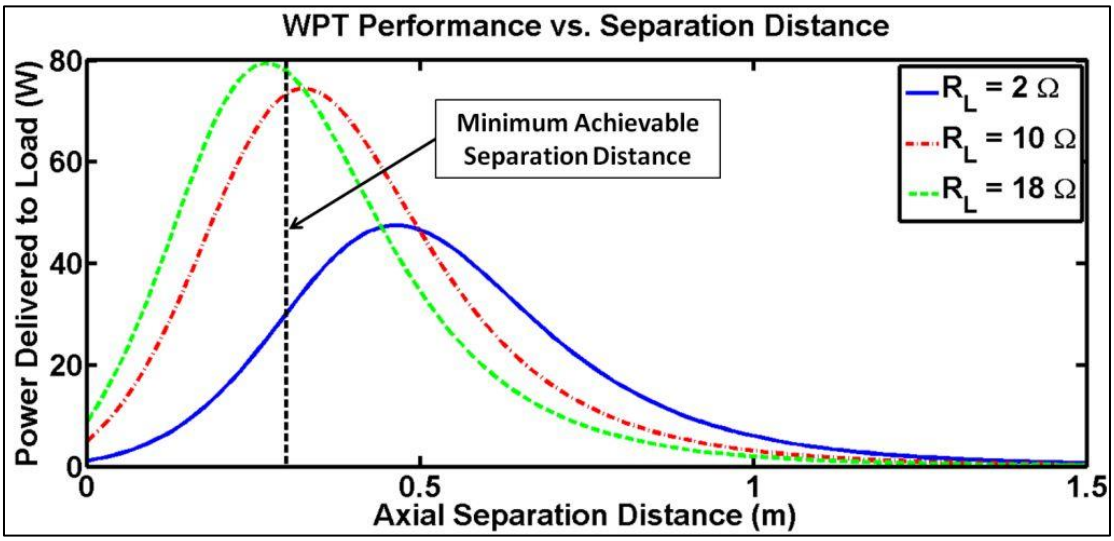

Figure 71 – Power Transfer Levels for Various Load Resistances

Figure 72 shows the predicted power transfer efficiency η for the same setup as in Figure 71. As with the total amount of power transferred, we see that the efficiency of power transfer is higher for larger values of load resistance, but only at small separation distances. In the region beyond 30 cm, the 2 Ω load resistor provides the best power transfer efficiency. Based on these results, a load resistor of 2 ohms was chosen.

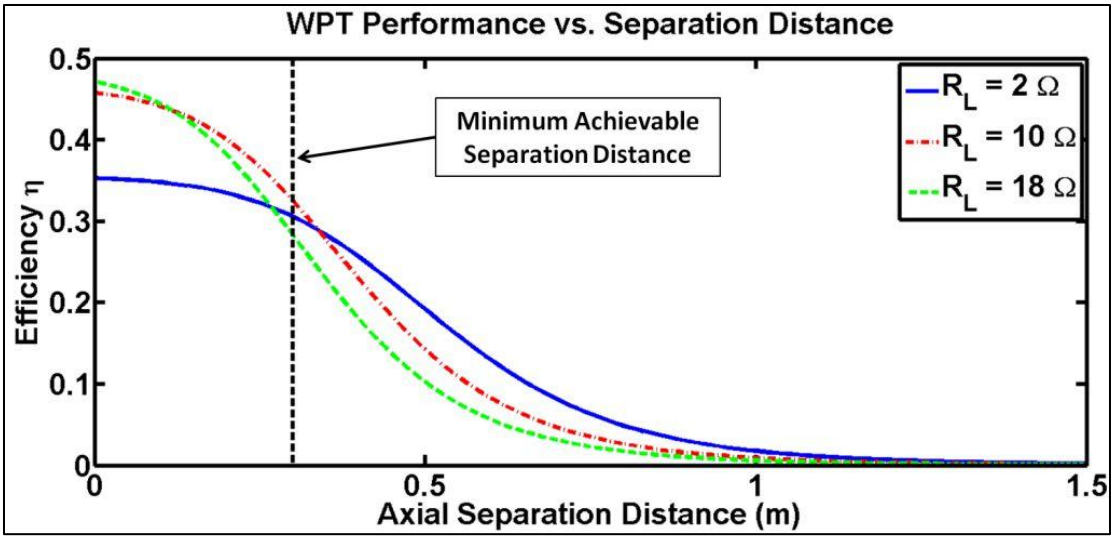

Figure 72 – Power Transfer Efficiency for Various Load Resistances

5.2: Driving Resonant Coil Circuit with Rectangular Wave

As a result of using the H-Bridge drive circuit architecture, the voltage applied to the coil circuit is an AC rectangular wave whose duty cycle and frequency are controlled with the onboard microcontroller. Due to the presence of higher frequency harmonics in the rectangular wave (the frequency of which is not equal to the resonant frequency of the system), coupled with the fact that the coil's resistance increases with frequency, the impedance of the coil circuit varies with the applied duty cycle. To investigate this phenomenon analytically, we first begin by modeling the rectangular wave as the sum of two Fourier series expansions for pulse trains. One of these pulse trains is positive and the other is negative and both have a period of oscillation T and pulse width τ. The phase difference between the two pulse trains is 180 degrees. The resulting sum can then be written as

$$V(t) = \sum_{n=1}^{\infty} D_n \cos\left(\frac{2\pi n}{T} t - \phi_n\right) \tag{35}$$

where

$$D_n = \sqrt{A_n^2 + B_n^2} \tag{36}$$

and

$$\phi_n = \tan^{-1}\frac{B_n}{A_n} \tag{37}$$

with

$$A_n = \frac{2}{n\pi}\sin\frac{\pi n\tau}{T}\left(\cos\frac{\pi n\tau}{T} - \cos\frac{\pi n(\tau - T)}{T}\right) \tag{38}$$

and

$$B_n = \frac{2}{n\pi}\sin\frac{\pi n\tau}{T}\left(\sin\frac{\pi n\tau}{T} - \sin\frac{\pi n(\tau - T)}{T}\right) \tag{39}$$

Note that with this notation convention, the duty cycle is given by

$$d = \frac{2\tau}{T}, \quad 0 \le d \le 1 \tag{40}$$

With the input having the form of (35), the steady-state response of the output is

$$I_{ss}(t) = \sum_{n=1}^{\infty} D_n|G_n|\cos\left(\frac{2\pi n}{T}t - \phi_n + \angle G_n\right) \tag{41}$$

where the transfer function G is given by

$$G_n = \frac{1}{j\omega_n L(\omega_n) + R(\omega_n) + {}^{1}/_{j\omega_n C}} \tag{42}$$

with

$$\omega_n = \frac{2\pi n}{T} \tag{43}$$

Note that in (42), L and R are functions of frequency as a result of the proximity effect. We seek to compute the impedance of the circuit, which is given by

$$Z = \frac{RMS\big(V(t)\big)}{RMS\big(I_{ss}(t)\big)} \tag{44}$$

Since the component waveforms of I_{ss} and V are orthogonal, we can rewrite equation (44) as

$$Z = \sqrt{\frac{RMS_{V_1}^2 + RMS_{V_2}^2 + \cdots + RMS_{V_n}^2}{RMS_{I_{ss_1}}^2 + RMS_{I_{ss_2}}^2 + \cdots + RMS_{I_{ss_n}}^2}} \tag{45}$$

or

$$Z = \sqrt{\frac{D_1^2 + D_2^2 + \cdots + D_n^2}{(D_1|G_1|)^2 + (D_2|G_2|)^2 + \cdots + (D_n|G_n|)^2}} \tag{46}$$

which can be solved computationally to produce the impedance of the circuit at a given duty cycle. The values of L and R at each harmonic are computed via the curve fits determined in Section 2.3.

Equation (46) was implemented numerically in a MATLAB script that calculates the results for the first 300 harmonics. With this large a number of harmonics, the solution is very well converged to its final value – the 300th harmonic only contributes an impedance on the order of e-20. The results for the EMFF operational mode are shown graphically in Figure 73. Also shown in Figure 73 are

experimental results for EMFF mode for duty cycles ranging from 15% to 85% in 5% increments. To obtain these experimental results, the RMS value of the applied voltage was measured using a multimeter. The RMS value of the current was simultaneously measured using an additional multimeter. This setup of measuring both the applied voltage and the resulting current allowed for calculation of the circuit impedance. Note that no secondary coil was present when the experimental data was obtained, as this could have potentially allowed induced EMFs to affect the results.

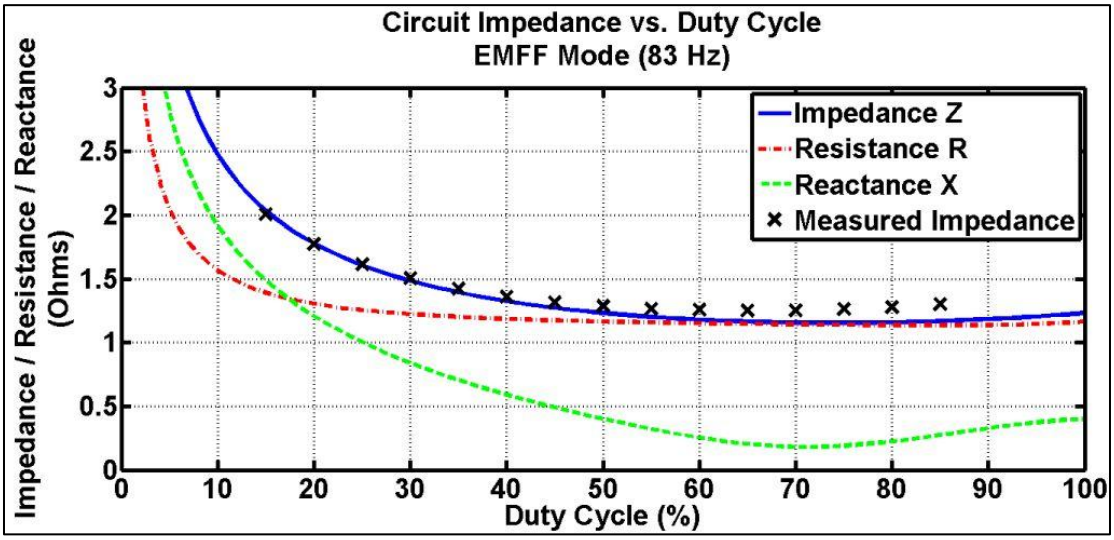

Figure 73 – Impedance vs. Duty Cycle for EMFF Mode

Additionally, we can determine the resistive component of the impedance by modifying our transfer function in equation (42). Removing the reactive components, the new transfer function is

$$G_n = \frac{1}{R(\omega_n)} \tag{47}$$

We can then calculate the reactive component of the impedance by

$$X = \sqrt{Z^2 - R^2} \tag{48}$$

where Z is obtained from the simulation that uses the transfer function in equation (42) and R is obtained from the simulation that uses the transfer function in equation (47). The reactance and resistance values obtained from this analysis are also plotted in Figure 73. These quantities are useful if one is interested in predicting the power dissipation in the coil at different duty cycles. The measured impedance values match up very well to the analytical predictions, both qualitatively and quantitatively. We also see that the location of minimum impedance in the experimental data, which occurs at approximately 70% duty cycle, is well predicted by the analytical results.

Figure 74 shows the same results as Figure 73, but for the WPT Transmit operational mode. The agreement between predicted impedance and measured impedance is not quite as good as it is in EMFF mode, which is probably due to errors in the curve fits for R and L. However, we again see a strong qualitative agreement between the analytical results and the experimental results. One interesting difference between the EMFF results and the WPT Transmit results is the difference in reactance between the two operational modes. In EMFF mode, the reactance contributes a significant amount to the impedance at duty cycles less than 50%. However, in WPT Transmit mode, the reactance is significantly smaller and hence the impedance, even at low duty cycles, is predominantly resistive.

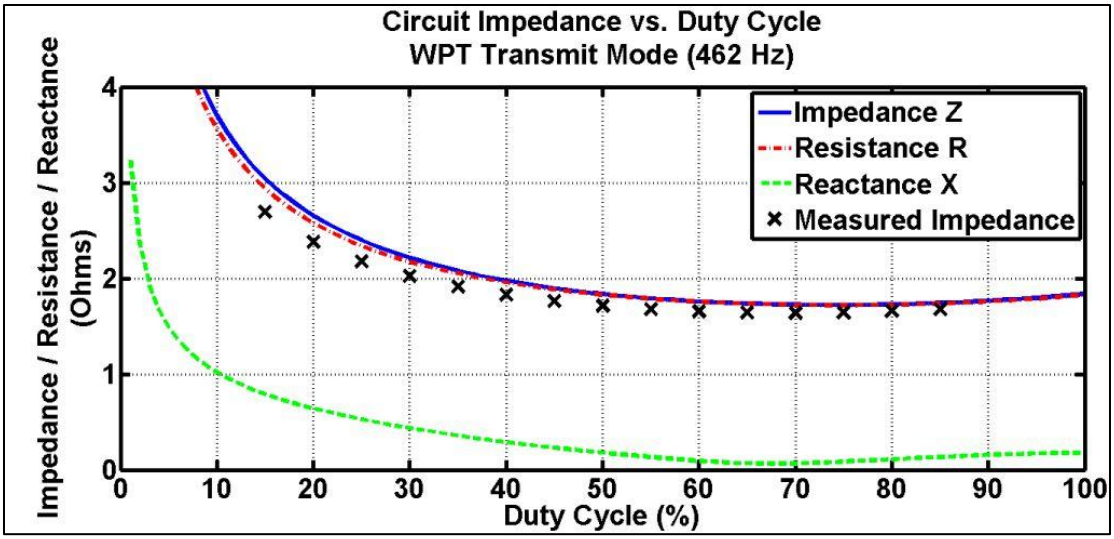

Figure 74 – Impedance vs. Duty Cycle for WPT Transmit Mode

5.3: EMFF Simulations

5.3.1: One-Coil Simulations

While the Fourier analysis presented in the Section 5.2 is useful for predicting the steady state response of the resonant coil circuit, it does not provide insight into the transient behavior of the circuit. Parameters such as the settling time and possible overshoot of the RMS coil current are of interest from a controls perspective. By numerically solving the differential equations, these transient response parameters can be investigated.

We begin with the simplest case of one coil being driven in EMFF mode without the presence of any secondary coil. In this case, the coil circuit transfer function is a simple second order system given by

$$\frac{I}{V} = \frac{1}{sL + R + {}^{1}/_{sC}} \tag{49}$$

Using MATLAB's "lsim" command, the coil current response to an AC rectangular wave applied voltage was investigated. For simplicity, we ignore the proximity effect on the higher harmonics by assigning fixed values for the inductance L and the resistance R. The capacitance and resonant frequency in EMFF mode are nominally 310 μF and 83 Hz, respectively. From these two numbers, we calculate an inductance L of 11.9 mH. Choosing a duty cycle of 50%, we then set the resistance R equal to the experimentally measured circuit impedance at this duty cycle, which is 1.29 Ω. The magnitude of the applied voltage is set to the nominal battery voltage of 36 volts. The results of the simulation are shown in Figure 75. Note that in Figure 75, the RMS current is calculated every half period. We see that the RMS current settles to 95% of its steady state value in approximately 60 msec, and exhibits no overshoot. These results are typical for all duty cycles. The settling time of 60 msec is a good result from a controls perspective, as the commanded current values from SPHERES are only updated at a frequency of 1 Hz. The lack of overshoot in the RMS current is also beneficial as it prevents an overcurrent event from occurring during the transient "ring-up" portion of the coil current response.

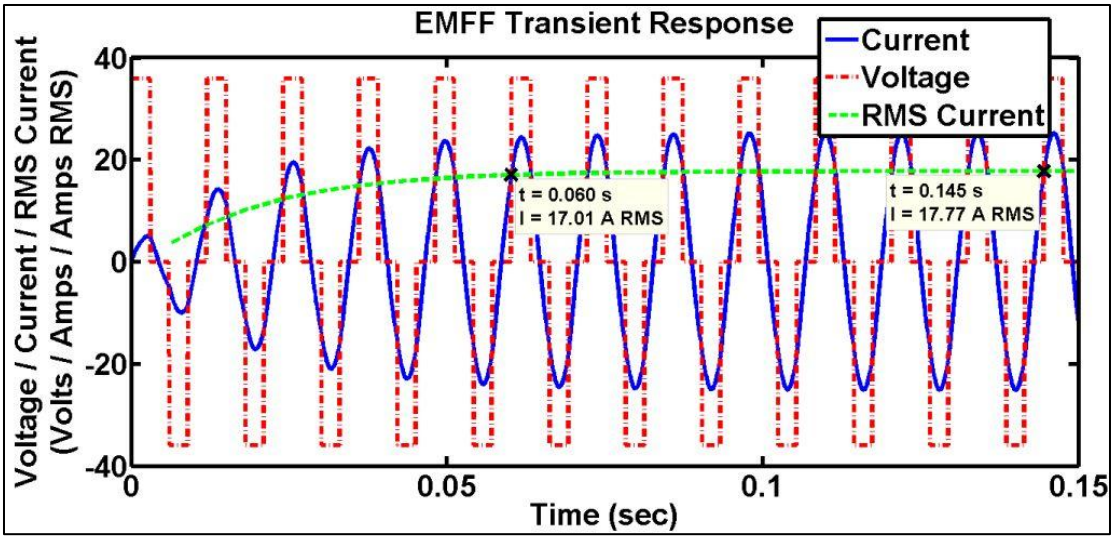

Figure 75 – One Coil EMFF Transient Simulation

We can also investigate the transient response to a sudden change in the phase of the applied voltage. This phase change is used in EMFF operations to dictate whether the two vehicles will attract or repel each other. The results of the phase change simulation are shown in Figure 76. Here, the simulation was first run for a length of time which was sufficient for the system to reach steady state conditions with an input phase angle of 0°. Then, at time t = 0, the input phase angle is set to 180°. All simulation parameters are the same as those used in Figure 75.

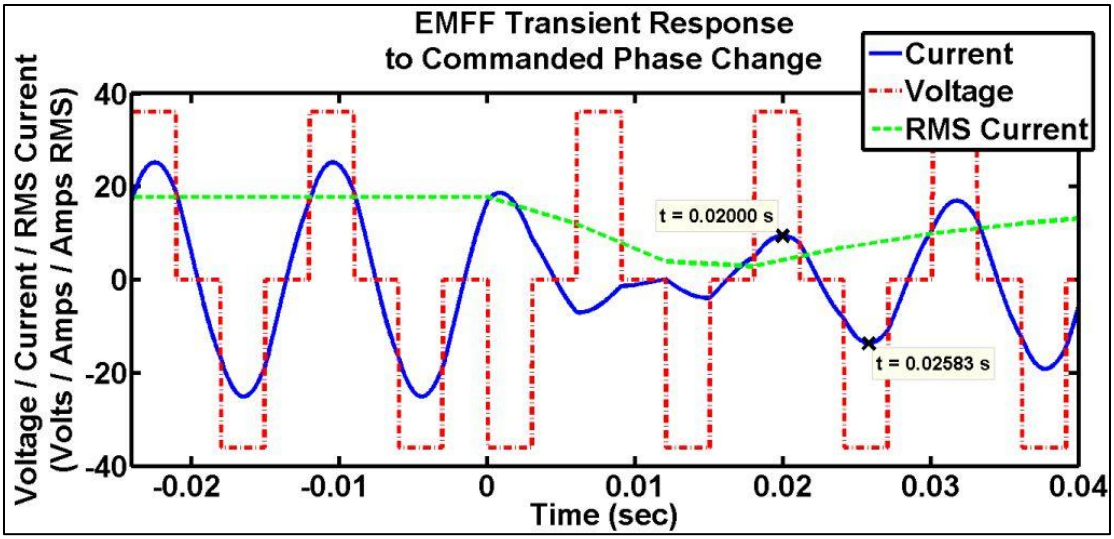

Figure 76 – One Coil EMFF Phase Change Response

In the steady state conditions seen when t < 0, it is clear that the peak current occurs in the middle of a driving pulse. With a 50% duty cycle, the middles of the driving pulses occur at times $t_1 = (mT+T/8)$ and $t_2 = (mT+5T/8)$, where T is the period of the applied voltage waveform and m is an integer. This allows us to determine a "phase settling time," or the amount of time required for the current to reach in-phase conditions after the new input is applied at t = 0. Starting at t = 0, we see that the output does not begin to take on a discernible sinusoidal shape until approximately halfway through the second period of the applied voltage. The middle of the second driving pulse of the second period occurs at exactly $t_1 = (T+5T/8) =$ 0.01958 seconds. As seen from the graph, however, the peak current occurs at $t_{Imax} =$ 0.02000 seconds. This results in a phase error of

$$\left|\frac{t_1 - t_{Imax}}{T}\right| = \left|\frac{0.01958 - 0.02000}{0.01205}\right| = 3.5\% \qquad (50)$$

after 20 msec. Applying the same technique to the next location of peak current, which occurs near the middle of the first driving pulse of the third period, results in a

calculated phase error of 1.9% after 26 msec. These results show a phase settling time, to within 98% of the steady state value, of approximately 26 msec. Though not visible in Figure 76, the settling time of the magnitude of the RMS current is similar (~60 msec) to that calculated in the "ring-up" simulation discussed previously.

Another area of interest regarding the rectangular wave input is the relationship between the applied duty cycle and the resulting coil current. Using the Fourier analysis presented in Section 5.2, along with the curve fits for inductance and resistance, an EMFF simulation was carried out to predict the RMS coil current for duty cycles ranging from 1% to 99% in 1% increments. The results of this investigation are shown in Figure 77. In addition to the nominal battery voltage of 36 volts, the simulation was also executed with battery voltages of 33 and 30 volts, to simulate system behavior as the batteries are depleted.

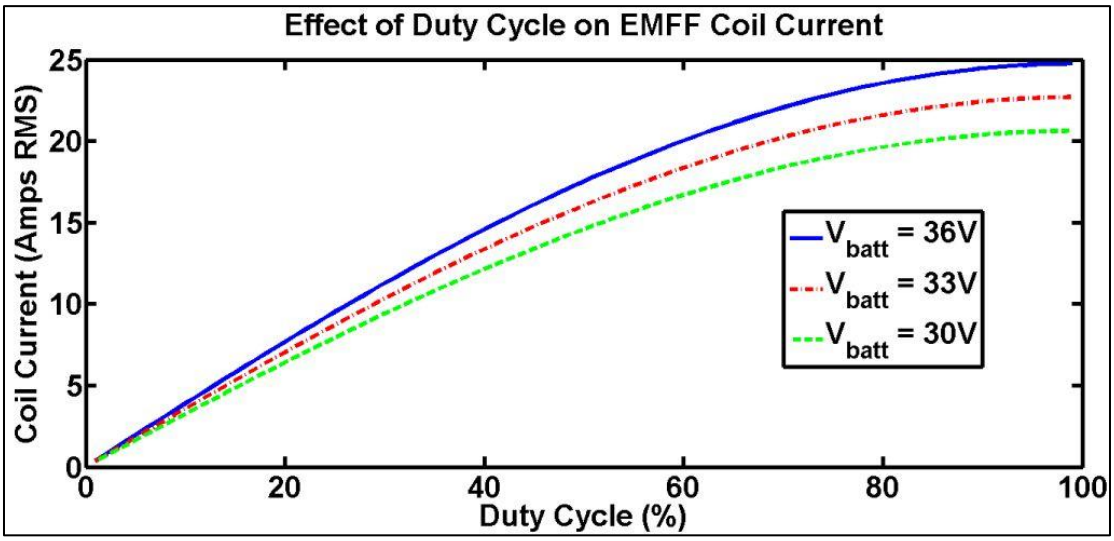

Figure 77 – Coil Currents vs. Duty Cycle in EMFF Mode

We see in Figure 77 that below about 50% duty cycle, a mostly linear relationship exists between the applied duty cycle and the resulting current in the coil. The difference in currents between the three different battery voltages is significant,

especially at higher duty cycles. This highlights the need for the implementation, on the PIC, of a duty cycle based current controller, since RINGS does not have the capability of reading in the battery voltage directly. More discussion on such a current controller is included in the conclusion chapter.

5.3.2: Two-Coil Simulations

With two coils present, the coil circuit behavior is slightly altered. This is due to the fact that the same inductive coupling phenomenon used for WPT is also present in two coil EMFF operations. However, the two coil EMFF setup differs from the WPT setup in that both coils are actively driven. A block diagram for the two coil EMFF setup is shown in Figure 78. Here, G_1 and G_2 represent the transfer functions for the two coil circuits, and are identical. The two G_m transfer functions represent the EMF induced in each coil due to the current flowing in the neighboring coil. The overall effect of these induced EMFs is a reduction in coil currents at close proximities.

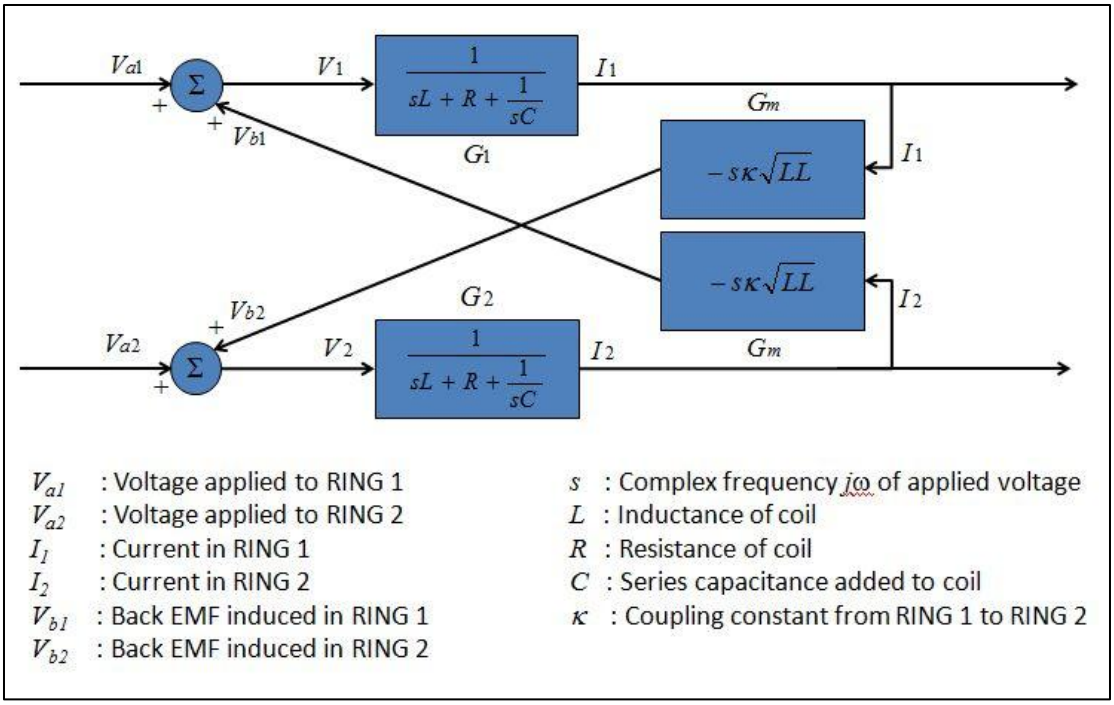

Figure 78 – Block Diagram for Two Coil EMFF

The setup shown in Figure 78 is a multiple-input and multiple-output (MIMO) system. The two system inputs are the voltages applied to each coil circuit and the two system outputs are the currents in each coil. To analyze the behavior of this system, a MIMO simulation was created in Simulink. The values for coil inductance, coil resistance, and the added capacitance are the same as was used in the 1 coil simulations from Section 5.3.1. Since we are interested in investigating how much the maximum achievable coil current is affected by the proximity of the two coils, we set the duty cycle to its maximum value of 99%. As before, the nominal battery voltage of 36 volts is used for the magnitude of the applied voltage. The coupling constant κ is computed as a function of axial separation distance using equation (32), as was done for the WPT simulations. In EMFF mode, the two coils will only ever be driven either in phase or out of phase with one another – no phase angle other than 0°

or 180° will ever be commanded. Consequently, only the two cases of driving in phase ($\angle V_{ad1} = \angle V_{ad2} = 0°$) or driving out of phase ($\angle V_{ad1} = 0°$, $\angle V_{ad2} = 180°$) are of interest to us. Running a number of individual simulations with in-phase conditions and out-of-phase conditions revealed that the current responses in the two coils are identical to each other for either of these two phase conditions.

A loop was created to investigate the system behavior for axial separation distances ranging from 1 cm to 1 m in increments of 1 cm. For each separation distance, the simulation was carried out with a sufficient time span so as to allow the system to reach steady state conditions, after which the RMS current value of the final period of oscillation was calculated. The results for the driven-in-phase and driven-out-of-phase cases are shown in Figure 79. Also shown in Figure 79 is the minimum possible separation distance of the two vehicles due to the presence of the SPHERES satellite in the assembly. We see that the two cases are nearly identical, with the exception of extremely small separation distances. At distances of 1 m and beyond, the inductive coupling has little effect and our maximum achievable current is predicted to be 21.5 amps RMS in each coil. At the minimum possible separation distance of 30 cm, the maximum achievable current is reduced to 18.3 amps, a 15% reduction from its far-field value. These results indicate that the RINGS vehicles can still achieve their maximum goal current of 18 amps RMS, even at their minimum possible separation distance. Since it is unlikely that the RINGS will ever be this close to each other during typical operations, the inductive coupling in EMFF mode will have little effect on system performance.

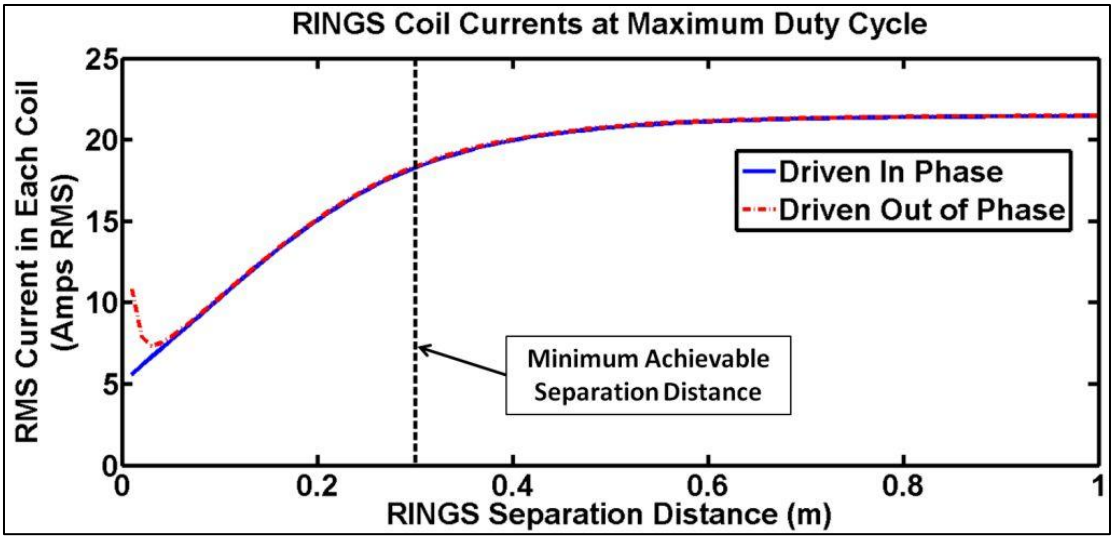

Figure 79 – Two Coil EMFF Simulation Results

Chapter 6: Conclusions

As discussed in Section 2.3, the proximity effect can cause the frequency of minimum impedance to be different from the frequency of zero reactance, introducing a source of error into the test setup. If the tests were repeated, more accurate results could be obtained by using the Lissajous curve feature on an oscilloscope to measure the phase angle between the applied voltage and the resulting current. Measuring the voltage waveform could be achieved by simply connecting a probe across the ends of the load. To accurately measure the current waveform, one could add a resistor in series with the load and place a probe across this resistor. The best choice for this resistor would be a film type composition (due to their low parasitic inductance) in the mΩ range so as to minimize power dissipation in the resistor. This setup, in conjunction with the multimeter setup used in the test, would produce more accurate values of resistance and inductance at different frequencies. Although the assumption that the frequency of minimum impedance is equal to the frequency of zero reactance may not apply to higher frequency ranges, they are most likely quite accurate at frequencies of less than 1 kHz where the proximity effect is not as pronounced. The lower accuracy of the curve fits at higher frequencies could be the source of error in the duty cycle versus impedance graphs in Section 5.2, especially in WPT mode. However, since the calculated frequency of maximum Q (460 Hz) was in the low frequency range, it is probably very close to the exact frequency of maximum Q.

While the compact coil design was advantageous from a packaging standpoint, the tight spacing between turns ultimately hindered the WPT capabilities of RINGS. Even by properly setting the resonant frequency of the system to the point

at which the quality factor Q was maximized, only a Q value of approximately 21 was achieved. By comparison, the one-turn helical design employed in [5] exhibited a measured Q value in excess of 900. The large discrepancy between the Q values of the RINGS multi-layer flat spiral design and their one-turn helical design highlights the massive impact that the proximity effect can have on system performance. Nonetheless, at present the RINGS system has successfully demonstrated the wireless transfer of 28 watts at 24% efficiency over a distance of half a meter, which agrees well with the models presented in Section 5.1.2. The capability for higher levels of power transfer is anticipated since the primary coil was not driven at its maximum permissible current level in this test.

Although the resonant coil design is less than ideal for achieving efficient WPT, it is extremely well suited for EMFF operations. By setting the EMFF operating frequency to the low value of 83 Hz, the proximity effect does not significantly increase power dissipation, since the coil resistance at this frequency is only slightly larger than it is at DC. As a result, the RINGS thermal control system exhibits good performance even at the high dissipated power levels present when operating at the maximum design current of 18 amps RMS.

The H-Bridge architecture proved to be an excellent choice for the drive circuit. Its power dissipation at full current is less than a watt, and it also carries the intrinsic benefit of allowing the PIC to set any desired frequency and duty cycle for the applied voltage. A current controller is presently in development at the MIT SSL and will be implemented on the PIC when complete. The inputs to the controller will come directly from the onboard Hall Effect current sensors. Once implemented, it

will actively adjust the duty cycle to achieve the commanded RMS current, which will be sent to the RINGS unit from the SPHERES satellite.

A total of four RINGS vehicles were built: two flight units which are currently (as of April, 2013) in Japan awaiting launch to the ISS, and two engineering prototype units. The engineering units are currently in use at the MIT SSL where they are undergoing flat floor testing with the goal of characterizing the dynamics of the system and implementing EMFF flight controllers. After their construction, the two flight units spent a week undergoing flat floor testing at the same facility, a picture of which is shown in Figure 80.

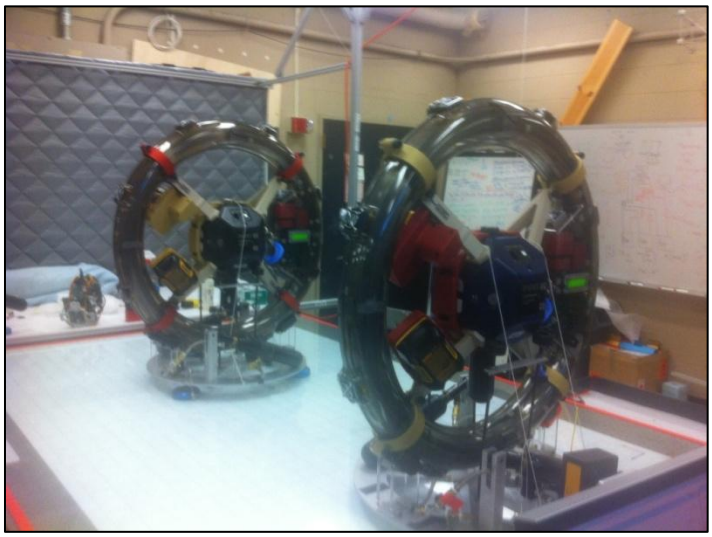

Figure 80 – RINGS Flight Units on the Flat Floor Facility at the MIT SSL

In support of future ISS operations, the two RINGS engineering units are currently scheduled for testing on a reduced gravity flight campaign in April 2013. These flights provide 20-30 seconds of microgravity conditions similar to that of the ISS environment in which the flight units will operate. In addition to the two engineering units, two SPHERES and a metrology system identical to the one on the ISS will also be used in the reduced gravity testing. This test setup will allow for a

more accurate characterization of the inertia matrix of the vehicles, as well as gathering of data on the EMFF dynamics at different current levels, separation distances, and orientations.

Bibliography

[1] O. Brown and P. Eremenko, "The Value Proposition for Fractionated Space Architectures," in *AIAA Space 2006 Conference*, San Jose, California, 2006.

[2] M. D. Neave, *Dynamic and Thermal Control of an Electromagnetic Formation Flight Testbed (Master's Thesis),* Cambridge, MA, 2005.

[3] D. W. Kwon, R. J. Sedwick and A. Sakaguchi, "Micro-Electromagnetic Formation Flight of Satellite Systems," in *AIAA Space 2010 Conference and Exhibition,* Anaheim, CA, 2010.

[4] N. Tesla, "Apparatus for Transmitting Electrical Energy". United States Patent 1,119,732, 18 January 1902.

[5] A. Kurs, A. Karalis, R. Moffatt, J. D. Joannopoulos, P. Fisher and M. Soljacic, "Wireless Power Transfer via Strongly Coupled Magnetic Resonances," *Science,* vol. 317, pp. 83-86, 2007.

[6] A. Karalis, J. D. Joannopoulos and M. Soljacic, "Efficient wireless non-radiative mid-range energy transfer," *Annals of Physics,* vol. 323, pp. 34-48, 2007.

[7] P. L. Dowell, "Effects of eddy currents in transformer windings," *Proceedings of the Institution of Electrical Engineers,* vol. 113, no. 8, 1966.

[8] V. C. Valchev and A. Van den Bossche, Inductors and Transformers for Power Electronics, CRC Press, 2005.

[9] F. W. Grover, Inductance Calculations, New York: D. Van Nostrand Company, 1946.